

PHASE CONJUGATE FIDELITY OF FOCUSED STIMULATED BRILLOUIN SCATTERING

L. P. Schelonka

August 1988

Final Report

Approved for public release; distribution unlimited.

AIR FORCE WEAPONS LABORATORY
Air Force Systems Command
Kirtland Air Force Base, NM 87117-6008

DTIC
ELECTE
OCT 18 1988
S **D**
QD

AD-A200 460



28 10 18 033

UNCLASSIFIED
SECURITY CLASSIFICATION OF THIS PAGE

REPORT DOCUMENTATION PAGE				
1a REPORT SECURITY CLASSIFICATION Unclassified		1b. RESTRICTIVE MARKINGS		
2a SECURITY CLASSIFICATION AUTHORITY		3 DISTRIBUTION / AVAILABILITY OF REPORT Approved for public release; distribution unlimited.		
2b. DECLASSIFICATION / DOWNGRADING SCHEDULE				
4 PERFORMING ORGANIZATION REPORT NUMBER(S) AFWL-TR-88-57		5 MONITORING ORGANIZATION REPORT NUMBER(S)		
6a. NAME OF PERFORMING ORGANIZATION Air Force Weapons Laboratory	6b OFFICE SYMBOL (if applicable) ARBM	7a NAME OF MONITORING ORGANIZATION		
6c ADDRESS (City, State, and ZIP Code) Kirtland Air Force Base, New Mexico 87117-6008		7b ADDRESS (City, State, and ZIP Code)		
8a. NAME OF FUNDING / SPONSORING ORGANIZATION	8b OFFICE SYMBOL (if applicable)	9 PROCUREMENT INSTRUMENT IDENTIFICATION NUMBER		
8c ADDRESS (City, State, and ZIP Code)		10 SOURCE OF FUNDING NUMBERS		
		PROGRAM ELEMENT NO. 62601F	PROJECT NO. 3326	TASK NO. 1B
		WORK UNIT ACCESSION NO. 01		
11 TITLE (Include Security Classification) PHASE CONJUGATE FIDELITY OF FOCUSED STIMULATED BRILLOUIN SCATTERING				
12. PERSONAL AUTHOR(S) Lee Paul Schelonka				
13a. TYPE OF REPORT Final	13b. TIME COVERED FROM Jan 85 to Jan 88	14. DATE OF REPORT (Year, Month, Day) 1988, August	15. PAGE COUNT 194	
16. SUPPLEMENTARY NOTATION Thesis				
17 COSATI CODES			18. SUBJECT TERMS (Continue on reverse if necessary and identify by block number)	
FIELD	GROUP	SUB-GROUP	Stimulated Brillouin scattering; Phase reconstruction	
20	02		Optical phase conjugation; Nonlinear optics.	
20	06		Phase conjugate fidelity; Aberrations	
19 ABSTRACT (Continue on reverse if necessary and identify by block number)				
<p>The first measurements of the effect of the focal intensity on the fidelity of phase conjugation in focused stimulated Brillouin scattering (SBS) are reported. Regardless of the strength of aberration, laser beams with focal intensities above 5 times the SBS threshold were conjugated accurately. As the focal intensity declined below this value, the phase conjugate fidelity declined. The maximum correctable aberration strength was that which reduced the focal intensity to near the SBS threshold. Higher laser powers corrected stronger aberrations.</p> <p>The pump laser was a single axial mode, tripled, Q-switched Neodymium:YAG, with a 6 nm pulse width, operating at 355 nm. The pulsewidth was 30 times the phonon lifetime (180 ps) of the SBS medium, liquid hexane. The 1.5 cm diameter beam was focused directly into a 2 cm diameter, 20 cm long cell using a 20 cm focal length lens placed 10 cm from the cell. Focal intensities ranging from below the SBS threshold ($22.5 \pm 4.5 \text{ GW/cm}^2$) to 55 times the SBS (over)</p>				
20. DISTRIBUTION / AVAILABILITY OF ABSTRACT <input checked="" type="checkbox"/> UNCLASSIFIED/UNLIMITED <input type="checkbox"/> SAME AS RPT <input type="checkbox"/> OTIC USERS			21 ABSTRACT SECURITY CLASSIFICATION Unclassified	
22a. NAME OF RESPONSIBLE INDIVIDUAL Lee P. Schelonka, Captain, USAF			22b. TELEPHONE (Include Area Code) (505) 844-0475	22c. OFFICE SYMBOL AFWL/ARBM

DD FORM 1473, 84 MAR

83 APR edition may be used until exhausted.
All other editions are obsolete.

SECURITY CLASSIFICATION OF THIS PAGE
UNCLASSIFIED

UNCLASSIFIED

SECURITY CLASSIFICATION OF THIS PAGE

19. ABSTRACT (continued)

threshold ($1250+250 \text{ GW/cm}^2$) were studied. A maximum reflectivity of 75% occurred at the maximum focal intensity.

A computerized far-field image analysis system directly measured the focal intensity reduction due to aberrations. The focal intensity of the brightest far-field spot controlled both the reflectivity and the fidelity. A pair of laminar airflow, hot-wire array aberrators provided continuously variable, nearly sinusoidal phase modulation in the transverse axes. Lateral shearing interferometry and energy in the bucket measurements gave the Strehl ratio of the backscattered (reconstructed) beam, and hence the phase conjugate fidelity.

A phenomenological theory for the phase conjugate fidelity of focused SBS was developed using resonator boundary conditions and a Gauss-Hermite mode decomposition. Analytical solutions for the case of no pump depletion were in qualitative agreement with the data.

Traces; — 4. 10. 18

The first measurements of SBS gain depletion during mode beating within a Q-switched laser pulse are also reported. The gain depletion occurred only during the brightest and fastest mode beating spike. The remainder of the scattered pulse replicated the pump pulse. Gain depletion occurred when the mode beating spikes were approximately 2.5 times the phonon lifetime in duration. This agrees well with the theory of gain switching from stimulated Brillouin scattering to stimulated Raman scattering.



Accession For	
NTIS ORARI	<input checked="" type="checkbox"/>
DTIC TAB	<input type="checkbox"/>
Unannounced	<input type="checkbox"/>
Justification	
By	
Date	
Project, Codes	
Distribution	
Remarks	
A-1	

ACKNOWLEDGEMENTS

Many people helped make this research exciting and enjoyable. Richard J. Cook taught me quantum mechanics in a way that showed the beauty and simplicity of the field. Marlan O. Scully's enthusiasm for the field of quantum optics helped me choose a nonlinear optics research topic. My dissertation committee members, Ronald R. Bousek, Kenneth C. Jungling, Sudhakar Prasad, and Christopher M. Clayton constantly encouraged me and provided technical insight and suggestions at every juncture. My advisor, John K. McIver, has been teacher, mentor, and friend for the past three years. His support and technical direction were crucial throughout this research. My colleagues and superiors at the Air Force Weapons Laboratory took an active interest in the research and provided equipment, a laboratory, and technical support. In particular, I appreciate the help of Carol K. Davis for digitizing and plotting the interferometric data, and Clifford A. Thies for designing and building the video image data acquisition system. Bernice Davidson did a thorough, professional job of typing the first draft from nearly illegible notes. Thomas F. Lowum, Jeanne S. Swecker, Scott C. Holswade, and Paul A. Laferriere conscientiously and carefully edited the manuscript, reducing it by almost 100 pages. In the words of Mark Twain, "If I'd had more time, I would have written a shorter book!" My wife, Debbie, has been a constant source of strength and encouragement throughout the research and writing. Finally, I would like to give thanks to Jesus Christ. His love, mercies, and blessings have indeed made this research possible.

PHASE CONJUGATE FIDELITY
OF FOCUSED STIMULATED BRILLOUIN SCATTERING

Lee Paul Schelonka

B.A. Physics, University of Colorado, 1978

M.A. Political Science, New Mexico State University, 1982

M.S. Engineering Physics, Air Force Institute of Technology, 1983

M.S. Chemical Physics, Air Force Institute of Technology, 1984

Ph.D. Optical Sciences, University of New Mexico, 1988

The first measurements of the effect of the focal intensity on the fidelity of phase conjugation in focused stimulated Brillouin scattering (SBS) are reported. Regardless of the strength of aberration, laser beams with focal intensities above 5 times the SBS threshold were conjugated accurately. As the focal intensity declined below this value, the phase conjugate fidelity declined. The maximum correctable aberration strength was that which reduced the focal intensity to near the SBS threshold. Higher laser powers corrected stronger aberrations.

The pump laser was a single axial mode, tripled, Q-switched Neodymium:YAG, with a 6 ns pulsewidth, operating at 355 nm. The pulsewidth was 30 times the phonon lifetime (180 ps) of the SBS medium, liquid hexane. The 1.5 cm diameter beam was focused directly into a 2 cm diameter, 20 cm long cell using a 20 cm focal length lens placed 10 cm from the cell. Focal intensities ranging from below the

SBS threshold ($22.5 \pm 4.5 \text{ GW/cm}^2$) to 55 times the SBS threshold ($1250 \pm 250 \text{ GW/cm}^2$) were studied. A maximum reflectivity of 75% occurred at the maximum focal intensity.

A computerized far field image analysis system directly measured the focal intensity reduction due to aberrations. The focal intensity of the brightest far field spot controlled both the reflectivity and the fidelity. A pair of laminar airflow, hot wire array aberrators provided continuously variable, nearly sinusoidal phase modulation in the transverse axes. Lateral shearing interferometry and energy in the bucket measurements gave the Strehl ratio of the backscattered (reconstructed) beam, and hence the phase conjugate fidelity.

A phenomenological theory for the phase conjugate fidelity of focused SBS was developed using resonator boundary conditions and a Gauss-Hermite mode decomposition. Analytical solutions for the case of no pump depletion were in qualitative agreement with the data.

The first measurements of SBS gain depletion during mode beating within a Q-switched laser pulse are also reported. The gain depletion occurred only during the brightest and fastest mode beating spike. The remainder of the scattered pulse replicated the pump pulse. Gain depletion occurred when the mode beating spikes were approximately 2.5 times the phonon lifetime in duration. This agrees well with the theory of gain switching from stimulated Brillouin scattering to stimulated Raman scattering.

TABLE OF CONTENTS

	<u>Page</u>
Acknowledgements.....	iii
Abstract.....	v
Table of Contents.....	vii
List of Figures.....	x
List of Tables.....	xvii
 Chapter 1. Introduction.....	 1
1.A. Motivation and General Discussion.....	1
1.B. Background.....	7
1.C. Organization, Units, and Terminology.....	11
 Chapter 2. Apparatus and Measurement Techniques.....	 12
2.A. Overview.....	12
2.B. Laser/SBS System.....	14
2.C. Temporal Pulse Shape and Spectrum Diagnostics.....	17
2.C.1. General.....	17
2.C.2. Single Axial Mode Check.....	20
2.C.3. Mode Beating Measurements.....	22
2.D. Input and Backscattered Pulse Intensity (Reflectivity Measurements).....	 23
2.E. Near Field Phase.....	26
2.F. Far Field Intensity Profiles.....	31
2.G. "Energy in the Bucket" Fidelity Diagnostic System..	38

TABLE OF CONTENTS, cont'd

	<u>Page</u>
2.H. Variable Phase Grating Aberrator.....	48
2.H.1. General.....	48
2.H.2. Optical Layout and Aberration Measurement Technique.....	49
2.H.3. Aberration Data.....	52
Chapter 3. Data and Analysis.....	61
3.A. Summary of Published Experimental Data.....	62
3.B. Temporal and Frequency Effects.....	65
3.B.1. Overview.....	65
3.B.2. Pulse Compression.....	66
3.B.3. Mode Beating Effects.....	74
3.C. SBS Reflectivity.....	83
3.D. Characteristics of the Focused Speckle Field: Speckle-Free Stimulated Brillouin Scattering.....	89
3.E. Phase Conjugate Fidelity.....	96
3.E.0. Overview.....	96
3.E.1. Aberration Strength Effects: Phase Reconstruction.	97
3.E.2. Aberration Strength Effects: Energy in the Bucket.	100
3.E.3. Focal Intensity Effects.....	102
3.E.4. "Second Order Effects".....	108
3.E.5. Summary of Phase Conjugate Fidelity Findings.....	112

TABLE OF CONTENTS, cont'd

	<u>Page</u>
Chapter 4. Theory.....	114
4.A. Derivation of the Coupled Gain Equations.....	115
4.B. Plane Wave Equations.....	120
4.C. Temporal Equations.....	128
4.D. SBS in Three Dimensions: Phase Conjugation.....	133
4.D.1. Boundary Conditions.....	139
4.D.2. Solutions to the Equations for SBS in a Resonator..	140
Two Transverse Axes of Aberration.....	152
Focal Intensity Effects.....	153
Comparison to Experimental Data.....	154
Chapter 5. Conclusions.....	158
References.....	162

LIST OF FIGURES

Figure	<u>Page</u>
1.1 Photographs of laser far field spots. (a)--aberrated spot, (b)--phase conjugated, reconstructed spot.....	2
1.2 Phase conjugate reflection. The laser reflects from the sound wave.	4
1.3 Aberration and reconstruction by phase conjugation. The backscattered beam is automatically reconstructed.	6
2.1 Schematic of the time-resolved intensity diagnostics and optical layout.....	24
2.2 Schematic of the shearing interferometry optical layout..	27
2.3 Lateral shearing interferometry. Front and back surface reflections interfere, giving fringes in the overlap region.	28
2.4 Schematic of the far field intensity analysis system and optical layout.....	32
2.5 Unaberrated far field intensity distribution.....	34

LIST OF FIGURES, cont'd

Figure	Page
2.6 Aberrated far field intensity distribution.....	35
2.7 Energy in the bucket optical layout.....	39
2.8 The encircled energy is plotted as a function of radius, for several spot sizes.	41
2.9 Normalized far field intensity profiles for several spot sizes.	42
2.10 The Strehl ratio is plotted versus the energy in the bucket for a one Airy bucket pinhole.	44
2.11 The Strehl ratio is plotted versus the energy in the bucket for a half Airy bucket pinhole.	45
2.12 Variable aberrator.....	50
2.13 Schematic of the aberrator analysis optical layout.....	51
2.14 Plots of the measured optical path difference across the wavefront.....	53

LIST OF FIGURES, cont'd

Figure	Page
2.15 Sinusoidal fits to the data in Fig. 2.14.....	54
2.16 The aberration strength is plotted as a function of the aberrator voltage.	58
2.17 The measured and predicted intensity reduction, and the reciprocal of the divergence are plotted versus the measured divergence.	59
3.1 Pump and Stokes intensities versus time (oscillographs)..	67
3.2 The pump and Stokes pulsewidths (FWHM) are plotted versus the pump intensity divided by the threshold intensity. .	69
3.3 The normalized pump and predicted Stokes pulses are plotted versus time.	71
3.4 The predicted and actual values of the pulse compression are plotted versus the peak pump intensity over the SBS threshold intensity.	73

LIST OF FIGURES, cont'd

Figure	Page
3.5 The pump and Stokes pulse relative intensities are plotted versus time and frequency. The laser operates on a single axial mode.	75
3.6 Temporal and spectral structure of the pump and Stokes pulses for two modes beating. The modes are separated by 3 times the cavity mode spacing.	77
3.7 Temporal and spectral structure of the pump and Stokes pulses. Modes separated by twice the cavity mode spacing.	78
3.8 Temporal and spectral structure of the pump and Stokes pulses for two adjacent modes beating.	79
3.9 Multimode temporal and frequency structure. The Stokes pulse replicates the pump pulse.	80
3.10 Gain depletion in the Stokes pulse during fast, intense mode beating.	82

LIST OF FIGURES, cont'd

Figure	Page
3.11 The SBS reflectivity is plotted as a function of the focal intensity divided by the threshold intensity. The intensity was changed by changing the laser power in (a), and by aberrating the beam in (b).	84
3.12 The reflectivity is plotted as a function of the aberration strength, for beams with focal intensities approximately equal to 16 times the SBS threshold.	88
3.13 The measured speckle length is plotted as a function of the divergence.	90
3.14 Photographs of the Gauss-Hermite modes of a laser resonator (after Ref. 91)	93
3.15 Photographs of the far field intensity patterns produced by the variable aberrator	94
3.16 The reconstructed Stokes beam's interferometrically measured Strehl ratio is plotted as a function of the aberrated pump's Strehl ratio.	98

LIST OF FIGURES, cont'd

Figure	Page
3.17 The phase conjugate fidelity is plotted versus the aberration strength.	101
3.18 The phase conjugate fidelity is plotted versus the aberrated focal intensity.	103
3.19 All fidelity versus focal intensity data from Fig. 3.18 (a)-(f) is plotted on a single curve.	105
3.20 All fidelity versus focal intensity data for unaberrated pump pulses is plotted on the same curve as in Fig. 3.19.	106
3.21 The slight decrease in fidelity for increasing focal intensity is plotted for unaberrated and slightly ($\xi \approx 1.3$) aberrated beams.	109
3.22 The fidelity is plotted as a function of the aberration strength, for constant ($I = 10I_{th}$) focal intensity.	111
4.1 Geometry of the plane wave problem.....	121

LIST OF FIGURES, cont'd

Figure	Page
4.2 The intensities of the pump and Stokes beams are plotted versus the distance z , for several values of the reflectivity R	126
4.3 The SBS gain reduction for short pulses is plotted versus the pulsewidth.	130
4.4 The modified SBS gain reduction, taking into account linewidth effects, is plotted versus the pulsewidth. ...	132
4.5 The long gain region for SBS in a lightguide is compared to the shorter gain region for SBS in the focused geometry.	135
4.6 The predicted (Ref. 13) and measured phase conjugate fidelity is plotted versus the focal intensity over the SBS threshold intensity.	138
4.7 The predicted (new model) and measured phase conjugate fidelity is plotted as a function of the intensity over the SBS threshold.	155

LIST OF TABLES

<u>Table</u>		<u>Page</u>
2.1	Aberrator OPD and Strehl ratio data: double pass.....	55
2.2	OPD, Strehl ratio, and predicted and measured focal intensity reductions: single pass.....	57
3.1	Pump and Stokes pulsewidths.....	68
4.1	Values of the overlap integral $Q_{\alpha n m \beta}$ for $\alpha = \beta$, $n = m$	143
4.2	Values of the overlap integral $Q_{\alpha n m \beta}$ for $\alpha \neq \beta$, $n = m = 0, 1$	144
4.3	Nonconjugate fraction as a function of the aberration strength for $g_{11} = 25$ (single aberration axis).....	151

Chapter 1. Introduction

1.A. Motivation and General Discussion

An undistorted laser beam can travel long distances without much decrease in intensity and can be focused to a single bright spot. However, when a laser beam travels through an aberrating medium, its phase is distorted. As the beam continues to propagate, these phase distortions cause intensity distortions, turning a uniform, highly focusable laser beam into a distorted, largely unfocusable beam. Fig. 1.1(a) is a photograph of a laser beam which has been distorted by passing through hot and cold flowing air, then focused onto a solid state video camera. It is clear that this beam has a nonuniform intensity structure, and the focus consists of many spots. Since the energy of the original beam is shared among the spots, each spot has very little intensity. If the laser beam could be "reconstructed" into a single focal spot, the spot would be much more intense.

One method of reconstructing distorted laser beams is optical phase conjugation. A "phase conjugate mirror" reverses the wavefront and forces the beam to travel back through the aberrator, producing a beam with no distortions. Such a beam is shown in Fig. 1.1(b). The beam is clearly more intense and sharply focused.



(a)

(b)

Figure 1.1 Photographs of laser far field spots. (a) - Aberrated spot. (b) - Phase conjugated, reconstructed spot.

Stimulated Brillouin scattering, the scattering of light waves from sound waves, is one of the nonlinear optical processes which can produce phase conjugation. Intense laser beams cause pressure changes (via electrostriction) in certain liquids, producing sound waves. These sound waves change the refractive index of the liquid, forming efficient scattering gratings which have the same curvature as the laser wavefront. The curvature of the gratings produces phase conjugation, or wavefront reversal of the input beam. Fig. 1.2 depicts a distorted laser beam and the sound wave it produces. The sound wave produces a replica of the laser beam traveling in the reverse direction.

The backward traveling wave has the same phase as the input laser beam, but is reversed in direction. In 1972, Zel'dovich, et. al. recognized that this would be characteristic of a wave which can be described mathematically as the the complex conjugate of the input wave.¹ It has been shown that this process of "phase conjugation" is equivalent to a reversal in time.² The concept of time reversal is useful for understanding phase conjugation. A laser beam is aberrated as it propagates through a distorter. If this laser beam is time-reversed upon phase conjugation, it will automatically undo its aberrations as it retraverses the distorter. If the reversal is accurate (high fidelity), the wavefront is reconstructed to its original (unaberrated) quality.

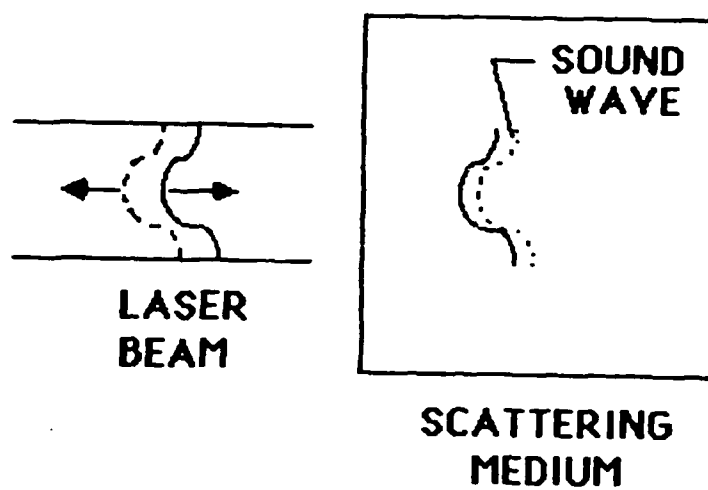


Figure 1.2 Phase conjugate reflection.

In Fig. 1.3 an input beam (denoted by a solid line) is aberrated as it passes through a distorter. It is "phase conjugated" or reversed in time by the scattering medium. Thus, it reflects back in the direction from which it came (dashed line) and is reconstructed as it retraverses the aberrator.

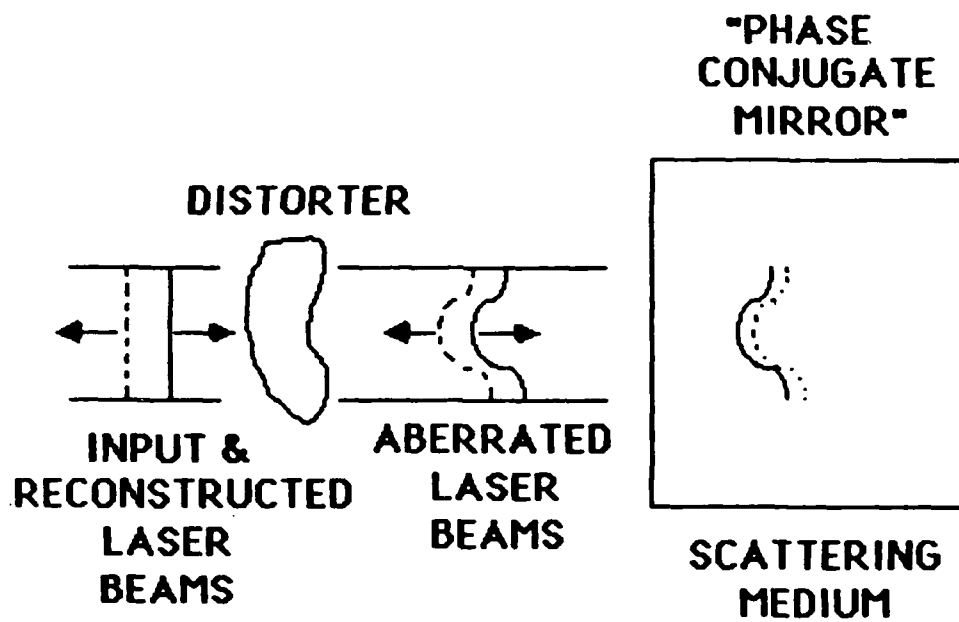


Figure 1.3 Aberration and reconstruction by phase conjugation. The backscattered beam is automatically reconstructed.

1.B. Background

Spontaneous scattering of light waves by thermally excited sound waves was experimentally investigated by Lord Rayleigh in the 1800's.³ In the early 1900's, Brillouin predicted that light could produce sound waves by electrostriction and then scatter the sound waves.^{4,5} However, stimulated Brillouin scattering (SBS) was not discovered until after the invention of the laser. In the 1960's SBS was observed in solids, liquids, and gases.⁶⁻¹⁰ Even the earliest studies of SBS mention that the scattered beam has maximum gain in the backward direction⁶ and the scattered light retraverses its input path.^{9,10}

In 1972, Zel'dovich and coworkers found that laser light which had passed through an etched glass distortion plates was reconstructed by backward SBS.¹ The backscattered beam automatically reconstructed itself after retraversing the distortion plate. This unexpected result led to the concepts of phase conjugation^{1,11} and time reversal.² The fidelity, or accuracy of phase conjugation is generally defined as the degree of overlap of the backscattered beam with the input beam. The overlap can be expressed as an integral.¹²⁻¹⁷ Letting F be the phase conjugate fidelity, we have

$$F(z) = \frac{|\int dx dy E_L(x,y,z) E_S(x,y,z)|^2}{\int dx dy |E_L(x,y,z)|^2 \int dx dy |E_S(x,y,z)|^2} \quad (1.5)$$

where E_L is the input (laser) field, E_S is the backscattered ("Stokes") field, and z is the propagation direction.

$F(z)$ varies only within the Brillouin medium.¹⁶ Outside the medium, where F is measured, it is constant in z . If we take $z=z_0$ anywhere outside the medium,

$$F = \text{const} = \frac{|\int dx dy E_L(x, y, z_0) E_S(x, y, z_0)|^2}{\int dx dy |E_L(x, y, z_0)|^2 \int dx dy |E_S(x, y, z_0)|^2} \quad (1.6)$$

The numerator is the absolute square of the integrated overlap of the pump and Stokes fields, taking into account both amplitude and phase. The denominator is a normalization factor, which equals the product of the integrated pump and Stokes intensities. When $F=1$, the overlap is complete and the fidelity, or wavefront reconstruction accuracy, is perfect. When $F=0$, the overlap is nonexistent, and the wavefront is not reconstructed.

Soon after the discovery and first analysis of phase conjugation, theoretical and experimental studies began with a goal of understanding the fidelity of phase conjugation. In the first experimental observation of phase conjugation, a long (~ 1 meter), small cross section (~ 4 mm²), reflective tube, filled with liquid, was used. Because of this, the early theory and experiments concentrated on this "waveguide" or "lightguide" geometry. A crucial result of these studies is that for accurate phase conjugation, it is necessary to distort the beam before focusing it into the waveguide.¹

Theoretical studies have shown that if the beam is distorted to more than 10 or 15 times the diffraction limited divergence, accurate phase conjugation takes place.^{14,16,18-25} Experimental studies have confirmed this for the SBS waveguide geometry.^{17,21,26-35}

In 1977, it was shown experimentally that accurate phase conjugation occurred in focused SBS, without a lightguide.^{36,37} In Ref. 37, the data indicate that the phase conjugate fidelity declined when the input beam divergence far exceeded the diffraction limit. The authors' conclusion however, was that accurate phase conjugation occurs only when the divergence far exceeds the diffraction limit and the fidelity declines as the divergence approaches this limit. This is contrary to what their data show. The error is made in a statement analyzing the data, and in the final equation.

This early paper was pivotal in the development of SBS fidelity theory, and the influence of its incorrect conclusions is still widespread. We note that in the common theoretical formalism, it is assumed that the beam must be strongly aberrated for accurate phase conjugation in focused SBS to occur.^{13,17,21,37-40} Many of these papers cite Ref. 37 as evidence for the strong aberration assumption.

In the next several years, experimental studies of the accuracy of phase conjugation in focused SBS were done. None of these studies showed that a strong amount of aberration was required for accurate phase conjugation. It has been firmly established that diffraction limited beams are conjugated accurately by focused SBS.^{21,26,38,41-44}

The few studies of focused SBS with weakly aberrated beams have shown accurate phase conjugation.^{26,42} However, even the most recent theoretical works on focused SBS continue to suggest that there will be a minimum amount of distortion (several times diffraction limited) required for accurate phase conjugation in focused SBS.^{21,38} The observed maximum amounts of aberration (above which the fidelity declined sharply) varied widely from experiment to experiment.^{26,37,38,42-44} The wide spread in the reported experimental data, and the different conclusions of the published theory and experiments have led to a lively debate about the utility of focused SBS for optical systems requiring accurate phase conjugation of weakly and strongly aberrated beams. Resolving the question of the minimum and maximum amounts of aberration corrected by focused SBS forms the crux of this study.

1.C. Organization, Units, and Terminology

This dissertation is organized as follows. The introduction is followed by a description of the experimental apparatus and techniques. A discussion and analysis of the results follows. Next, a phenomenological theory of focused SBS is developed, which qualitatively agrees with the data. Finally, conclusions and recommendations for further study are presented.

The metric system of units is used throughout the apparatus and data chapters of this dissertation. Gaussian units are used in the theoretical chapter, because the majority of references are written in Gaussian units.

There is at least one term which may be ambiguous in its usage in this dissertation, because of inconsistencies in common usage in the literature. When "pulse compression" is discussed in this dissertation, it generally refers to a truncation of the lowest intensity portions of the pulse, due to threshold effects. This is consistent with use in several references. In contrast, the compression of chirped pulses in dispersive media is not truncation. Rather, it is the compression of the energy of a long pulse into a short pulse, increasing the peak power. No such effect was observed in these experiments.

Chapter 2. Apparatus and Measurement Techniques

2.A. Overview

In order to measure the accuracy of phase conjugation in focused stimulated Brillouin scattering (SBS) over a range of aberration strengths, we developed an apparatus and techniques to measure the following parameters:

- 1) The input and backscattered pulse temporal shape and spectral content.
- 2) The input and backscattered relative intensities, which give the reflectivity.
- 3) The input, aberrated, and reconstructed near field phases, giving the aberration strength and a measure of the phase reconstruction accuracy.
- 4) The far field intensity, including the intensity profiles and the reduction in focal intensity caused by the aberrator.
- 5) The "energy in the bucket" for the pump beam and the backscattered, reconstructed beam, giving the phase conjugate fidelity.

These are discussed in the following sections, but first we will discuss the laser, the beam train, and the SBS cell. After describing the diagnostics, we will discuss a phase grating optical aberrator, which provides easily and continuously variable aberrations with no optical elements to align.

2.B. Laser/SBS System

Recently, stimulated Brillouin scattering (SBS) has been observed at ultraviolet wavelengths.⁴⁵⁻⁴⁹ In order to observe competition between SBS and stimulated Raman scattering, we used the tripled output of a Q-switched YAG laser as our pump. The laser was a Q-switched, line-narrowed Neodymium YAG (Quanta-Ray DCR-2A (10)). The tripled laser output produced up to 250 millijoules in 6 ns (FWHM) pulses at 355 nm. An intracavity etalon reduced the bandwidth to less than 6 GHz⁴⁹ (typically 1.5 GHz or better). In order to provide single axial mode pulses, a specially timed trigger device (Electronic Line Narrower, or ELN) fired the Q-switch. The ELN partially opened the Q-switch, allowing relaxation oscillations to build up. Since each relaxation oscillation underwent many passes through the cavity, it was significantly narrower in linewidth than a normally Q-switched pulse. The ELN fired the Q-switch at the peak of the second relaxation oscillation,⁵⁰ producing single axial mode pulses approximately 50 percent of the time. Such techniques are commonly used to obtain single axial mode pulses from Q-switched lasers.⁵¹⁻⁵⁴ Using temporal and Fourier transform measurements, we found that the multimode pulses contained at most 5 axial modes, and the number of modes running varied from shot to shot. The cavity length L was 67 cm, giving a mode spacing of $c/2L=214\text{MHz}$. Thus, the multimode shots had less than 1.1 GHz overall bandwidth.

The laser had an unstable resonator, high gain oscillator and a single pass amplifier. The laser's output energy at 1.06 microns

could be changed by varying the flashlamp energy. The amount of third harmonic light could be changed by rotating the doubling and tripling crystals away from phase matching. We used a Pellin-Broca prism to separate the UV light from the fundamental and second harmonic light. At maximum lamp energy and optimum crystal alignment, 250 millijoules of 355 nm light were produced.

The near field and far field intensity profiles were strongly modulated just outside the laser. To calculate the focal intensity in the SBS medium, well-defined and easily analyzed intensity profile was produced. The beam was apertured from the original 9 mm to 3 mm, and spatially filtered using a 100 cm lens and a calibrated 300 micron diameter tungsten pinhole. The resulting beam was expanded to 3 centimeters in diameter, and then apertured to 1.5 centimeters. This provided nearly constant amplitude, nearly plane wave light (the Strehl ratio was interferometrically measured to be greater than 0.96). At most, 3 millijoules made it through the entire system and into the SBS cell. Still, this energy range allowed us to study SBS from threshold to 55 times threshold with accurate far field intensity diagnostics.

The SBS system consisted of a 20 cm focal length, antireflection coated ($R < 0.5\%$ per surface), plano-convex lens and a tube filled with HPLC grade hexane liquid. The tube, 20 cm long and 2 cm in diameter, was placed with the front window 10 cm from the lens. The reflectivity was independent of the distance from the lens to the cell unless the front or back window was within a centimeter of

focus. In that case, damage occurred to the window and the reflectivity dropped severely. The windows were "neutral solution treated" (Schott process) to be antireflective over a broad bandwidth. They had less than 2% reflectivity at 355 nm when used in the hexane-filled cell. The windows were tilted approximately 2 degrees from normal incidence so that specular reflections would be discarded. The lens and cell were arranged to collect all the diffracted light from the aberrator. We examined only the focused (no lightguide) geometry.

2.C. Temporal Pulse Shape and Spectrum Diagnostics

2.C.1. General

A fast photodiode and transient digitizer measured the temporal shape of the pump and Stokes pulses. A digital Fourier transform of the temporal data provided the frequency spectra of both pulses. The following paragraphs discuss the importance of laser linewidth on SBS gain, and the diagnostics used to measure pump and Stokes mode structure, mode beating, pulse compression, and SBS reflectivity.

There are three reasons that the gain of stimulated Brillouin scattering decreases as the pump laser linewidth increases. First, the gain coefficient explicitly depends on the pump linewidth.⁵⁶⁻⁵⁹ Second, if the pump coherence length is less than the interaction length, the gain is reduced.^{21,59} Finally, mode beating can produce intensity fluctuations shorter than the pulse width. These intense spikes can drive competing processes^{56,58,59} such as stimulated Raman scattering,^{8,59-64} stimulated Rayleigh scattering,⁶⁵ stimulated thermal scattering,⁶⁶ and optical breakdown.⁴⁸ In our experiment, the coherence length was always longer than the interaction length. Mode beating did produce intensity fluctuations shorter than the pulse width, and the data indicates that competing processes depleted gain from SBS during mode beating.

The Brillouin gain coefficient was reduced when the laser operated multimode. The gain coefficient's dependence on laser linewidth can be written^{21,56,59}

$$g(\Delta\nu) = \frac{C}{1 + \frac{(\Delta\nu_L)^2}{(\Delta\nu_B)^2}} \quad (2.C.1)$$

where C is a constant containing material parameters, $\Delta\nu_L$ is the laser linewidth, and $\Delta\nu_B$ is the Brillouin linewidth. For $\Delta\nu_L \ll \Delta\nu_B$ the gain is independent of the laser linewidth. When the laser linewidth equals the Brillouin linewidth, the gain coefficient is reduced by a factor of two. For $\Delta\nu_L \gg \Delta\nu_B$ the gain is inversely proportional to the square of the laser linewidth.

For typical Q-switched laser systems, the laser spectrum is composed of narrow bandwidth modes separated by the cavity mode spacing. If each mode has a narrow bandwidth, and the modes are spaced widely compared to the Brillouin linewidth, the SBS gain is independent of the number of modes.⁵⁹ The bandwidth of each mode is typically transform limited (approximately 27 MHz for our 6 ns pulses) and the mode spacing is $c/2L$ (214 MHz for our 67 cm cavity), where L is the cavity length. The Brillouin linewidth is given by

$$\Delta\nu_B = \frac{1}{2\pi\tau_B} = \frac{k^2\eta}{2\pi\rho} \quad (2.C.2)$$

where τ_B is the phonon lifetime, k is the pump wavenumber, η is the viscosity, and ρ is the density. For Hexane liquid pumped at 355

nm, the phonon lifetime is 180 ps and the Brillouin linewidth is 880 MHz.⁵⁶ In this case, each mode has a bandwidth much less than the Brillouin linewidth, but we cannot make the assumption that the mode spacing is much greater than the Brillouin linewidth. With 5 laser modes running, the overall laser linewidth (1.1 GHz) is slightly greater than the Brillouin linewidth. The SBS gain coefficient is reduced by a factor of $1+(1.1/0.88)^2$ or 2.6. This reduction in the SBS gain coefficient for multimode shots becomes important when competing effects such as stimulated Raman scattering occur.

2.C.2. Single Axial Mode Check

The laser used an Electronic Line Narrower to produce single mode pulses approximately 50 percent of the time. The Electronic Line Narrower, in addition to triggering the Q-switch, monitored the temporal profile of the Q-switched pulse and produced a data trigger signal whenever the pulse was "smooth". The temporal pulse shape was also measured using an avalanche photodiode (NRC Model 877) with less than 200ps rise/fall time,⁶⁷ and a high speed transient digitizer (Tektronix Model 7912AD with 7A29 and 7B10 plugins) with less than 500 ps rise/fall time.⁶⁸ The measurements showed that the trigger signal was generated whenever the Q-switched pulse had less than 5% modulation.

The spectral content of the "smooth" pulses was measured by digitally Fourier transforming the temporal data. The transient digitizer transferred data records to an HP 320 microcomputer, which created a data file of intensity values as a function of time (the sampling period was 2.56×10^{-11} sec). A Fast Fourier Transform program (HP Model 98827A Waveform Analysis Software⁶⁹) then analyzed this data file by calculating a discrete Fourier transform of the time data and plotting the intensity as a function of frequency. Smooth pulses have far less power in high-frequency components than multimode pulses. For example, a smooth pulse (less than 5% modulation) contains 20 times less power in the first sideband than a two-mode (43% modulated) pulse contains in its first sideband. The data trigger signal for "smooth" pulses occurred when the pulses had

more than 97% of their energy in a single mode. This is fairly consistent with other reported measurements of the modulation depth and mode structure of Q-switched laser pulses. Other researchers have predicted that if the ratio of the modulation depth to the average intensity is M , the ratio of the fundamental mode intensity to the sideband intensity should be $16/M^2$ (see Ref. 52). For a 5% modulation depth, the ratio of mode intensities is predicted to be 6.4×10^3 , and approximately 99% of the energy should be in the fundamental mode.

2.C.3. Mode Beating Measurements

Since the laser only ran single mode during approximately 50 percent of the shots, mode beating occurred during the other shots. The temporal and frequency replication of the pump pulse by the Stokes pulse was monitored during the mode beating shots. An optical delay was used to direct both signals into a single avalanche photodiode. In this way, the pump and Stokes pulses appeared on a single trace of the transient digitizer. The data were sent to the microcomputer and split into two data files. The first half of the trace contained the pump pulse. The second data file (the second half of the trace) contained the Stokes pulse. The Fourier transform was taken of each data file, and the Stokes spectrum was compared to the pump spectrum.

For pulses well above threshold, the temporal and spectral content of the Stokes pulse matched the temporal and spectral content of the pump pulse. The mode beating data verified that the temporal system could respond to signals with 400 picosecond rise times and fall times. The Fourier transform of this data showed that the system could respond to signals with bandwidths as high as 1.1 GHz. The data acquisition system had sufficient speed and bandwidth to measure pulse compression and laser mode beating effects.

2.D. Input and Backscattered Pulse Intensity (Reflectivity Measurements)

The high speed detection system measured the input and backscattered peak intensities, providing reflectivity data. A low reflection window (Schott "neutral solution" antireflection treated window with 1%R per surface) placed approximately one meter before the lens and SBS cell served as a beamsplitter (see Fig. 2.1). A mirror (M1) and a detector were placed on opposite sides of the beamsplitter, so that the beamsplitter directed the input pulse into the detector, and the mirror directed the backward traveling Stokes pulse into the detector. The system was calibrated by replacing the lens and cell with a calibrated (99%R) mirror (M2) and by rotating the beamsplitter and the mirror M1 to give equal pump and reflected intensities. The mirror M2 was then removed and the lens was reinstalled. The SBS reflectivity was calculated from the ratio of the backscattered pulse peak intensity to the input pulse peak intensity. The lens and SBS cell window were antireflection coated, and passed more than 99 percent of the input and backscattered light. The reflectivity data were repeatable to better than 10 percent.

It is important to note that the reflectivity data are measures of the intensity, not the energy. In fact, it would be possible to have an intensity reflectivity greater than unity if significant pulse compression⁷⁰⁻⁷² occurred (the energy reflectivity is always less than unity). However, our measurements show that pulse

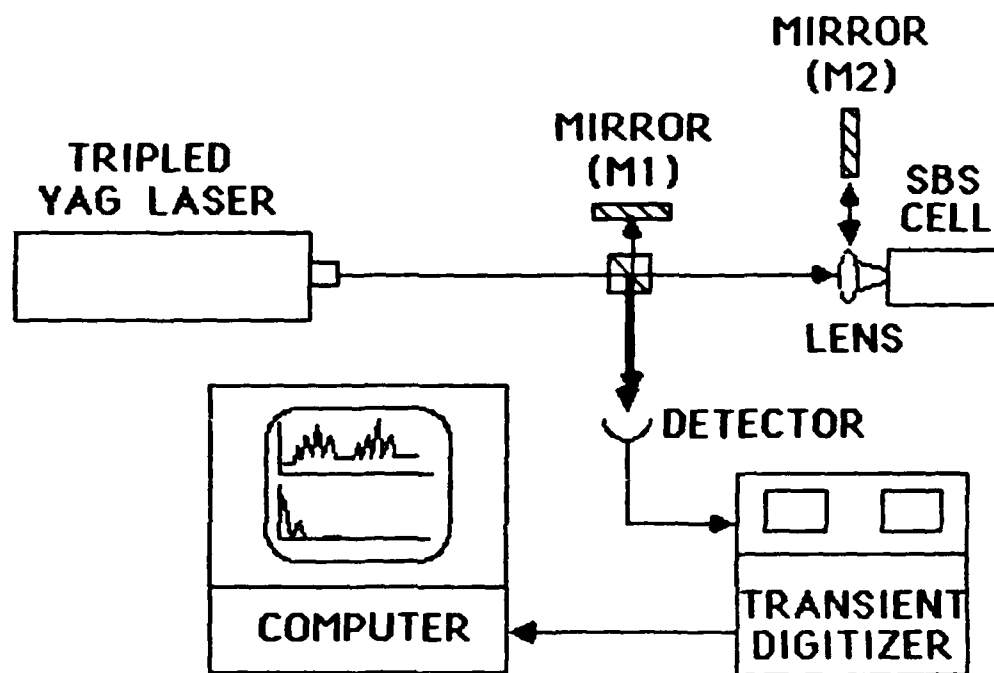


Figure 2.1 Schematic of the time-resolved intensity diagnostics and optical layout.

compression is only significant for pulses near threshold intensity (where the reflectivity is much less than unity). More will be said about pulse compression in the data and analysis section.

To summarize, the time-resolved data acquisition system provided accurate measurements of pulse compression, mode beating, and reflectivity. This system provided the first direct measurements of subnanosecond SBS gain depletion caused by mode beating within a pulse. The temporal resolution was sufficient to monitor the mode beating and pulse compression which occurred. The system provided SBS reflectivity values which were repeatable to better than 10 percent.

2.E. Near Field Phase

Two-axis lateral shearing interferometry directly measured the input, aberrated, conjugated, and reconstructed wavefronts. Fig. 2.2 is a schematic of the optical layout, emphasizing the position of the two shear plates. When placed before the aberrator, they could measure the input beam phase and the reconstructed beam phase, for the two beams traveling in opposite directions. When placed between the aberrators and the SBS cell, they measured the aberration strength. The interferometric measurements of the input, aberrated, and reconstructed beam Strehl ratios determined the phase reconstruction accuracy.

Lateral shearing interferometry is discussed in Ref. 73. It is a self-referencing interferometric technique, combining the front and back surface reflections of an optical flat or wedge to give fringes in an overlap region which is a subaperture of the overall wavefront (see Fig. 2.3). The fringes generate the derivative of the wavefront in the direction of shear,⁷³ so two axes of lateral shear are required to determine the wavefront. In order to calculate the wavefront from the interferograms, a VAX computer program called SAINT was used. The fringes for each transverse axis were digitized, and the data was input to the computer program. SAINT then calculated the wavefront, and plotted it in a pseudo 3-dimensional plot. The two shear axes, which were perpendicular to the propagation direction, were two of the axes on the plot. The optical

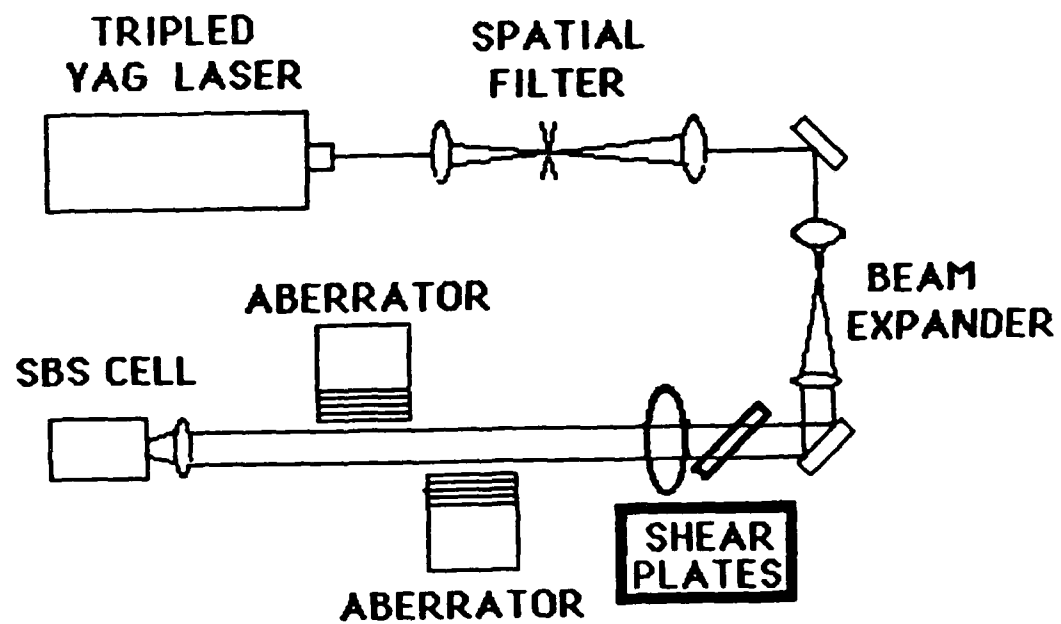


Figure 2.2 Schematic of the shearing interferometry optical layout.

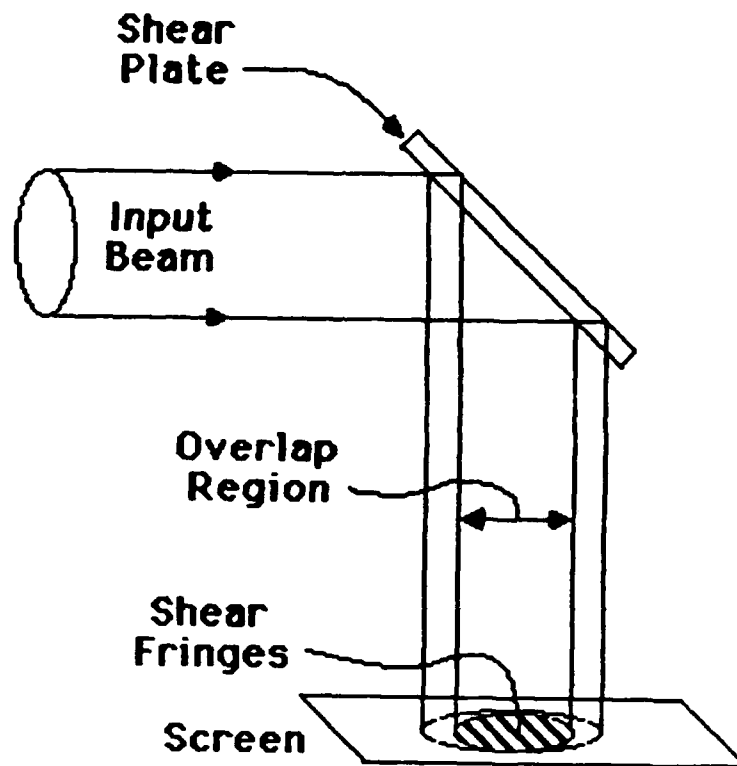


Figure 2.3 Lateral shearing interferometry. Front and back surface reflections interfere, giving fringes in the overlap region.

path difference was plotted on the third axis. SAINT also calculated the peak to valley and root mean square (RMS) optical path difference and the Strehl ratio.⁷⁴ Assuming a constant amplitude beam, if we let ϕ_{RMS} be the RMS optical path difference (in waves) and S be the Strehl ratio, then

$$S = \exp[-(2\pi\phi_{\text{RMS}})^2] \quad (2.E.1)$$

The wavefronts and the Strehl ratios of the input, aberrated and reconstructed beams gave quantitative measurements of the accuracy of phase reconstruction using SBS. However, these measurements are different from measurements of the phase conjugate fidelity F, as defined in chapter 1. Recall that for any z_0 outside the gain medium,

$$F = \text{const} = \frac{|\int dx dy E_L(x, y, z_0) E_S(x, y, z_0)|^2}{\int dx dy |E_L(x, y, z_0)|^2 \int dx dy |E_S(x, y, z_0)|^2} \quad (2.E.2)$$

Note that the overlap integral takes into account both the phase and the amplitude of the fields at z_0 . In contrast, the interferometrically generated Strehl ratios assume constant amplitude beams, and only measure the effect of the phase. Although the interferometrically generated Strehl ratios give accurate phase reconstruction data, they overestimate the fidelity F because they do not take into account the reduction in fidelity due to amplitude fluctuations.

It was not possible to separate the near field phase data for single mode shots from the data for multimode shots. Also, the time required to digitize the fringes (approximately 1 hour) and reduce the wavefront (10-15 minutes to run, 1/2 hour to retrieve plots) strongly limited the number of samples taken. Thus this technique was only used in the early phases of the experiment, and as a baseline to cross check the far field video and energy in the bucket measurement systems.

2.F. Far Field Intensity Profiles

A computerized far field image analysis system directly measured the reduction in the focal intensity due to aberration. A schematic of the far field image analysis system is shown in Fig. 2.4. Beamsplitters and mirrors directed light into the lenses and camera. Sampling the beam between the SBS cell and the aberrator gave a measure of the degree of aberration, and sampling the beam after it was conjugated and passed back through the aberration gave a measure of the phase conjugate fidelity.

The system consists of beamsplitters and mirrors (flat to $\lambda/10$) directing light through an antireflection coated lens doublet. The doublet had a variable focal length, from 60 cm to over 2 m. Typically, the focal length was kept at 120 cm. The lenses focused the light directly onto the focal plane of a General Electric Model TN2505 Charge Injection Device (CID) array video camera. The CID array camera is designed to have minimum dead space between pixels. The far field spots produced by our laser were always three or more pixels wide and high, so more than 6 pixels were illuminated by every spot. This minimized potential problems with discrete pixels missing far field data. The camera was operated with an inject/inhibit circuit to trigger a scan for each single axial mode shot. The focal plane contained 242 vertical by 377 horizontal active pixels in an array measuring 0.66 cm by 0.88 cm, for an effective pixel size of $27.3 \mu\text{m}$ by $23.3 \mu\text{m}$. The camera's response linearity (in amps per watt) was better than 2% for intensities ranging from 1% of

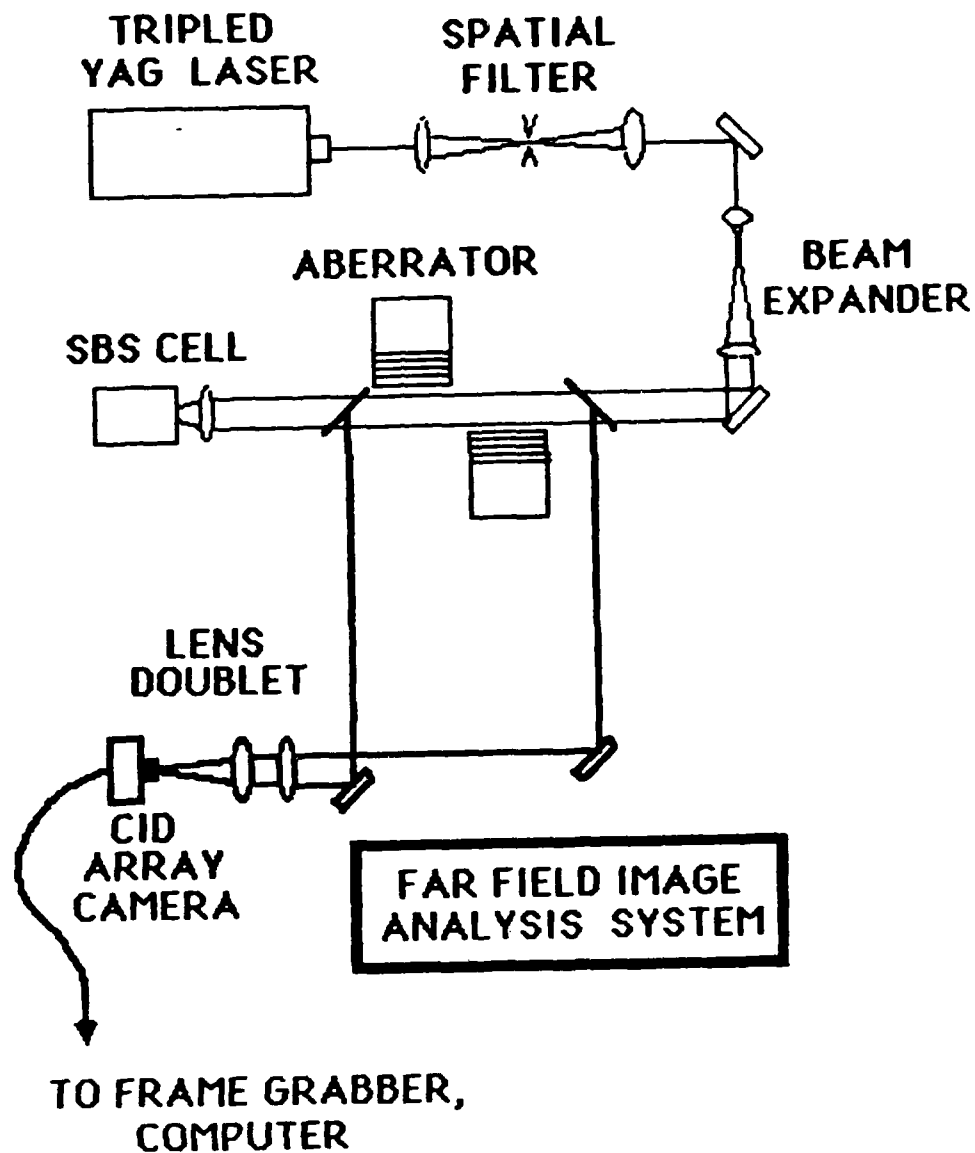


Figure 2.4 Schematic of the far field intensity analysis system and optical layout.

saturation to 95% of saturation.⁷⁶ The camera was always operated below the saturation intensity. We used neutral density filters placed within 10 cm of the focal plane to reduce the intensity to below the camera's saturation intensity.

A Poynting Model 505 frame grabber digitized and stored the video output from the camera. The frame grabber had 8-bit resolution,⁷⁷ giving better than 0.4% precision. The frame grabber had memory capacity to store 256 horizontal by 256 vertical pixels, but since the camera had 242x377 pixels, there were 14 unused rows of storage, and 121 unstored columns of camera data. The grabber stored the first 256 columns of camera data, and transferred the data to a Hewlett Packard Model 320 microcomputer. A program called MULTI processed the image data and plotted the intensity profiles using a Hewlett Packard Model 82906A printer.⁷⁸ Figs. 2.5 and 2.6 are typical plots of the unaberrated and the aberrated intensity distributions. These intensity distributions are in good agreement with calculated far field intensity profiles due to sinusoidal phase gratings (see Section 2.H.3).

The intensity of the brightest aberrated spot (not the average intensity) divided by the intensity of the unaberrated spot was used in measurements of the reduction in focal intensity caused by aberrations. The brightest spot was used because it has been demonstrated experimentally that the intensity of the brightest spot controls the SBS reflectivity.⁷⁹ Theory predicts that the brightest spot also controls the SBS phase conjugate fidelity.⁸⁰

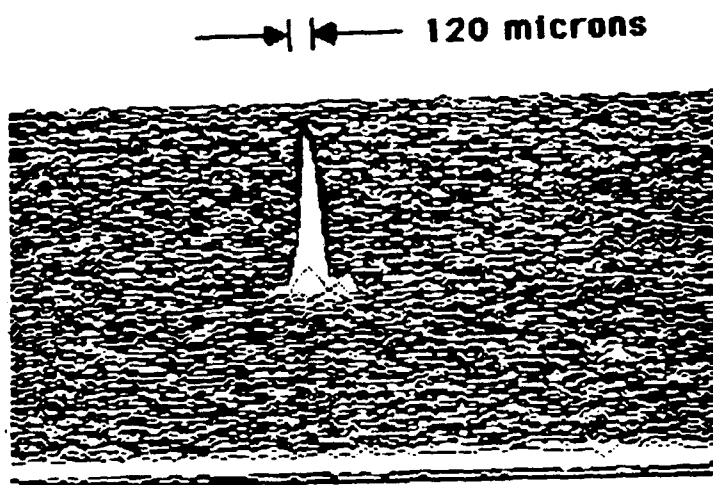


Figure 2.5 Unaberrated far field intensity distribution.

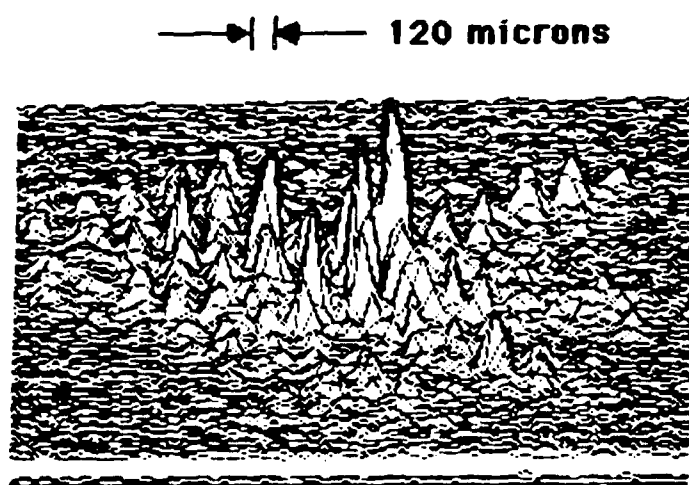


Figure 2.6 Aberrated far field intensity distribution.

Calibrated neutral density filters controlled the light level into the camera. When the beam was severely aberrated, neutral density filters were removed so as to increase the intensity at the camera. The camera's linear response gave voltage measurements that were proportional to the intensity. The reduction in the focal intensity due to aberration is

$$\frac{I_{ab}}{I_{dl}} = \frac{(V_{ab} - B)}{(V_u - B)} \times N.D. \quad (2.F.1)$$

where I_{ab} is the aberrated intensity, I_{dl} is the unaberrated (diffraction limited) intensity, V_{ab} is the peak voltage level of the video signal for the brightest aberrated spot, V_u is the peak voltage level of the unaberrated spot, B is the background voltage, and $N.D.$ is the transmissivity of filters removed to observe the aberrated beam. We found that our laminar heated air aberrator could produce up to a 34-fold reduction in the focal intensity of the brightest aberrated spot.

The focal intensity reduction produced by the variable aberrator changed by as much as 30% from shot to shot for a given aberrator setting, so ten shots were averaged for each aberrator setting. The variance of this average is $\sqrt{10}$, or approximately a factor of 3 smaller than the variance of the individual measurements. The average value of the focal intensity reduction is therefore accurate to approximately 10%. These measurements were made at several aberration strengths, providing a wide range of focal

intensities. The data on the focal intensity reduction due to aberration will be presented in section 2.H.

2.G. "Energy in the Bucket" Fidelity Diagnostic

Since energy measurements are easy to obtain and require very little data reduction time, they are ideal for data acquisition. A spatial filter and two energy meters were used to measure the fraction of the backscattered (Stokes) beam which was transmitted through the pinhole (see Fig. 2.7). For backscattered beams which are at least partially reconstructed (Strehl ratio greater than 0.2) the energy in the bucket measurements give the Strehl ratio of the backscattered beam. The Strehl ratio of a laser beam is defined as the ratio of the beam's far field intensity to the far field intensity of a diffraction limited beam of the same near field spot size and power.

$$S = \frac{I}{I_{dl}} \quad (2.G.1)$$

If the pump beam is diffraction limited, the Strehl ratio of the Stokes beam equals the phase conjugate fidelity.⁴⁴ Our pump beam was nearly diffraction limited. Its Strehl ratio was greater than 0.96.

The energy in the bucket is a measure of the far field focusability of a laser beam. It is generally defined as the encircled energy contained within the first dark ring of an Airy pattern. If we define $L(w)$ as the fraction of the energy contained in a circle of radius w for an Airy pattern produced by focusing a

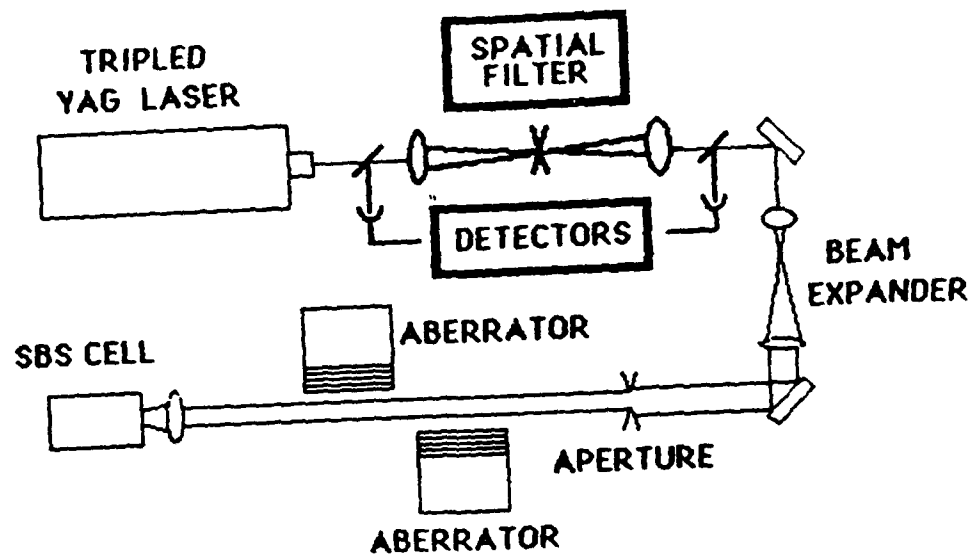


Figure 2.7 Energy in the bucket optical layout.

constant amplitude plane wave to the far field, we have⁸¹

$$L(w) = 1 - J_0^2(kaw) - J_1^2(kaw) \quad (2.G.3)$$

where a is the unfocused beam radius

k is the wavevector

$J_{0,1}$ are the 0th and 1st order Bessel functions

This function is plotted in Fig. 2.8 (dotted line). The first point of inflection (at the point of intersection with the right vertical dashed line in Fig. 2.8) corresponds to the first dark ring in the Airy pattern. The energy in the bucket is the encircled energy at that point. For a diffraction limited beam, the energy in the bucket is 84 percent of the total energy.

Compared to a diffraction limited beam, an aberrated beam has an increased spot size, and decreased energy in the bucket. In Fig. 2.9, Airy patterns with varying sizes but constant integrated intensities are plotted. It is apparent that there is less energy in the bucket and lower on-axis intensity (Strehl ratio) for the "aberrated" spots. Fig. 2.8 shows plots of encircled energy for several different sized spots. We see that the bigger spots have less encircled energy at the bucket point, so they would transmit less energy through a "one Airy bucket" pinhole.

We note that a "one Airy bucket" pinhole is not the best choice for Strehl ratio measurements, because the energy in the bucket is

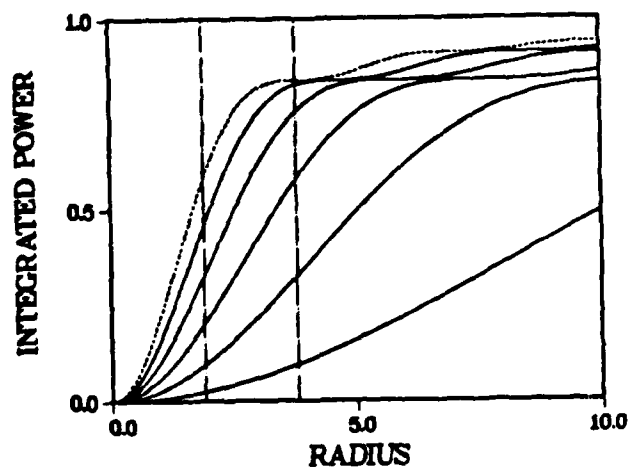


Figure 2.8 The encircled energy is plotted as a function of the radius, for several spot sizes.

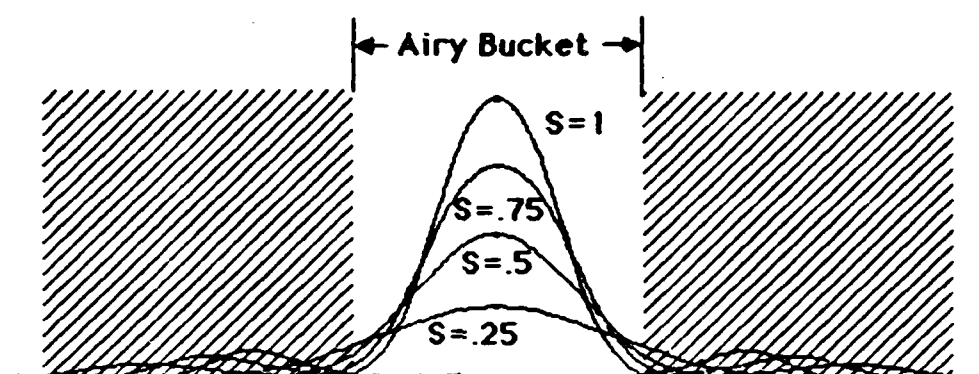


Figure 2.9 Normalized far field intensity profiles for several spot sizes.

is not proportional to the Strehl ratio. Fig. 2.10 is a plot of the Strehl ratio versus energy in the bucket for a one Airy bucket pinhole (solid line). The data points in Fig. 2.10 were generated by calculating the energy in the bucket for the "aberrated" spots represented by the curves in Fig. 2.8.⁸² It is apparent that the data in Fig. 2.10 do not fit a model which predicts the Strehl ratio to be linearly proportional to the energy in the bucket.

Now, let us define the "bucket" as half the diameter of the first Airy ring for the unaberrated beam. A small bucket is chosen because it gives an encircled energy which is nearly proportional to the Strehl ratio (see Fig. 2.11). For a diffraction limited beam, approximately 60% of the energy makes it through a pinhole which is half an Airy bucket in diameter (left vertical dashed line in Fig. 2.8). Aberrated beams pass proportionately less energy (see Fig. 2.11). In order to obtain the Strehl ratio, it is necessary to normalize the encircled energy fraction. The normalization factor is $1/0.6$ or 1.67 . A diffraction limited beam will have a normalized encircled energy fraction of 100%, and a Strehl ratio of 1.0. From this point forward, we define "energy in the bucket" as the normalized encircled energy fraction for a half Airy bucket pinhole. These measurements give the Strehl ratio of the phase conjugate beam, which equals the phase conjugate fidelity.

Measurements of the phase conjugate fidelity using this energy in the bucket diagnostic were simple (see Fig. 2.7). Light from the

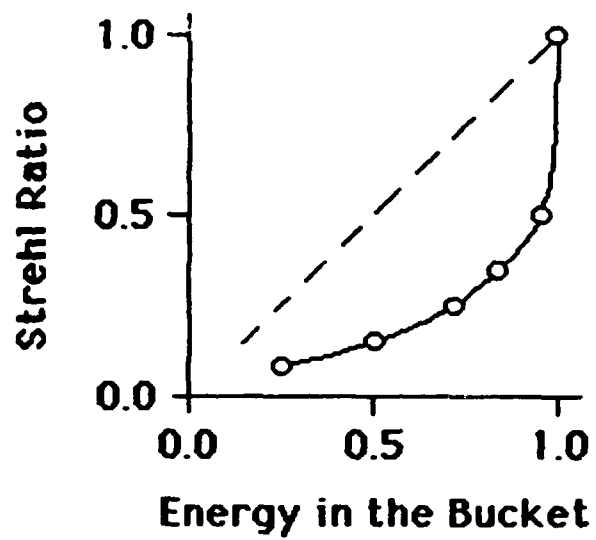


Figure 2.10 The Strehl ratio is plotted versus the normalized energy in the bucket for a one Airy bucket pinhole. Note the nonlinear dependence.

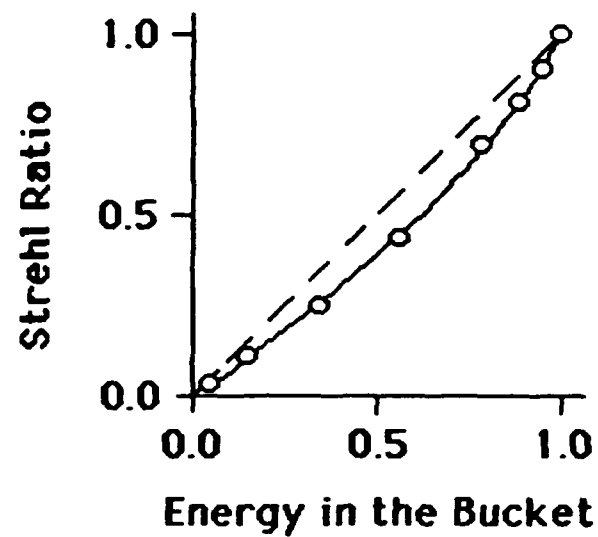


Figure 2.11 The Strehl ratio is plotted versus the normalized energy in the bucket for a half Airy bucket pinhole. The dependence is nearly linear.

laser was spatially filtered by the pinhole, and beam expanded by a factor of 10, giving a 3 centimeter diameter central bright spot. This spot was apertured to 1.5 centimeters in diameter, providing a nearly constant amplitude beam. The beam was aberrated, conjugated, reconstructed, and focused back through the spatial filter. Because the beam had been apertured to half its original size, it focused to a spot twice as big as the pinhole. This effectively gave a half Airy bucket pinhole. The beam's Strehl ratio was simply the normalized energy ratio at the two detectors. The ratiometer was triggered only for single axial mode pulses, so all of the energy in the bucket data is limited to the single axial mode case.

The experimental normalization was performed by directing apertured, diffraction limited light (verified with shearing interferometry) back through the pinhole and measuring the "energy in the bucket". A calibrated pair of energy meters (Laser Precision Model Rj-7200 Energy Ratiometers) was used to make the measurements. The reciprocal of the transmitted energy fraction was the experimental normalization factor. This normalization factor depended on the reflectivity of the beamsplitters used. For identical beamsplitters set to identical angles, the theoretical normalization factor would be $1/0.6$, or 1.67. For our beamsplitters set to fixed angles, the experimental normalization factor was 1.3. This normalization factor is accurate to approximately 10 percent. All the fidelity data was multiplied by the experimental normalization factor.

The accuracy of this measurement technique can be estimated by examining systematic and random error contributions. From Fig. 2.11, it is clear that the energy in the bucket for a half Airy bucket pinhole is nearly linearly proportional to the Strehl ratio. The root mean square deviation of the points in Fig. 2.9 from the straight line fit is 4 percent. The experimental normalization was accurate to approximately 10 percent. Random errors were minimized by averaging 100 shots at each power and aberation setting. The averaged data was typically repeatable to ± 4 percent. The square root of the sum of the squares of these errors is 11.5 percent. Thus, the fidelity data measured by this technique is accurate to better than 12 percent.

To summarize this section, energy in the bucket measurements gave the Stokes beam Strehl ratio, which equals the phase conjugate fidelity. This technique gave rapid, accurate measurements of the fidelity, without extensive data reduction.

2.H. Variable Phase Grating Aberrator

2.H.1. General

In order to study the fidelity of phase conjugation, it is desirable to use a variable aberrator. Low order Seidel aberrations can be produced using conventional optical machining techniques, and high spatial frequency random phase aberrators have been produced by etching glass in hydrofluoric acid. These aberrators cannot be varied in strength or spatial frequency without physically moving optical elements in the beam train. As part of a study of the effect of intracavity aberrations on laser beam quality, K.R. Calahan designed and built a variable optical aberrator.⁸³ Recently, we analyzed the aberrator's performance,⁸⁴ comparing it to a sinusoidal phase grating.^{85,86} In this section, the aberrator design and performance are presented.

2.H.2. Optical Layout and Aberration Measurement Technique

The aberrator consists of a fan which blows air through honeycomb channels, then over heated wires. Fig. 2.12 is a schematic drawing of the aberrator. A commercial 10 cm diameter "muffin fan" blows air into the honeycomb structures. The honeycomb material is 5 cm thick with 0.5 cm wide hexagonal structure and provides nearly laminar airflow. The air flows past nichrome wires, which are stretched in a grid with approximately 0.6 cm separation. The wires are heated by adjusting the current through them with a variac. The heated air flows perpendicular to the beam axis, producing aberrations. Two crossed aberrators produced aberrations in both transverse axes. The beam traverses approximately 10 cm along each aberrator, accumulating up to 2.1 waves of optical path difference in each axis.

A schematic of the optical layout for analyzing the aberrator is shown in Fig. 2.13. After spatial filtering and beam expanding, the collimated 355 nm light passed along both aberrators, and into the diagnostics. The diagnostics included lateral shearing interferometry and far field intensity analysis, as discussed in sections 2.E and 2.F. The strength and spatial frequency of aberration were cross checked using the near and far field diagnostic systems.

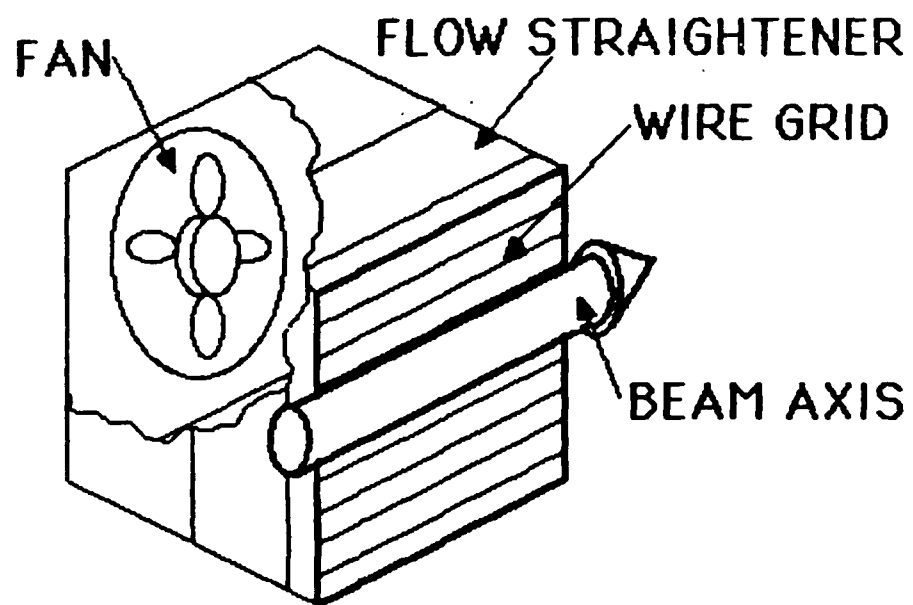


Figure 2.12 Variable aberrator.

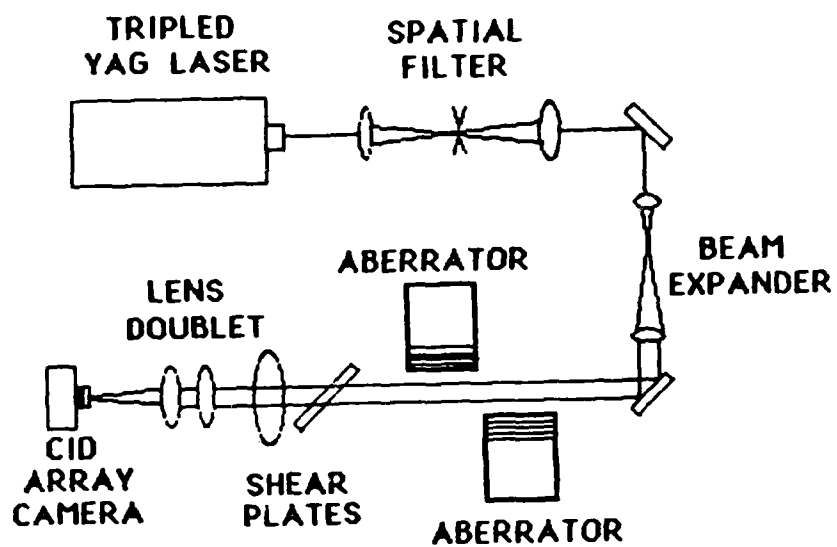


Figure 2.13 Schematic of the aberrator analysis optical layout.

2.H.3. Aberration Data

The near field phase data show nearly sinusoidal transverse phase modulation. Since our interferogram reduction software could only produce plots of the optical path difference (OPD) along axes at 45° to the aberrator axes, the number of cycles along the aberrator axes and their spatial frequency are reduced in the following plots by a factor of $\sqrt{2}$, or approximately 1.4. Bearing this in mind, quantitative values of the aberration strength, spatial frequency, and sinusoidal nature were derived from the plots. Fig. 2.14 shows typical plots of the OPD in one of the transverse axes for three different aberrator current settings. Fig. 2.15 shows sinusoidal curves fit to the data. The fit is quite good: the measured OPD is sinusoidal to approximately 10%. By varying the current through the wires, the phase front was modulated by up to 2.1 waves (peak to valley). Table 2.1 gives the peak to valley (P-V) and root mean square (RMS) OPD and the interferometrically generated Strehl ratios, for beams passing twice through the aberrator.

Using the theory of sinusoidal phase gratings,⁸⁶ the reduction in focal intensity due to various amounts of aberration was predicted. The phase grating theory predicts a roughly $1/\xi$ reduction in focal intensity for 2 axes of aberration, where $\xi = \theta/\theta_{d1}$ is the ratio of the far field divergence θ to the diffraction limited far field divergence θ_{d1} . The reduction in the focal intensity was measured using the far field image analysis system described in section 2.F.

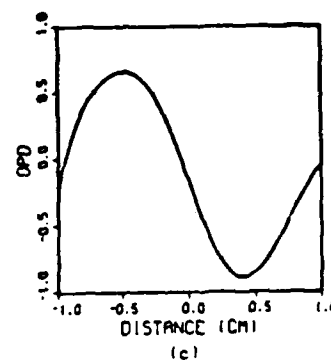
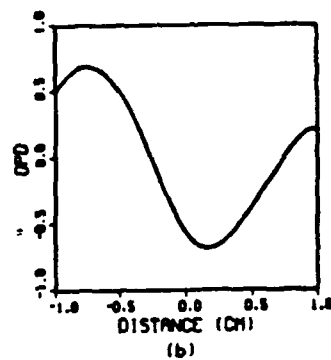
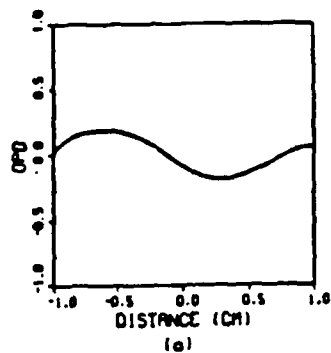


Figure 2.14 Plots of the measured optical path difference across the wavefront.

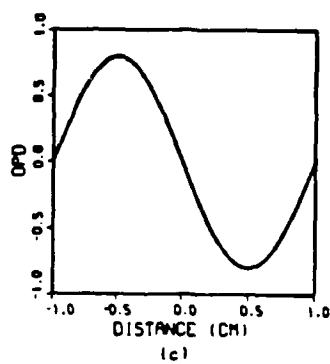
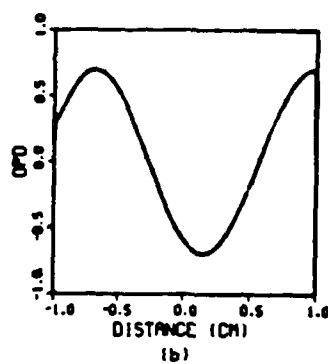
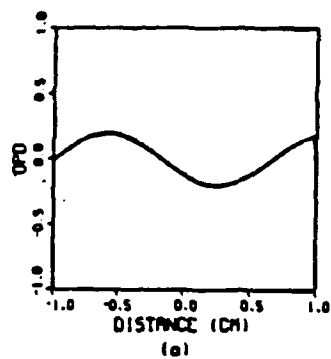


Figure 2.15 Sinusoidal fits to the data in Fig. 2.14.

Table 2.1

Aberrator OPD and Strehl Ratio Data: Double Pass

Aberrator 1 Voltage	Aberrator 2 Voltage	OPD (P-V)	OPD (RMS)	Strehl Ratio
0	0	0.15	0.03	0.95
0	10	0.22	0.05	0.89
10	0	0.19	0.05	0.91
10	10	0.19	0.04	0.92
0	20	0.64	0.13	0.52
20	0	0.47	0.10	0.65
20	20	0.77	0.15	0.40
0	30	0.73	0.18	0.28
30	0	0.56	0.15	0.40
30	30	1.35	0.28	0.05
0	35	1.32	0.35	0.007
35	0	0.93	0.22	0.15
35	35	1.35	0.26	0.07

Table 2.2 gives the OPD's, Strehl ratios, and the measured and phase grating-predicted values of the reduction in focal intensity due to a single pass along the aberrators, with selected current settings. The numbers in the parentheses were extrapolated from double pass measurements. In Fig. 2.16, the phase grating-predicted and measured values of the diffraction limited intensity divided by the aberrated intensity, and the observed divergence are plotted as functions of the aberrator voltage. Fig. 2.17 is a plot of the measured and predicted values of the focal intensity reduction of the brightest aberrated spot, along with a $1/\xi$ curve, plotted versus the measured divergence ratio ξ . The data is in fair agreement with the phase grating theory, though the intensity is greater than predicted for $1.5 < \xi < 10$. The direct measurement of the reduction in focal intensity due to aberration allowed us to study, plot, and model the reflectivity and fidelity of focused SBS as functions of the aberrated focal intensity.

In summary, the variable phase grating aberrator produced variable strength, nearly sinusoidal aberrations in either or both transverse axes. The aberrator produced up to a factor of 34 reduction in focal intensity, in rough agreement with the sinusoidal phase grating theory.^{84,85} The main drawback of the aberrator is that it produces relatively low spatial frequency (1.5 to 2 per cm) aberrations. Still, the easily and continuously variable modulation depth makes this aberrator useful for many optical experiments,

Table 2.2

OPD, Strehl Ratio, and Predicted and Measured Focal Intensity

Reductions: Single Pass

Aberrator 1 Voltage	Aberrator 2 Voltage	OPD (P-V)	OPD (RMS)	Strehl Ratio	I_{d1}/I Pred.	I_{d1}/I Meas.	$\xi = \theta/\theta_{d1}$
0	0	(<0.14)	(0.03)	(0.95)	(1)	1	1
10	10	(0.175)	(0.04)	(0.94)	(1.16)	1.05	1.3
20	20	(0.35)	(0.09)	(0.73)	(3.5)	2.25	3.5
30	30	0.72	0.15	.41	11.4	5.5	9
40	40	1.65	0.36	.006	43.5	18.2	11
50	50	2.1	0.43	6.7×10^{-4}	52.6	28.6	21
60	60	2.1	0.54	10^{-5}	52.6	33.9	24

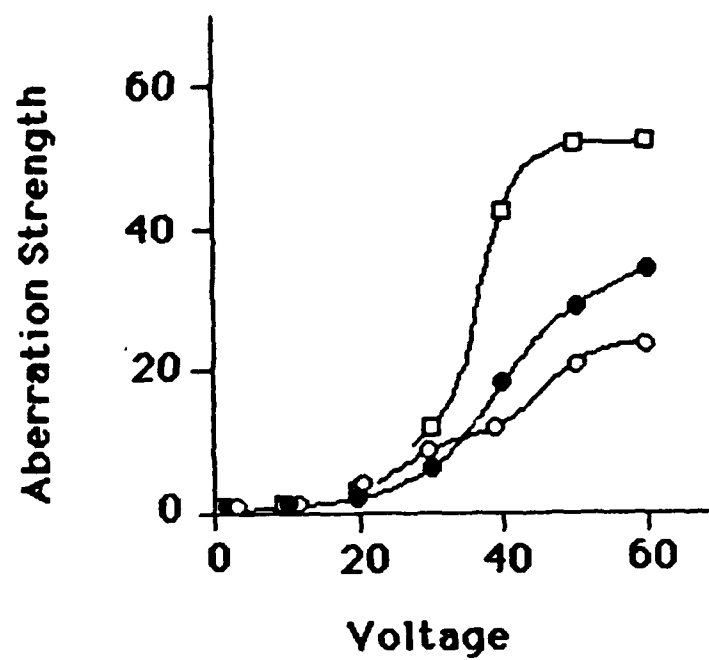


Figure 2.16 The aberration strength is plotted as a function of the aberrator voltage. \square --phase grating theory, \bullet --data (I_{d1}/I), \circ --data (θ/θ_{d1}).

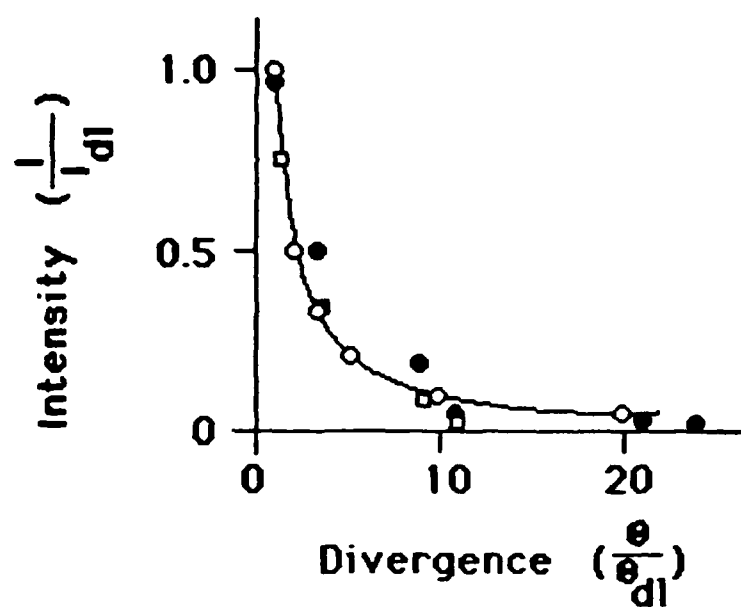


Figure 2.17 The measured and predicted intensity reduction, and the reciprocal of the divergence are plotted versus the measured divergence. □--phase grating theory, ●--data (I/I_d), ○-- $1/\text{divergence}$.

including wavefront reproduction accuracy in phase conjugation. The sinusoidal wavefront simplifies analysis, so the aberrator is both easy to use and easy to analyze.

Chapter 3. Data and Analysis

In this chapter, the published experimental results on the fidelity of phase conjugation in focused stimulated Brillouin scattering (SBS) are presented first. Then, results from the experiments which were done for this dissertation are discussed.

3.A. Summary of Published Experimental Data

The following effects have been reported in the literature regarding the behavior of SBS. Except as noted, these results are experimental.

- 1) Temporal and spectral effects have been studied intensively.
 - a) SBS can compress Q-switched laser pulses to less than a nanosecond.⁷⁰⁻⁷²
 - b) If stimulated Raman scattering (SRS) has a steady state gain coefficient almost as large as the steady state SBS gain coefficient, gain switching from SBS to SRS can occur during short pulses.⁶⁰⁻⁶⁴
 - c) Mode beating⁸⁷⁻⁹¹ can also cause gain switching from SBS to SRS.^{58,59} However, there are no published reports of time-resolved measurements of gain switching within mode beating pulses.
 - d) If the pump consists of a train of short pulses separated by less than a phonon lifetime, SBS can step up pulse by pulse to a quasi-steady state value.^{92,93}
 - e) If the pump spectrum consists of narrowband spikes separated by more than the Brillouin linewidth (1/phonon lifetime), the SBS reflectivity is independent of the number of pump modes, and the number of Stokes modes equals the number of pump modes.^{58,59}
 - f) If the pump operates broadband, the SBS reflectivity declines.^{21,56,59}

- 2) If two beamlets enter the SBS medium, the reflectivity is controlled by the focal intensity of the brighter beam.⁷⁹ Theoretical studies predict that the phase conjugate fidelity of the weaker beam is the same as the fidelity of the stronger beam.⁸⁰
- 3) The threshold power for focused SBS increases roughly linearly with increasing aberration strength.³⁷
- 4) For low pump powers,⁴² or for pump pulses shorter than a phonon lifetime,³⁸ increasing the aberration strength decreases the phase conjugation fidelity, both for random aberrations^{37,38,42,43} and for astigmatism.³⁸ None of the experiments measured the phase conjugate fidelity versus the focal intensity.
- 5) Accurate phase conjugation in focused SBS has been observed for beams with $1 \leq \xi \leq 1000$, where ξ is the aberrated beam's far field divergence divided by the diffraction limited divergence.^{26,37,38,41-44} None of the experiments showed a minimum divergence for accurate phase conjugation.
- 6) For diffraction limited beams with focal intensities well above the SBS threshold, the phase conjugation fidelity decreases approximately 10% for a two order of magnitude increase in the pump power.^{38,41-43}
- 7) Increasing the aberration strength qualitatively increases the resolution of image reconstruction by focused SBS.^{40,94} This may be because increasing the aberration strength increases the overlap of different spatial frequencies at the image's focus within the SBS medium. Experiments and theory have shown enhanced phase conjugate fidelity when beamlets

in an SBS medium were aberrated in order to overlap at the focus.^{95,96} Note that image reconstruction accuracy is distinct from the phase conjugation fidelity, and that images can be "poorly" reconstructed even when more than 90% of the backscattered light is conjugated.⁴⁴ In other words, a nonconjugate fraction of less than 10% can cause large intensity modulations, giving qualitatively "poor" image reconstruction.

The experiments for this dissertation were organized to resolve questions concerning the minimum and maximum aberration strength for accurate WFR in focused, steady state SBS. The experiments concentrate on focal intensity effects, which have not been reported in the literature. The effect of the pulsewidth on the phase conjugation fidelity was beyond the scope of this dissertation, though we did investigate the influence of mode beating and pulse compression on the reflectivity. Image reconstruction accuracy was also beyond the scope of the dissertation.

3.B. Temporal and Frequency Effects

3.B.1. Overview

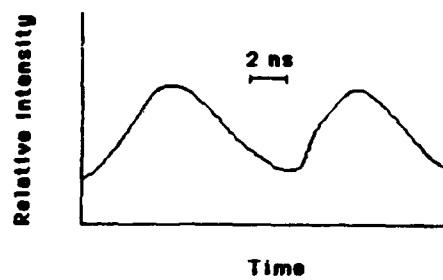
Our temporal and spectral data acquisition system was described in section 2.C. The temporal system had rise and fall times of less than 400 picoseconds. The Fourier transform system had a resolution of 100 MHz, and a nominal bandwidth of 1-1.5 GHz. We measured the pulse compression versus the focal intensity, and found increasing pulse compression as the intensity was reduced to near the SBS threshold. We also measured mode beating effects for pulses at approximately 30 times the SBS threshold intensity. The Stokes pulse replicated the temporal and spectral structure of the pump pulse, except when the pump's mode beating intensity spikes caused competing processes to deplete gain from SBS. During fast, intense mode beating, the Stokes pulse replicated only part of the pump pulse. Backward and forward stimulated Raman scattering were observed on some multimode shots.

3.B.2. Pulse Compression

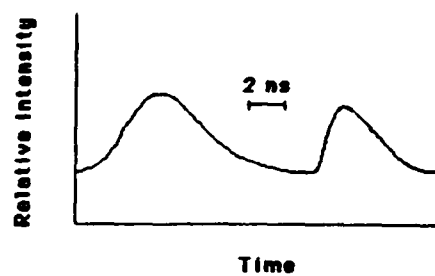
Pulse compression was studied as a function of the pump energy for unaberrated, single axial mode pulses. In Fig. 3.1, oscillographs of the pump and Stokes intensities versus time are presented. In the pulse shown in Fig. 3.1(a), approximately 1.1 millijoule entered the SBS cell, giving 25 times threshold intensity; approximately 0.36 mJ ($I=8I_{th}$) entered the cell in (b); and approximately 0.18 mJ ($I=4I_{th}$) entered the cell in (c). The SBS threshold occurred at 0.045 ± 0.005 mJ. The Stokes pulses were compressed relative to the pump pulses, with increasing compression as the pump energy declined.

Table 3.1 gives the values of the pump and Stokes pulsewidths and compression as functions of the energy and the intensity over the SBS threshold. In Fig. 3.2, the pump and Stokes pulsewidths (FWHM) are plotted versus the input intensity divided by the threshold intensity. The Stokes pulse was uncompressed for a pump pulse with 25 times threshold intensity, compressed by a factor of 0.62 for a pump pulse with one third that intensity, and compressed by a factor of 0.42 for a pump pulse with 4 times the SBS threshold intensity.

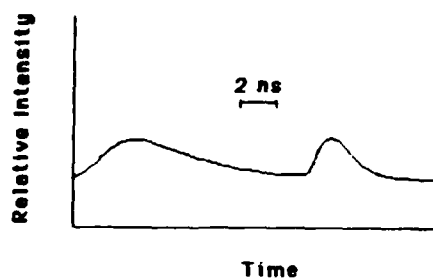
A phenomenological model for pulse compression can be constructed using the intensity versus time data and the reflectivity data.



(a)



(b)



(c)

Figure 3.1 Pump and Stokes intensities versus time (oscilloscographs.)

(a) $--I=25I_{th}$, (b) $--I=8I_{th}$, (c) $--I=4I_{th}$.

Table 3.1
Pump and Stokes Pulsewidths

Energy (mJ)	I/I_{th}	Type	Pulsewidth (ns)	Compression (t_s/t_p)
1.0	25	Pump	5.1	----
----	----	Stokes	5.1	1.0
0.34	8	Pump	5.3	----
----	----	Stokes	3.3	0.62
0.15	4	Pump	5.5	----
----	----	Stokes	2.2	0.40

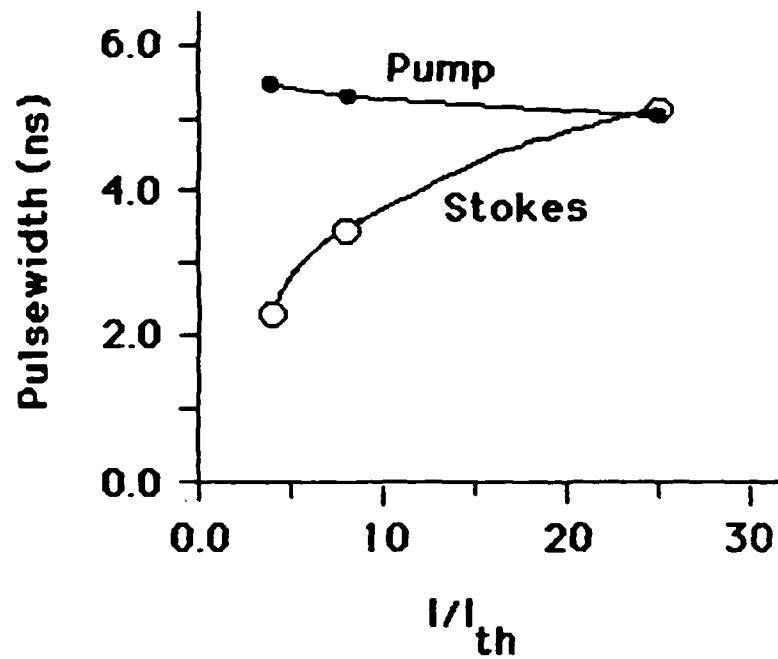


Figure 3.2 The pump and Stokes pulsewidths (FWHM) are plotted versus the input intensity divided by the threshold intensity.

model, the Stokes intensity as a function of time is assumed to be equal to the pump intensity times the SBS reflectivity.

In Fig. 3.3(a) the normalized pump intensity for the shot with 25 times threshold intensity is plotted versus time (upper trace). The lower trace is the predicted Stokes intensity derived from the simple pulse compression model. The predicted Stokes intensity has a maximum value of 0.62 because that is the SBS reflectivity at 25 times threshold intensity. The predicted Stokes intensity at each point equals the pump intensity times the SBS reflectivity for that pump intensity. The Stokes pulse in this model has FWHM=4.65 ns. Comparing this model to the data in Fig. 3.1(a) we see that the actual Stokes pulse is compressed on its leading edge, but the FWHM equals that of the pump. The model predicts more compression than is observed in this case.

In Fig. 3.3(b) the pump and predicted Stokes intensities are plotted versus time for the pulse with $I=8I_{th}$. The peak reflectivity is 0.48, and the predicted Stokes pulse has FWHM=4.15 ns for a compression of 0.78. The actual Stokes pulse was compressed more (0.62). Finally, in Fig. 3.3(c) the intensities for the pulse having $I=4I_{th}$ are plotted. The model gives a compression of 0.62, while the actual compression was 0.42.

The predicted and actual values of pulse compression are plotted in Fig. 3.4. The simple model is in qualitative agreement with the data, but it generally predicts less compression than is observed.

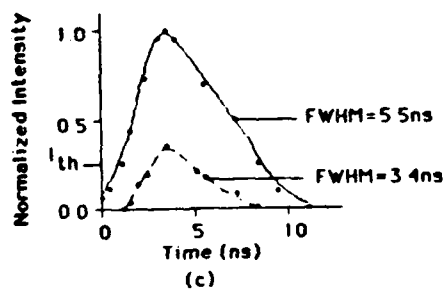
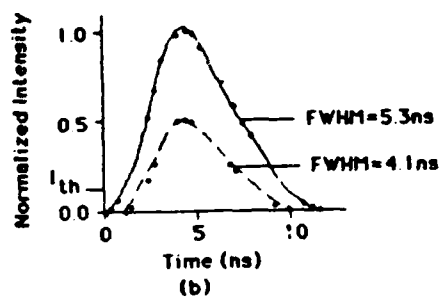
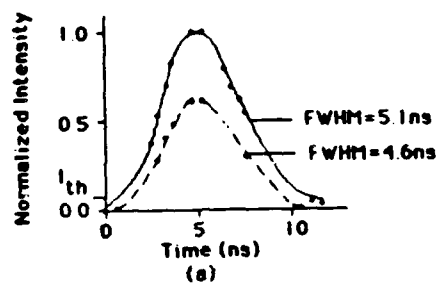


Figure 3.3 The normalized pump and predicted Stokes pulses are plotted versus time. The predicted compression is (a)--0.92, (b)--0.78, (c)--0.62.

Perhaps phonon buildup time effects, which were neglected here, would lead to additional compression because they would delay the onset of SBS. However, these effects would be much more difficult to model. They were neglected because the phonon lifetime (180 ps for hexane pumped at 355 nm)⁵⁶ is much shorter than the pulsewidth.

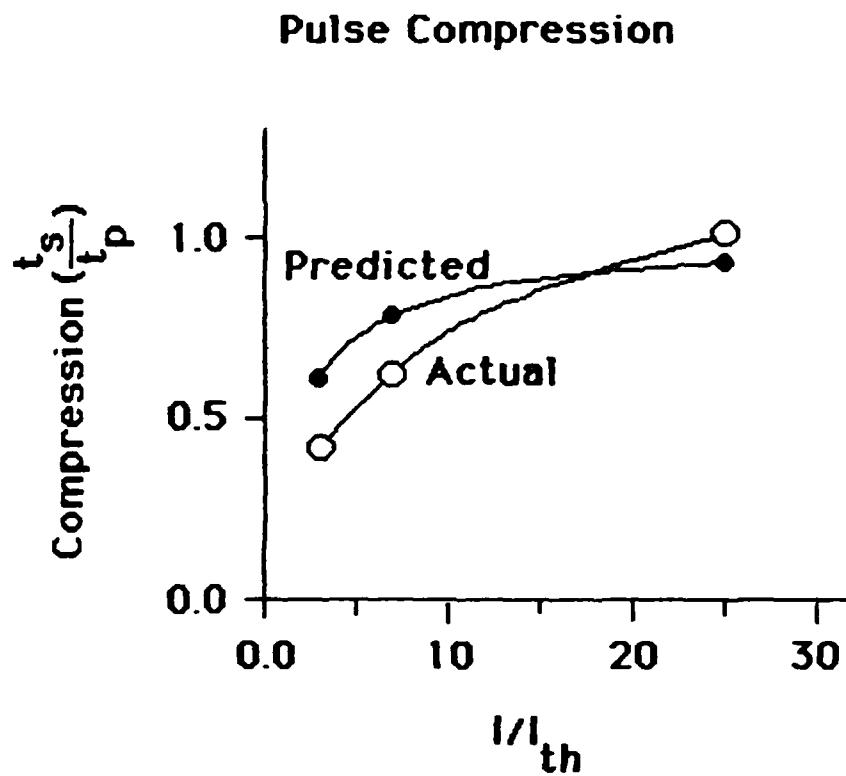


Figure 3.4 The predicted and actual values of the pulse compression are plotted versus the peak pump intensity over the SBS threshold intensity.

3.B.3. Mode Beating Effects

Mode beating is commonly observed in multimode laser operation.⁸⁷⁻⁹¹ Depending on the number of modes running, the temporal structure of a pulse may give sinusoidal or more complicated beating. Several distinct temporal pulse shapes were caused by mode beating in these experiments. The temporal pulse profiles were Fourier analyzed to determine their frequency structure. For up to 5 modes running, the Stokes pulse replicates the pump with two exceptions:

- a) The Stokes pulse is compressed in time, and exhibits a wider bandwidth than the pump under single mode operation.
- b) If the mode beating of the pump leads to strong, short-duration intensity fluctuations at certain times in the pulse, the Stokes pulse has lower gain at similar times in its pulse. This may be due to the onset of competing processes.

Pulse compression for the single mode case was discussed in section 3.B.2. In Fig. 3.5, the pump (left) and Stokes (right) pulses are plotted in time and in frequency spectrum. The pulse compression is obvious and the Stokes spectrum is noticeably broader. The Fourier transform of a narrowed temporal pulse is a broadened

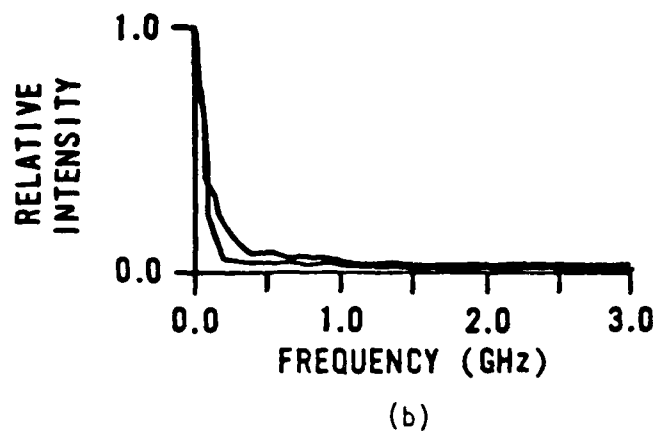
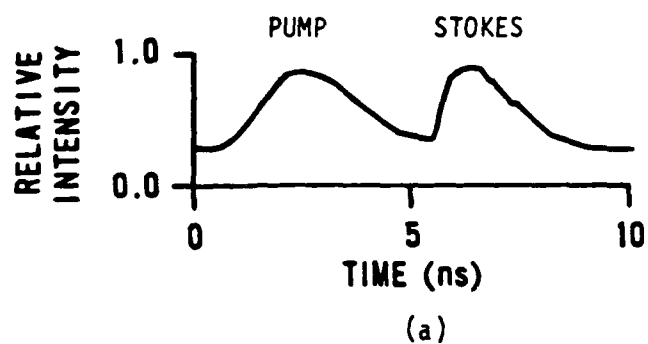


Figure 3.5 The pump and Stokes pulse relative intensities are plotted versus time and frequency. Temporal narrowing of the Stokes pulse leads to spectral broadening.

spectral profile. Nearly single mode operation is confirmed in the pump and Stokes pulses, since there is little power at the beat frequencies.

The case of just two modes beating is presented in Figs. 3.6 and 3.7. In Fig. 3.6, the beat frequency is 650 MHz, or about 3 times the cavity mode spacing. For the shot corresponding to Fig. 3.7, the beat frequency is 450 MHz, or about twice the cavity mode spacing. Apparently the laser can run on two modes which are not adjacent cavity modes. The shot in Fig. 3.6 skipped two modes, while the shot in Fig. 3.7 skipped one mode.

When two adjacent modes ran, it was generally in the context of a total of 3 or more modes running. In Fig. 3.8, the predominant beat is at the cavity frequency (≈ 214 MHz) but there is additional higher frequency modulation.

Even for rather complicated temporal profiles, the Stokes pulse has nearly the same temporal and spectral structure as the pump pulse (see Fig. 3.9). This is in agreement with reflectivity and Fabry-Perot interferometry data reported in Refs. 58 and 59. Note that in Figs. 3.5 - 3.9, the Stokes pulse appears to have a higher intensity than the pump pulse. This is an artifact of the detector scheme. A larger fraction of the Stokes pulse entered the detector than of the pump pulse, so that both pulses would have approximately the same apparent intensity at the detector.

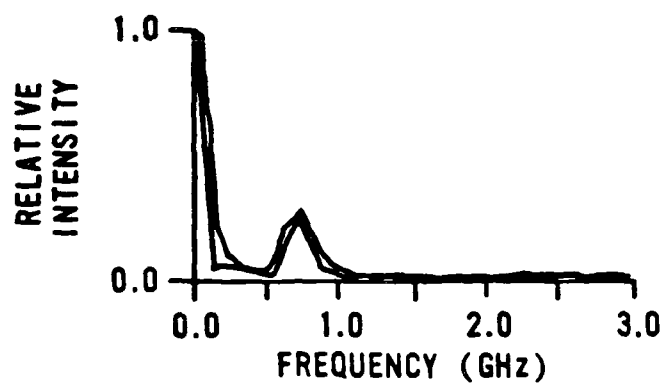
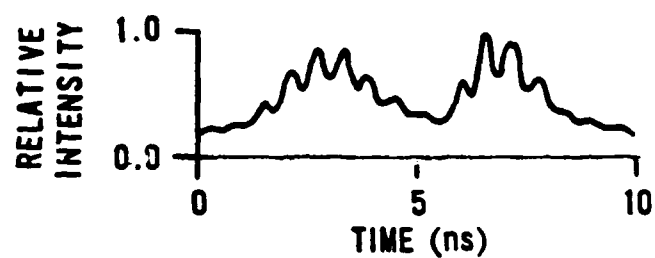


Figure 3.6 Temporal and spectral structure of the pump and Stokes pulses for two modes beating. The modes are separated by 3 times the cavity mode spacing.

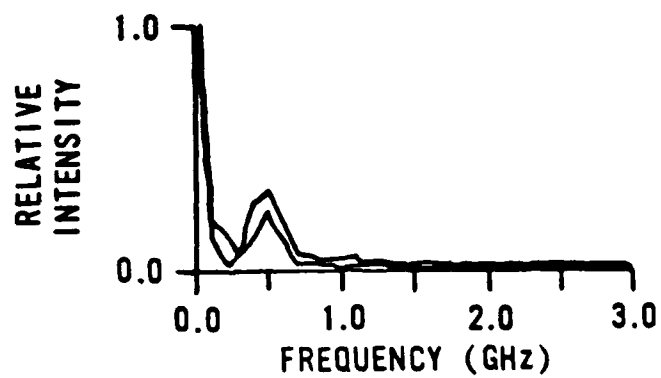
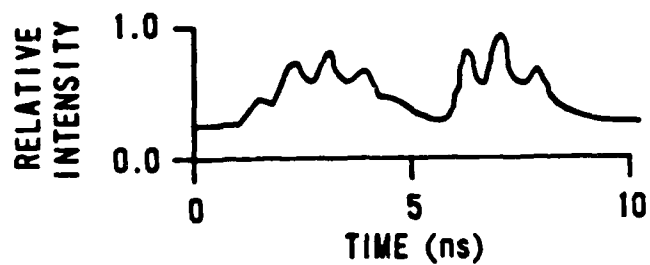


Figure 3.7 Temporal and spectral structure of the pump and Stokes pulses. Modes separated by twice the cavity mode spacing.

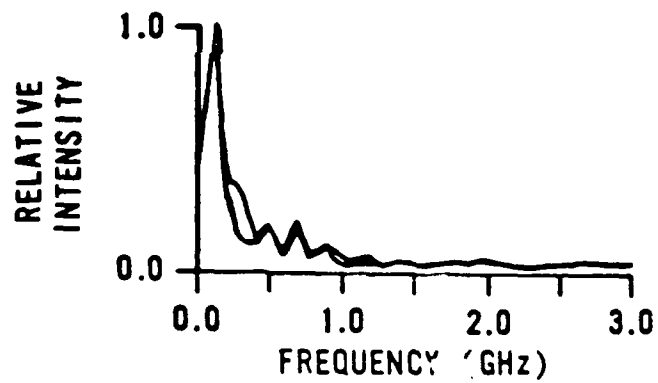
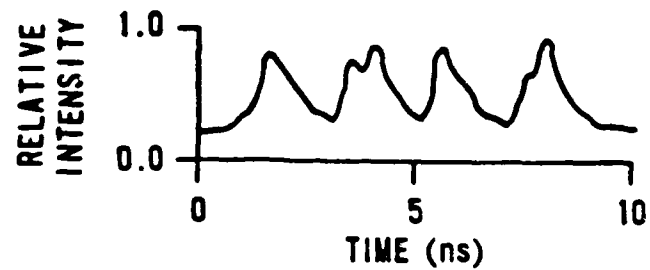


Figure 3.8 Temporal and spectral structure of the pump and Stokes pulses for adjacent modes beating. The predominant beat is at the cavity mode spacing, but there is other beating as well.

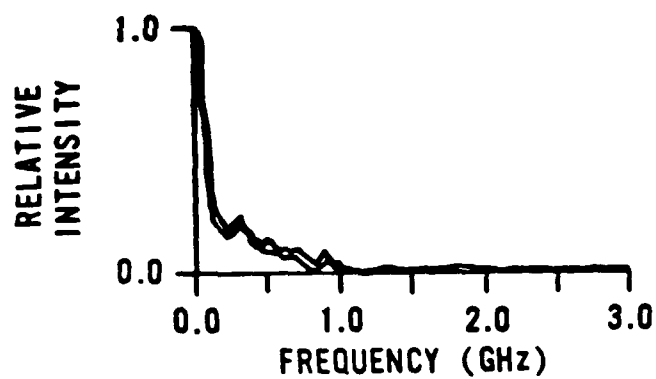
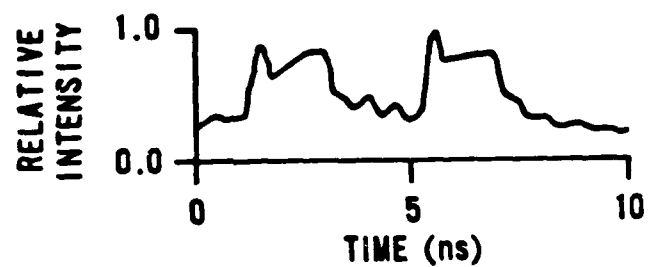


Figure 3.9 Multimode temporal and frequency structure. The Stokes pulse replicates the pump pulse.

For certain pulses, the Stokes pulse did not replicate the pump pulse temporally or in frequency. In Fig. 3.10 we see that the places in the Stokes pulse which differ from the pump pulse occur during the brightest mode beating spikes. These spikes are approximately 400 ps in duration. On the other hand, the Stokes replicates the pump for the rest of the pulse. This is particularly obvious in the upper temporal profile in Fig. 3.10.

Although reduced SBS reflectivity due to mode beating has been reported,^{58,59} to our knowledge this is the first direct observation of partial pulse replication during mode beating.⁹⁷ A possible explanation of this effect is that stimulated Raman scattering (SRS) depletes gain from SBS in these spikes.^{56,58,59} In hexane pumped at 355 nm, the steady state gain for SRS is lower than that for SBS by a factor of approximately 2.45 (see Refs. 56 and 62). The SRS lifetime is on the order of picoseconds, so it reaches steady state during the 400 ps mode beating intensity spikes. The SBS lifetime is 180 ps, and the SBS gain is depleted during the 400 ps mode beating spikes. We often observed forward and backward SRS during highly modulated pump pulses. Second Stokes SRS shifted the wavelength of the light from the UV to the visible, so it was easy to see when SRS occurred. It seems likely that stimulated Raman scattering depleted gain from SBS during the most intense, fastest mode beating spikes.

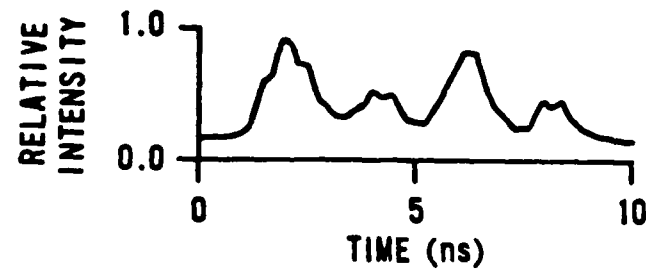
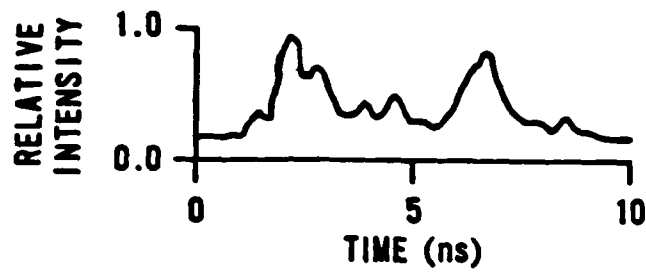
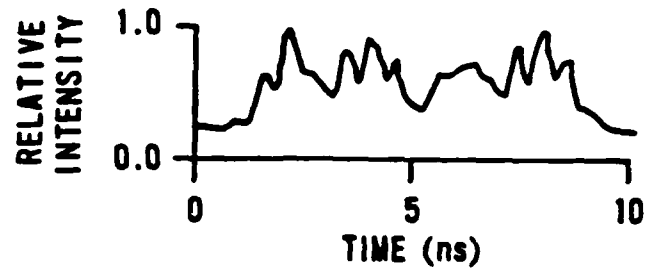


Figure 3.10 Gain depletion in the Stokes pulse during fast, intense mode beating.

3.C. SBS Reflectivity

The SBS reflectivity was measured as a function of the focal intensity for a wide range of laser power settings and aberration strengths. The reflectivity was defined to be the peak intensity of the backscattered pulse divided by the peak intensity of the pump pulse. This quantity depended only on the focal intensity of the brightest aberrated spot.

The unaberrated and aberrated relative intensities were directly measured, and were combined with the pulse energy and temporal data to determine the focal intensity at each laser power and aberrator setting. The reflectivity was measured versus the focal intensity for unaberrated and aberrated pulses at various laser power settings. In Fig. 3.11(a), the reflectivity versus the intensity over the SBS threshold intensity is plotted for unaberrated pulses. The reflectivity exhibits a marked threshold, a monotonic increase, and a reduced slope as saturation became important. The maximum observed reflectivity was 75% at a maximum pump intensity of 55 ± 2 times the SBS threshold intensity. This is in good agreement with published reflectivity curves.³⁸⁻⁴⁴

The threshold intensity was precisely determined by directing the backscattered light into a video camera. At threshold, backscattered light was observed, but just below threshold no backscattered light was detected. This technique had submicrojoule responsivity. The SBS threshold occurred at a focused intensity of 22.5 ± 4.5 GW/cm².

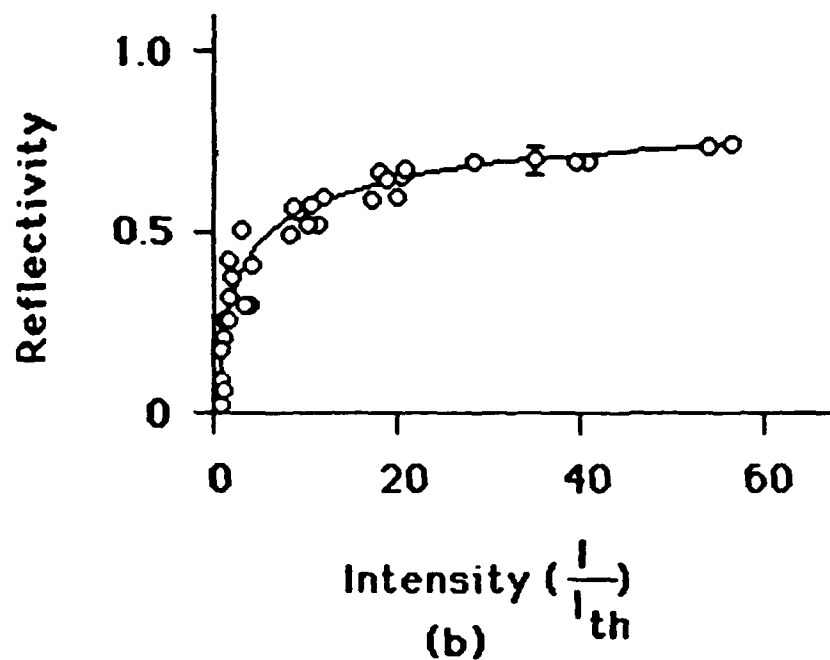
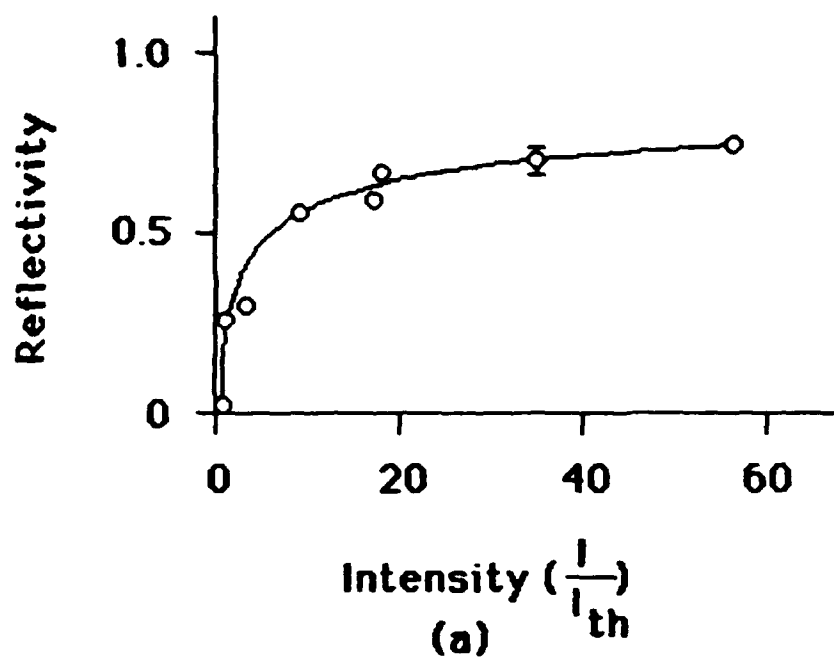


Figure 3.11 The SBS reflectivity is plotted as a function of the focal intensity divided by the threshold intensity. The intensity was changed by changing the laser power in (a), and by aberrating the beam in (b).

It is well known and accepted, both theoretically and experimentally, that the product of the gain coefficient times the pump beam's focal intensity times the gain length (gIl) controls focused SBS reflectivity.^{13,17,21,37-44,56-59} For a diffraction limited pump beam, the threshold value of gIl is easy to calculate from experimental parameters. The gain coefficient g equals 0.026 cm/MW (see Ref. 56). The peak focal intensity is the peak power divided by the focal spot area, times a factor of 3. The factor of 3 is the ratio of the on-axis focal intensity to the average focal intensity for a Gaussian beam. If we let the interaction length be equal to a diffraction limited Rayleigh range, we have

$$gIl = g \frac{3P}{A \lambda} = g \frac{3P}{\lambda} \quad (3.C.1)$$

where P is the peak power (Energy/FWHM for a gaussian temporal profile pulse), and A is the area of the focused spot. The pump energy at the SBS threshold was 0.045 ± 0.005 millijoules, and the pulsewidth was 5.7 ± 0.3 ns, for a power of 7.9 ± 0.9 kilowatts. For $\lambda = 355$ nm, we have $gIl = 17 \pm 2$ at threshold.

Now, if the gain coefficient and intensity are kept at their measured values, while allowing the interaction (gain) length l to be a free parameter, then the commonly accepted assertion that $gIl = 25$ to 30 at threshold^{13-25,35-41} can be used to determine l . This makes the gain length equal to the following:

$$\text{if } gIl=25, \quad l = \frac{25}{17} \frac{\Delta}{\lambda} = 1.5 \frac{\Delta}{\lambda} \quad (3.C.2a)$$

$$\text{if } gIl=30, \quad l = \frac{30}{17} \frac{\Delta}{\lambda} = 1.7 \frac{\Delta}{\lambda} \quad (3.C.2b)$$

So the gain length is 1.5 to 1.7 times the diffraction limited Rayleigh range.

Next, the beam was aberrated by various amounts at each laser power setting. The reflectivity (and hence the gIl product) depended strictly on the focal intensity (see Fig. 3.11(b)--the curve is the same as for Fig. 3.11(a)). The data points for the reflectivity versus the aberrated focal intensity are in full agreement with the data for the reflectivity versus the unaberrated focal intensity. Thus, whether the beam was aberrated or the laser power was changed, the focal intensity controlled the reflectivity.

Recall that the intensity of the brightest aberrated spot was used in these calculations (not the average intensity of the spots). The data show that the intensity of the brightest spot controls the SBS reflectivity. Others have reported similar results.^{79,80}

Regardless of the amount of the beam's aberration, the reflectivity is controlled by the focal intensity. In Fig. 3.12, the reflectivity is plotted as a function of the aberration strength for a constant focal intensity of approximately 10 times the SBS threshold. We see that the reflectivity is independent of the aberration strength. This implies that for all amounts of

aberration, the gain product (gIl) depends only on the focal intensity. Thus l , the gain length, is constant for all amounts of aberration. This is an important and unexpected result.

A primary assumption of the common theoretical formalism for focused SBS is that the gain length is equal to the length of the focal constriction^{13,21,37-40}. We and others²¹ have found that the length of the focal constriction (the distance along the propagation direction for the aberrated beam envelope to increase in size by $\sqrt{2}$) increases roughly linearly as the aberration strength increases. If the gain length did increase with increasing aberration strength, the reflectivity of an aberrated beam at a given focal intensity would exceed the reflectivity of an unaberrated beam at the same focal intensity. However, the reflectivity for unaberrated beams at a given focal intensity is the same as the reflectivity of aberrated beams at the same focal intensity (see Fig. 3.12). Therefore, the gain length is the same for an aberrated beam as for an unaberrated beam. It is not equal to the length of focal constriction, but is independent of the aberration strength and equal to approximately 1.5-1.7 times the diffraction limited Rayleigh range.

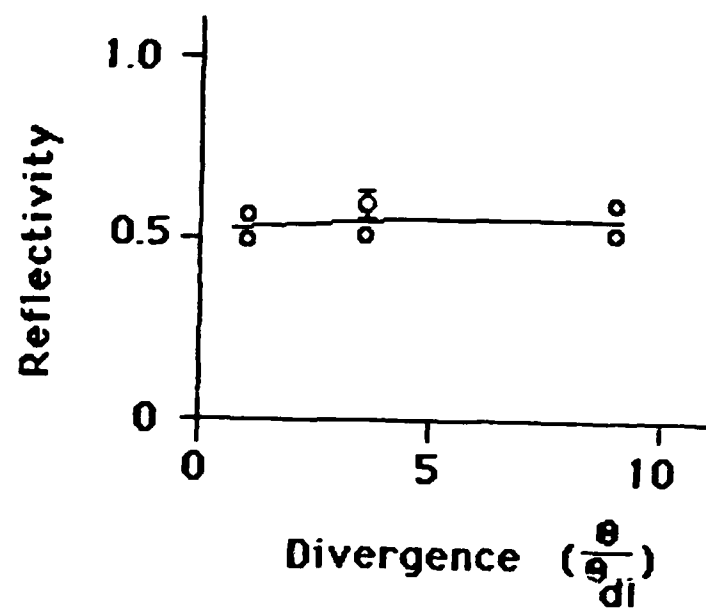


Figure 3.12 The reflectivity is plotted as a function of the aberration strength, for beams with focal intensities approximately equal to 16 times the SBS threshold.

3.D. Characteristics of the Focused Speckle Field: Speckle-Free Stimulated Brillouin Scattering

The longitudinal length of the interference maxima (the speckle length), the transverse speckle structure, and the amount of speckle crossing and twisting were measured by moving the camera along the focal region. These parameters were measured for beams distorted by the variable hot wire array aberrator (see section 2.H) and for beams distorted by etched glass phase plate aberrators. The phase plates were made by etching microscope slides in concentrated hydrofluoric acid for 10 to 120 seconds. They introduced strong aberrations into the beam (the measured increase in the far field divergence, $\xi = \theta/\theta_{d1}$, was 10^2 to 10^3). The variable aberrator produced $1 \leq \xi \leq 24$.

The length of the speckles was nearly constant, regardless of the aberration strength for $1 < \xi < 1000$. Fig. 3.13(a) is a plot of the measured values of speckle length versus the aberration strength, using the hot wire array aberrator, with $1 < \xi < 11$. The speckle length is 2.0 ± 0.8 times the diffraction limited Rayleigh range. For randomly etched phase plate aberrators having $100 \leq \xi \leq 1000$, the speckle length was 2.6 ± 0.9 times the diffraction limited Rayleigh range (see Fig. 3.13(b)). Recall that the gain length was approximately 1.5 - 1.7 times the diffraction limited Rayleigh range. This is approximately 0.8 times the measured values of the speckle length, for all aberration conditions. This leads to the conclusion that the gain occurs in a single speckle length in focused SBS. Note that the

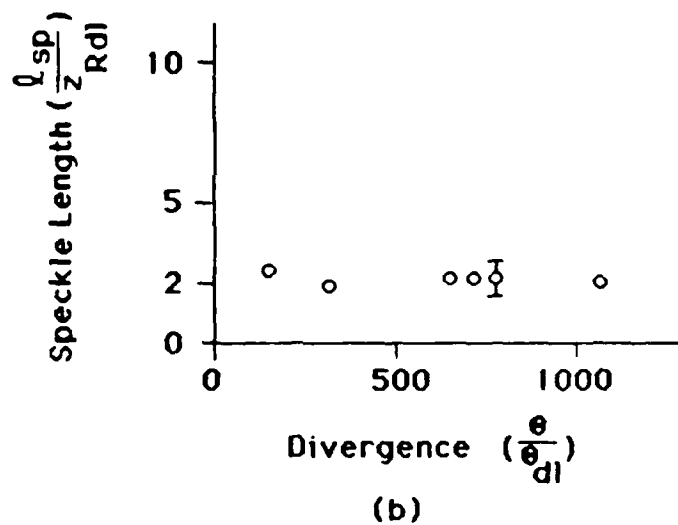
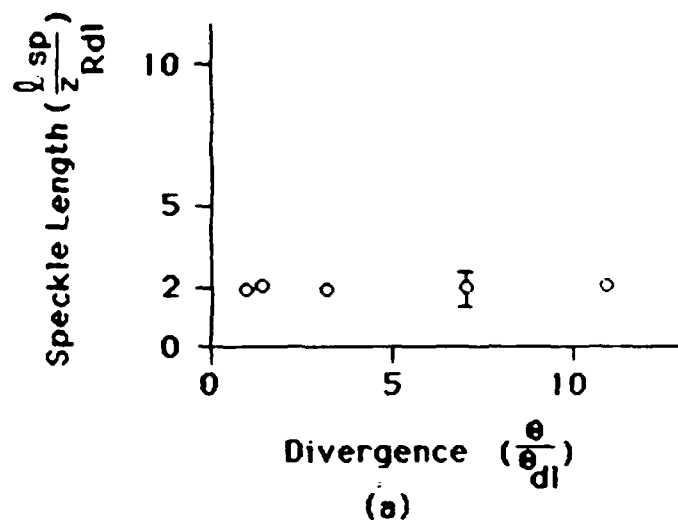


Figure 3.13 The measured speckle length is plotted as a function of the divergence. In (a), the hot wire array aberrator produced $1 < \xi < 11$. In (b), a series of etched glass phase plates produced $100 < \xi < 1000$. z_{Rdl} is the diffraction limited Rayleigh range.

intensity decreases near the ends of each speckle, so that the gain length should be slightly less than the speckle length. It seems reasonable to assume that the gain would cut off as the intensity dropped to zero at the end of a speckle.

A primary assumption of the common theoretical formalism for focused SBS is that the gain length l greatly exceeds the speckle length l_{sp} .^{13,17,21,37-40} In fact, it is argued that $gll_{sp} \ll 1$ is a necessary condition for accurate phase conjugation in focused SBS.^{13,21,38-40} However our data show that $l \approx l_{sp}$, and $gll_{sp} \approx 25$ to 30, regardless of the aberration strength. This is such a novel result, and so directly in conflict with the published theory (that the existence of many speckles along the gain length is a necessary condition for accurate phase conjugation in focused SBS), that we choose to emphasize the novelty by calling it "speckle-free stimulated Brillouin scattering." In contrast to the published theory, the gain length is not much longer than the speckle length; rather, it is slightly shorter than the length of the speckles. A large number of interference maxima along the gain length is not a necessary condition for accurate phase conjugation in focused SBS.

Direct examination of the transverse position of the speckles throughout the interaction length with the far field image analysis system, showed that the speckles do not cross or twist appreciably within the gain length. Even for random phase plates with $\xi > 500$, the angle between of the speckles and the beam axis is on the order of

$$\theta_{sp} \approx (0.5 \text{ to } 2) \frac{w_{sp}}{l_{sp}} \quad (3.D.1)$$

where θ_{sp} is the speckle inclination angle, w_{sp} is the individual speckle radius, and l_{sp} is the speckle length. In other words, even for highly aberrated beams, the speckle crossing angle does not appreciably exceed the diffraction limited divergence θ_{dl} , since $\theta_{dl} \approx w_{dl}/z_{Rdl} \approx 2w_{sp}/l_{sp}$, where w_{dl} is the diffraction limited spot size and z_{Rdl} is the diffraction limited Rayleigh range.

The variable aberrator produced far field intensity distributions which resembled the eigenmodes of a resonator. Fig. 3.14 shows photographs of some of the modes of a stable resonator.⁹¹ Fig. 3.15 shows photographs of the far field intensity distributions produced by the variable aberrator. Note the qualitative agreement of the aberrated far field intensity distributions with the Gauss-Hermite modes listed below each photo. Changing the voltage in the nichrome wires of the aberrator changed the depth of the wavefront modulation, thus producing discrete far field spots. It was possible to "dial in" higher equivalent mode indices by increasing the voltage.

In the case of resonator modes, the overall beam size is nearly constant, regardless of the mode index. The individual spots get smaller as the mode index increases. However, our aberrator produces far field intensity patterns having individual spots which are constant in size w_s , but having an overall size w which increases as the aberration strength increases. In fact, $w = \xi w_{dl}$ where ξ is the increase in the far field divergence, and w_{dl} is the diffraction

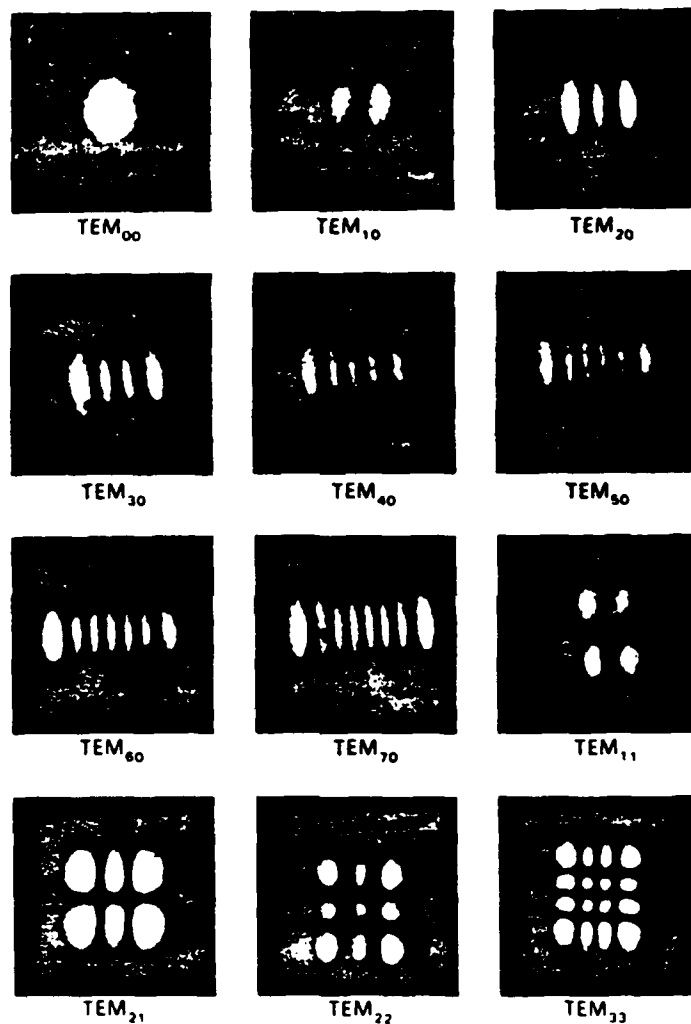


Figure 3.14 Photographs of the Gauss-Hermite modes of a laser resonator (after Ref. 91).

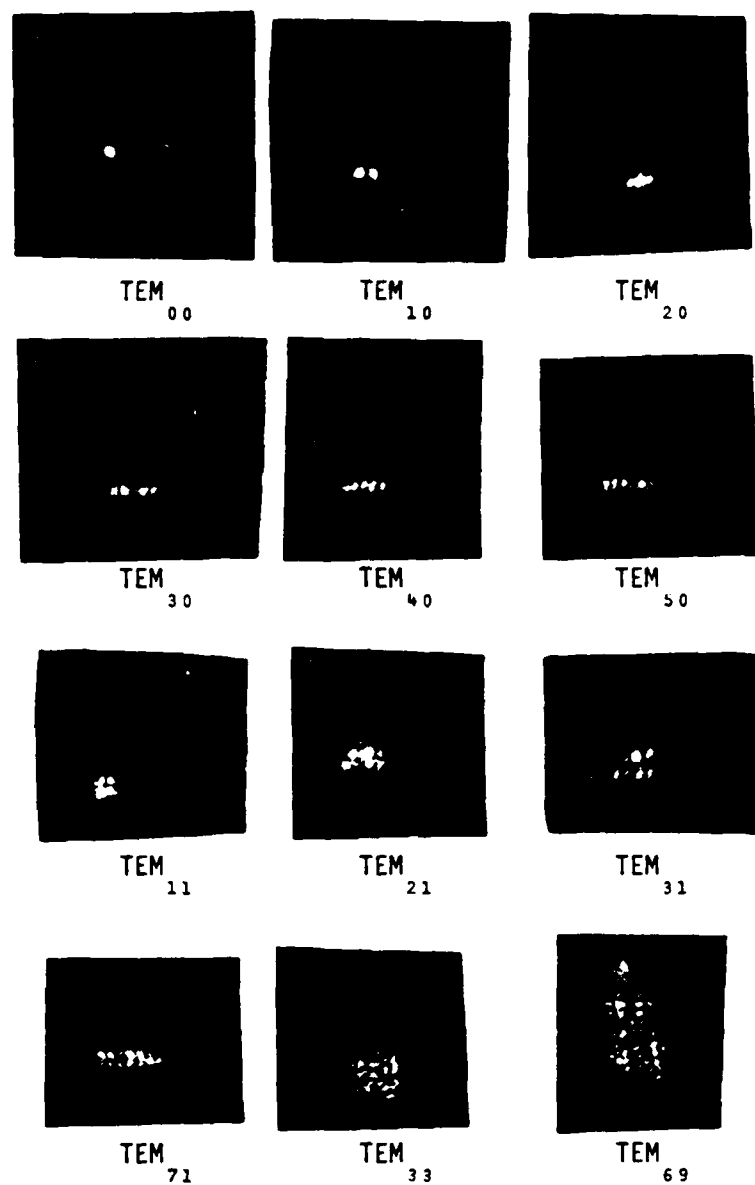


Figure 3.15 Photographs of the far field intensity patterns produced by the variable aberrator. Note the resemblance to the modes listed below each photograph.

limited spot size. It appears that ξ is roughly equal to $n+1$, where n is the equivalent mode index. For example, the pattern emulating the TEM_{33} mode has an overall spot size $\xi=n+1=4$ times larger than the diffraction limited spot size. Note that ξ equals the number of spots in each transverse axis, and n is the number of nulls in each axis.

To summarize this section, the speckle length is independent of the aberration strength, and is approximately equal to twice the diffraction limited Rayleigh range. The gain length is also independent of the aberration strength, and is approximately 0.8 times the speckle length. Because the gain length is less than the speckle length, in contrast to current theories assuming that there must be many maxima and minima in the gain length, we have chosen to call this "speckle-free stimulated Brillouin scattering." The speckles do not cross or twist appreciably within an interaction length, so the equations for SBS growth should be simplified. Finally, we note that using a variable phase grating aberrator, the focused pump intensity distribution qualitatively resembles a single Gauss-Hermite mode, with mode index equal to $\xi-1$, where ξ is the increase in divergence over the diffraction limited divergence.

3.E. Phase Conjugate Fidelity

3.E.0. Overview

We have found that the primary influence on the phase conjugate fidelity in focused SBS is the focal intensity of the pump. Specifically, the intensity of the brightest aberrated spot controls both the SBS reflectivity and the fidelity. For intensities above 5 times the SBS threshold, the phase conjugate fidelity, as measured by the energy in the bucket, is constant and equal to 0.85 ± 0.07 . As the focal intensity declines and approaches the SBS threshold, the phase conjugate fidelity declines. To first order, the effect of aberrating the pump is limited to its effect on the pump's focal intensity. As long as the aberration does not reduce the focal intensity of the brightest spot to within a few times the SBS threshold intensity, the phase conjugation is accurate and independent of the aberration strength.

3.E.1. Aberration Strength Effects: Phase Reconstruction

Shearing interferometry showed that the accuracy of phase reconstruction was independent of the aberration strength. Starting with an unaberrated intensity of approximately 20 times threshold, the pump beam was aberrated in either or both transverse axes. The phase reconstruction was exact, to within the measurement uncertainty, for up to 1.35 waves (peak to valley) of aberration, for a double pass through the aberrator.

To find the accumulated phase introduced into an unconjugated beam after two passes through the aberrator, the lens and SBS cell were replaced with a dielectric coated mirror ($R > 99\%$ at 355 nm, flat to $\lambda/10$). The wavefront phase was measured by shearing interferometry, after the beam had passed twice through the aberrator. Aberrated Strehl ratios as low as 0.007 were observed. When the lens and SBS cell were returned to the setup, the wavefront reconstruction was accurate to within the measurement uncertainty. The reconstructed Strehl ratios were all 0.92 or better, regardless of the strength of aberration. A Strehl ratio of 1.0 corresponds to a diffraction limited beam.

In Fig. 3.16 the reconstructed Strehl ratios are plotted as a function of the aberration strength (input Strehl ratio). The input Strehl ratio was obtained from the double pass, conventional mirror data. In the plot, the squares are the data for one aberrator at

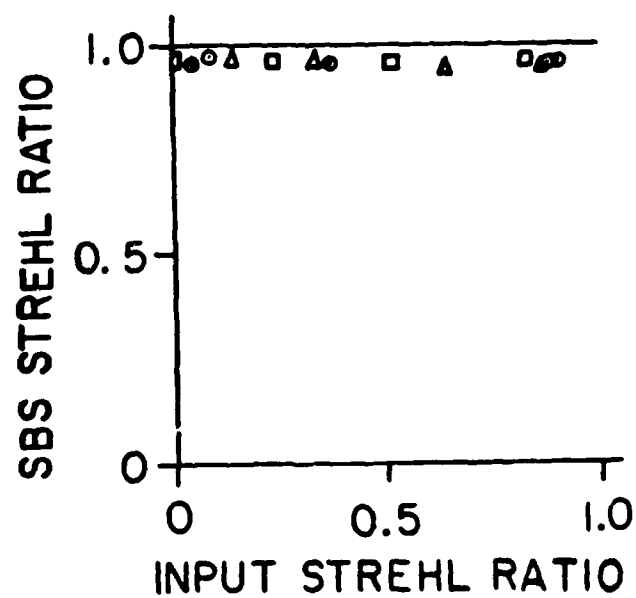


Figure 3.16 The reconstructed Stokes beam's interferometrically measured Strehl ratio is plotted as a function of the aberrated pump's Strehl ratio.

various voltage settings, the triangles represent the data for the other aberrator, and the circles are the data corresponding to equal voltage on both aberrators. The solid horizontal line at 1.0 indicates perfect phase reconstruction. The data shows that the phase reconstruction in focused SBS is accurate, independent of the aberration strength.⁹⁸

3.E.2. Aberration Strength Effects: Energy in the Bucket

The fidelity of phase conjugation was measured using an energy in the bucket technique (see section 2.G. for a description of the technique). Strongly aberrated beams had scintillations (changes in intensity across the beam front), which were not removed by phase conjugation. Scintillations slightly decreased the conjugate beam near field spot size, especially for strongly aberrated beams. The slightly smaller near field spots were less focusable. This decreased the phase conjugate fidelity as measured by the energy in the bucket.

In Fig. 3.17, the phase conjugate fidelity is plotted as a function of the aberration strength, for several pump powers. The fidelity monotonically declines for increasing aberration strength, and the rate of decline is lowest for the most intense beam. The critical strength of aberration, the point where the fidelity drops sharply for a small increase in aberration, increases with increasing pump power. This appears to be consistent with the wide range of reported "maximum" amounts of aberration correctable by focused SBS.^{26,37,38,42-44} Higher pump powers can correct stronger aberrations. This data has important implications for users of SBS phase conjugation. The specific dependence of the fidelity on the focal intensity is discussed in the next section.

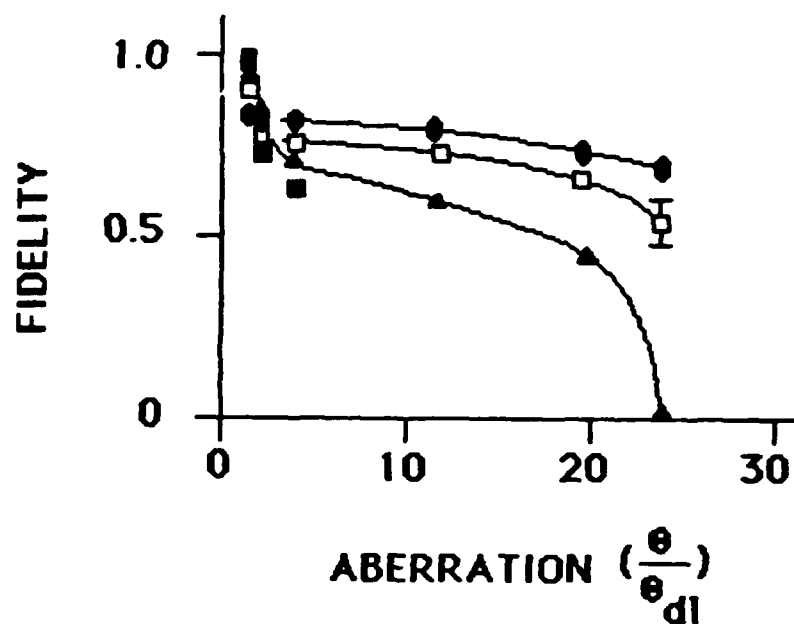


Figure 3.17 The phase conjugate fidelity is plotted versus the aberration strength. Before aberration, \blacksquare -- $I=6I_{th}$, \blacktriangle -- $I=20I_{th}$, \square -- $I=40I_{th}$, \bullet -- $55I_{th}$.

3.E.3. Focal Intensity Effects

The effect of the focal intensity on SBS fidelity has been largely ignored in the published literature. Data on the fidelity versus the pulsewidth, the aberration strength, and the pulse energy have been reported in the literature, but so far there has been no literature on focal intensity effects. For this study, direct measurements of the reduction in the focal intensity of the brightest aberrated spot were made. The data show that the focal intensity is a crucial parameter in the phase conjugate fidelity of focused SBS. The measurement technique was to set the unaberrated laser power at a known amount above the SBS threshold, and then increase the aberration strength, thereby reducing the focal intensity until SBS was no longer observed. Since the reduction in focal intensity for each aberrator setting was known, the focal intensity for each data point in each run was also known.

In Fig. 3.18, the fidelity is plotted as a function of the focal intensity for six data runs. Within each plot, the reduction in the focal intensity is due to progressively increasing the aberration strength. Each point represents the average of 100 shots. Note that the fidelity is largely independent of the focal intensity, hence independent of the aberration strength, as long as the intensity is more than 5 times the SBS threshold intensity. This is particularly apparent in Fig. 3.18(a). The laser power was decreased for the next runs (b)-(f). The "critical strength" of aberration occurs at the point where the focal intensity is reduced to approximately five

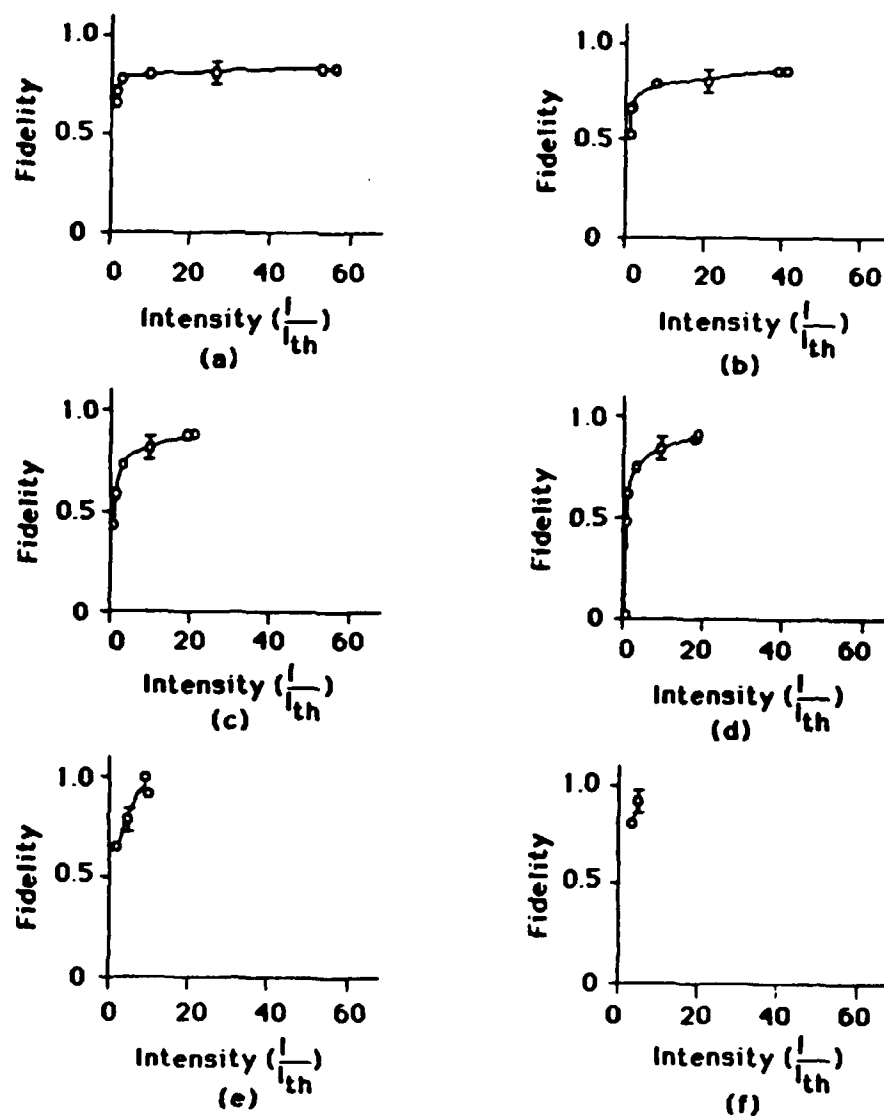


Figure 3.18 The phase conjugate fidelity is plotted versus the aberrated focal intensity. Before aberration,
 (a) $--I=55I_{th}$, (b) $--I=40I_{th}$, (c) $--I=21I_{th}$, (d) $--I=19I_{th}$,
 (e) $--I=10I_{th}$, (f) $--I=5I_{th}$.

times the SBS threshold. In most cases, the fidelity monotonically declines as the aberration strength increases, and as the focal intensity decreases.

A crucial finding of this research is that all the data in Fig. 3.18 can be fit to a single, smooth, physically meaningful curve. In Fig. 3.19 all the data in Figs. 3.18(a)-(f) is plotted. The fit to the curve is quite good: the mean square deviation from the curve is under 4 percent. This data was all taken in a single afternoon, to minimize potential errors due to minor alignment differences. The simple curve is physically significant: the fidelity is constant and near unity (0.85 gives the best fit) as long as the focal intensity is above 5 times threshold. As the focal intensity declines to approach the SBS threshold, the fidelity declines sharply.

Unaberrated and strongly aberrated data points fit the curve equally well. In fact, the curve in Fig. 3.19 was derived from a fit to the unaberrated data. The phase conjugate fidelity versus focal intensity data for all unaberrated shots is shown in Fig. 3.20. There is more spread in unaberrated intensity data than in the aberrated intensity data, probably because it was taken over the course of two weeks. Minor changes in the alignment or other factors could have caused the increased variance. Still, the mean square fit to the curve is better than 6 percent. This data is in qualitative agreement with the data reported in Ref. 42. The fidelity increases with increasing pump power when the pump is aberrated. For high

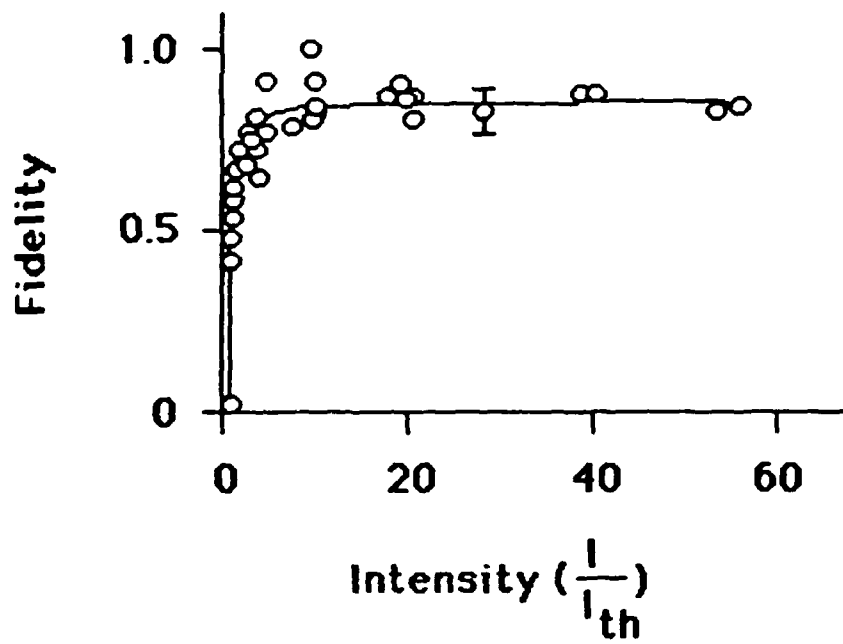


Figure 3.19 All fidelity versus focal intensity data from Fig. 3.18
(a)-(f) are plotted on a single curve.

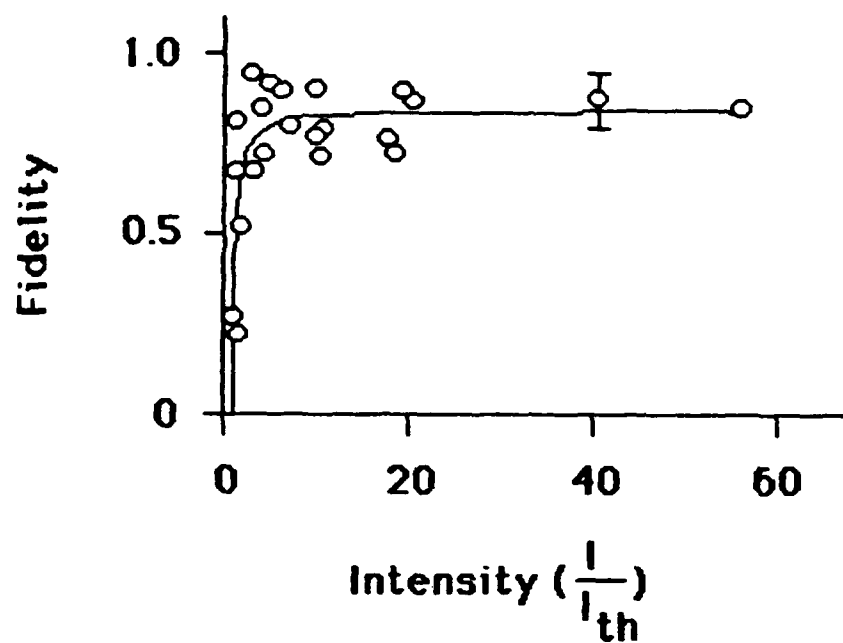


Figure 3.20 All fidelity versus focal intensity data for unaberrated pump pulses is plotted. The curve is the same as in Fig. 3.19.

pump powers, the published data show accurate phase conjugation, independent of the aberration strength. For low pump powers, increasing the aberration strength decreases the phase conjugate fidelity.⁴²

To summarize this section, for both unaberrated and aberrated beams the intensity of the brightest focal spot controls the phase conjugate fidelity. The primary effect of aberration is its reduction in the pump beam's focal intensity. Pulses having focal intensities over 5 times threshold were conjugated accurately, but pulses approaching the SBS threshold intensity underwent inaccurate phase conjugation, regardless of their aberration strength. The maximum correctable aberration for focused SBS is that aberration which reduces the focal intensity to a few times the SBS threshold intensity. To our knowledge, these are the first measurements of the effect of the aberrated focal intensity on the fidelity of focused SBS.⁹⁹

3.E.4. "Second Order Effects"

Experiments have been reported that show slightly declining phase conjugate fidelity for unaberrated beams as the focal intensity increases from a few times the SBS threshold intensity to several hundred times the SBS threshold.^{34,38,41-44} However, this effect is small: typically, a reduction of less than 10% in fidelity is observed for an increase in intensity of more than two orders of magnitude. An examination of the data on the phase conjugate fidelity as a function of the focal intensity for unaberrated beams reveals a similar effect. In Fig. 3.21, the fidelity versus focal intensity data for unaberrated (O) and slightly ($\xi < 1.3$) aberrated (O) beams is presented. In contrast to the data presented in Fig. 3.20, which was taken over a two week period, this data was taken in a single afternoon. The line is a linear least squares fit to the data, indicating a 7.8% reduction in the fidelity for an increase of nearly two orders of magnitude in the unaberrated focal intensity.

No conclusive, quantitative theory has been developed to account for this effect, but a plausible explanation argues that the point where intensity exceeds threshold, hence the point where SBS occurs, is upstream of the focal constriction when the intensity is well above threshold. This means that SBS starts and phase conjugation occurs at other than the far field point, and not all phase interruptions are converted into intensity effects. The pump beam phase does not enter into the Stokes gain equation; only the pump intensity is present. Phase conjugation is accurate if the

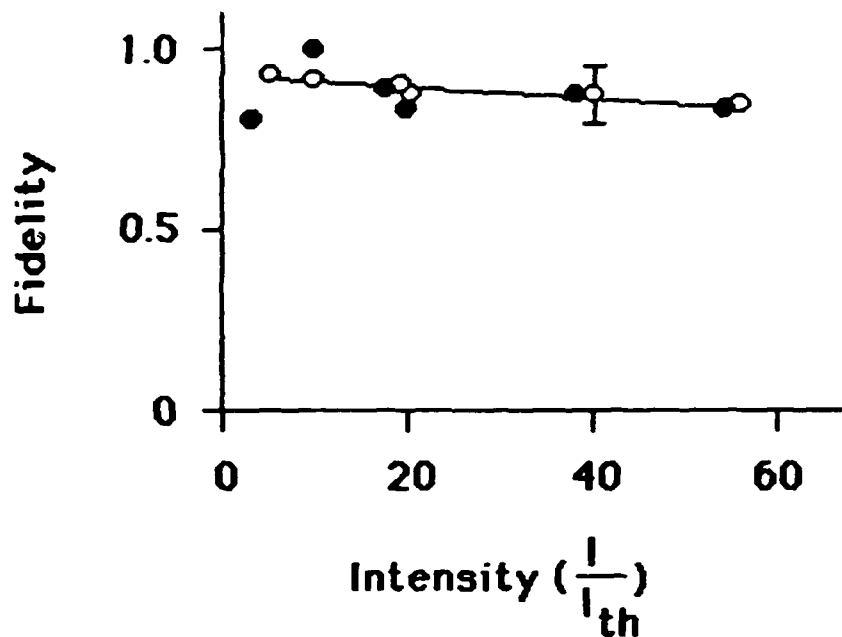


Figure 3.21 The slight decrease in fidelity for increasing focal intensity is plotted for unaberrated--0 and slightly ($\xi \approx 1.3$) aberrated--0 beams. The line is a linear least squares fit to the data.

phase fluctuations are converted to intensity fluctuations (as happens at the far field point), but may be inaccurate if there are many unconverted phase fluctuations (as would happen upstream of the focus). It would be difficult to quantify such effects, at least analytically. Perhaps a computer code could be developed in the future to take such effects into account.

Another second order effect is a slight reduction in the fidelity as the aberration strength is increased, for a fixed focal intensity. In Fig. 3.22, the fidelity is plotted as a function of the aberration strength, for a fixed focal intensity of ten times the SBS threshold. A 10% reduction in the fidelity is observed for an order of magnitude increase in the aberration strength.

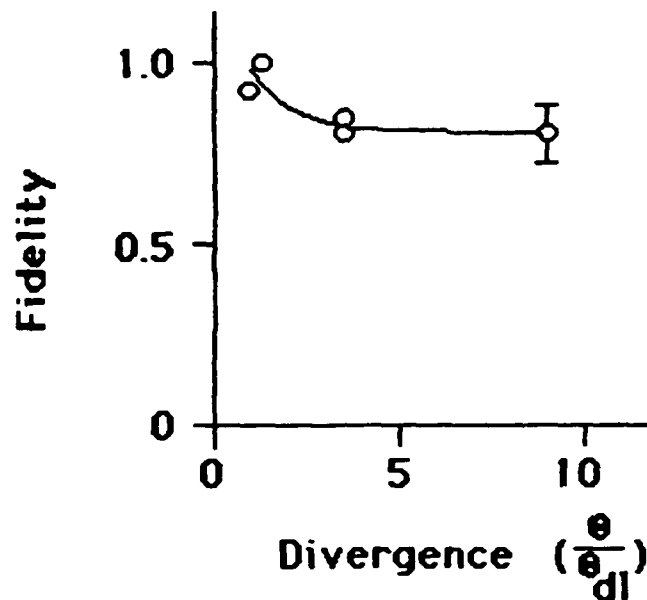


Figure 3.22 The fidelity is plotted as a function of the aberration strength, for constant $(I-10I_{th})$ focal intensity. Stronger aberrations are generally conjugated with slightly less fidelity.

3.E.5. Summary of Phase Conjugate Fidelity Findings

Using interferometrically determined Strehl ratios, for pulses with intensities well above the SBS threshold, the phase reconstruction accuracy was perfect, to within the experimental uncertainty, regardless of the aberration strength. Intensity modulation across the beam diameter was observed on the Stokes beams which were produced by strongly aberrated pump beams. This led to slightly lower values of the phase conjugate fidelity (the overlap of the pump and Stokes fields) than the values of the phase reconstruction accuracy (the pump and Stokes phase equivalence).

Energy in the bucket measurements showed that the aberrated focal intensity controlled the phase conjugate fidelity. The fidelity was high (0.85 ± 0.06) and independent of the intensity unless the intensity was decreased to below 5 times the SBS threshold. As the intensity approached the SBS threshold, the fidelity dropped sharply. This strong dependence of the phase conjugate fidelity on the aberrated focal intensity may help explain the wide range of maximum correctable aberrations which have been reported in the literature. The data indicates that there will be a different maximum aberration for each laser power setting. Higher power pump beams can correct stronger aberrations using focused SBS. To the extent that it is possible to infer aberrated focal intensities from published experimental plots of the phase conjugate fidelity versus the pump energy and aberration strength, this data appears to be in qualitative agreement with published experimental results.

Second order effects were observed. For unaberrated beams, the fidelity dropped approximately 8% for a nearly 2 order of magnitude increase in the focal intensity. This agrees well with published experimental results. Also, the fidelity was consistently lower (but typically by less than 10 percent) for strongly aberrated beams than for unaberrated beams at fixed focal intensities.

Chapter 4. Theory

This chapter is devoted to a development of the theory of focused stimulated Brillouin scattering. The coupled wave equations are derived and solved, first using the plane wave approximation, giving temporal and bandwidth effects, and then using the paraxial and non-depleted pump approximations. A decomposition into Gauss-Hermite modes is used, and the equations are solved analytically for the case of pumping by a single Gauss-Hermite mode. This somewhat artificial case is qualitatively in agreement with the transverse pump intensity caused by a variable phase grating aberrator. The analytic solution is in agreement with experimental observations that the wavefront reversal is accurate, and nearly independent of the strength of aberration, as long as the pump intensity is well above threshold.

4.A. Derivation of the Coupled Gain Equations

The plane wave and paraxial coupled gain equations for pump and Stokes beams in stimulated Brillouin scattering are well known.^{18-25,100,101} The remarks in this section are simply a review of the accepted development, leading to the coupled paraxial equations for the pump and Stokes beams. Stimulated Brillouin scattering is the scattering of a pump field E_L by density- or pressure-driven index of refraction changes in a medium, giving a scattered (Stokes) field E_S . Specifically, the pump field scatters from thermal phonons in the medium, giving a frequency-shifted Stokes field. As the number of Stokes photons increases, stimulated scattering can occur. The pump and Stokes waves interact to produce a quasi-standing wave which moves at the sound speed, instead of the speed of light. In steady state conditions, the Stokes wave travels in a direction opposite to the pump wave. The theory of Stokes wave buildup and its transverse intensity overlap with the pump beam is the subject of this chapter.

If we ignore absorption (the absorption coefficient is less than 0.01 cm^{-1} for hexane at 355 nm) then the wave equations for a pump field E_L and a Stokes field E_S interacting with nonlinear polarizations $P_{NL(L,S)}$ are⁵⁶

$$\nabla^2 E_L - \frac{\epsilon \mu}{c^2} \frac{\partial^2 E_L}{\partial t^2} = - \frac{4\pi}{c^2} \frac{\partial^2 P_{NL(L)}}{\partial t^2} \quad (4.A.1a)$$

and

$$\nabla^2 E_S - \frac{\epsilon \mu}{c^2} \frac{\partial^2 E_S}{\partial t^2} = -\frac{4\pi}{c^2} \frac{\partial^2 P_{NL}(S)}{\partial t^2} \quad (4.A.1b)$$

The first term gives propagation and diffraction; the second gives temporal effects; the right hand side is the source term which includes bandwidth effects. The slowly varying envelope approximation makes the right hand sides equal to $\frac{-4\pi\omega_{L,S}^2}{c^2} P_{NL}(L,S)$.

The nonlinear polarization is caused by pressure-induced index of refraction changes in the medium,⁵⁴ which are, in turn, caused by electrostriction. The nonlinear polarization for the pump wave can be written^{21,56,96}

$$P_{NL}(L) = \frac{-ik\gamma^2}{32\pi^2 cv\rho\Gamma_B} \frac{1}{1 + (\Delta\nu_L)^2/(\Delta\nu_B)^2} |E_S|^2 E_L \quad (4.A.2a)$$

where γ is the coefficient of electrostriction, v is the velocity of sound, ρ is the density, $\Gamma_B = 2\pi\Delta\nu_B$ is the Brillouin linewidth, $\Delta\nu_L$ is the laser linewidth, and $\vec{k} = \vec{k}_L + \vec{k}_S$ is the wavevector of the sound wave ($|\vec{k}| = k \approx k_L - k_S$ for backscattering). Similarly,

$$P_{NL}(S) = \frac{ik\gamma^2}{32\pi^2 cv\rho\Gamma_B} \frac{1}{1 + (\Delta\nu_L)^2/(\Delta\nu_B)^2} |E_L|^2 E_S \quad (4.A.2b)$$

The first term in the right hand side is a gain coefficient, the second term is a Lorentzian bandwidth dependence¹⁰² and the third term is the product of fields driving the electrostriction.

Note that $\Gamma_B = 1/\tau_B$, the phonon lifetime. The phonon lifetime is given by⁵⁶

$$\tau_B = \frac{\rho}{4\eta k_L^2 \sin^2(\phi/2)} \quad (4.A.3)$$

where η is the viscosity, and ϕ is the angle between the pump beam and the Stokes beam. The phonon lifetime becomes extremely long for forward scattering ($\phi=0$). Forward SBS has been predicted for pulses with widths more than several hundred times the backward SBS phonon lifetime.⁸⁸ For our 6 ns pulses, which are 30 times the backward SBS phonon lifetime (180 ps in hexane pumped at 355 nm),⁵⁶ forward SBS was not observed.

In order to simplify the notation in equations (4.A.2), we define

$$\frac{g_L}{2} = \frac{k\gamma^2\omega_L}{16\pi c^2\nu\rho\Gamma_B} \frac{1}{1 + (\Delta\nu_L)^2/(\Delta\nu_B)^2} \quad (4.A.4a)$$

and

$$\frac{g_S}{2} = \frac{k\gamma^2\omega_S}{16\pi c^2\nu\rho\Gamma_B} \frac{1}{1 + (\Delta\nu_L)^2/(\Delta\nu_B)^2} \quad (4.A.4b)$$

Substituting the results of (4.A.4) and (4.A.2) into (4.A.1) to gives

$$\nabla^2 E_L - \frac{\epsilon\mu}{c^2} \frac{\partial^2 E_L}{\partial t^2} = \frac{2ik_L g_L}{2} |E_S|^2 E_L \quad (4.A.5a)$$

and

$$\nabla^2 E_S - \frac{\epsilon\mu}{c^2} \frac{\partial^2 E_S}{\partial t^2} = \frac{-2ik_S g_S}{2} |E_L|^2 E_S \quad (4.A.5b)$$

In the experiments, the 6 ns pulsewidth is 30 times the phonon lifetime, so we can assume a steady state solution (exceptions will be discussed in section 4.C). We also make the paraxial approximation, because the fields do not vary significantly in the transverse direction over distances on the order of a wavelength of light. So equations (4.A.5) become^{16,18-26,38,39}

$$\nabla_T^2 E_L - 2ik_L \frac{\partial E_L}{\partial z} = \frac{2ik_L g_L}{2} |E_S|^2 E_L \quad (4.A.6a)$$

and

$$\nabla_T^2 E_S + 2ik_S \frac{\partial E_S}{\partial z} = \frac{-2ik_S g_S}{2} |E_L|^2 E_S \quad (4.A.6b)$$

where $\nabla_T^2 = \frac{\partial^2}{\partial x^2} + \frac{\partial^2}{\partial y^2}$

These are the coupled, paraxial, steady state equations for stimulated Brillouin scattering. In the following sections we discuss steady state plane wave solutions, transient solutions, and steady state, paraxial, undepleted pump solutions.

4.B. Plane Wave Equations

The solutions to the coupled equations for the pump and Stokes waves with no transverse derivatives are well known. They have been solved for the cases of a non-depleted pump,⁵⁶ a depleted pump with no absorption,¹⁰⁰ and a depleted pump with absorption.¹⁰¹ A few comments are in order for each of the published solutions.

We shall assume a plane pump wave propagating in the +z direction, exciting a plane Stokes wave propagating in the -z direction, in a medium extending from z=0 to z=l (see Fig. 4.1). The time independent equations, taking absorption into account, are

$$\frac{\partial E_L}{\partial z} = -\frac{g_L}{2} E_L E_S E_S^* - \frac{\alpha}{2} E_L \quad (4.B.1a)$$

$$\frac{\partial E_S}{\partial z} = -\frac{g_S}{2} E_S E_L E_L^* + \frac{\alpha}{2} E_S \quad (4.B.1b)$$

Multiplying eq. (4.B.1a) by E_L^* and adding its complex conjugate, and multiplying eq. (4.B.1b) by E_S^* and adding its complex conjugate gives^{56,100,101}

$$\frac{\partial I_L}{\partial z} = -g_L I_L I_S - \alpha I_L \quad (4.B.2a)$$

$$\frac{\partial I_S}{\partial z} = -g_S I_S I_L + \alpha I_S \quad (4.B.2b)$$

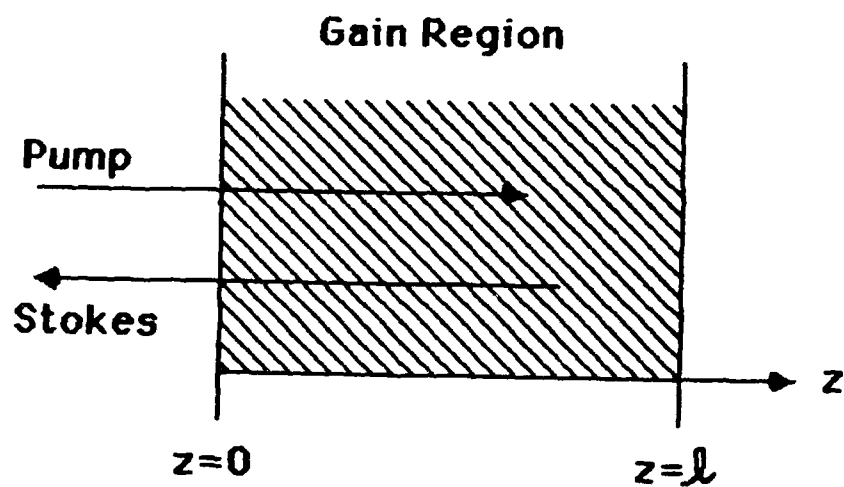


Figure 4.1 Geometry of the plane wave problem. The pump propagates from $z=0$ to $z=l$, but the Stokes propagates from $z=l$ to $z=0$.

If we assume no pump depletion, I_L is a constant and we have

$$\frac{\partial I_S}{\partial z} = -(g_S I_L - \alpha) I_S \quad (4.B.3)$$

This is simply exponential growth in the $-z$ (Stokes propagation) direction with a gain coefficient of $g_S I_L - \alpha$. Noting that $\alpha < 0.01 \text{ cm}^{-1}$ for hexane pumped at 355 nm, we neglect absorption for the rest of the theoretical development. Thus,

$$\frac{I_S(0)}{I_S(l)} = \exp(g_S I_L l) \quad (4.B.4)$$

It is widely agreed^{21-25,36-39} that at threshold the gIl product equals 25 to 30. The large amplification (10^{11} to 10^{13}) is a crucial factor in gain discrimination of conjugate waves from nonconjugate waves. We shall discuss the implications of intensities over threshold, and pump depletion below.

If we now include pump depletion, but neglect absorption, equations (4.B.2) are easily integrated. We start with

$$\frac{\partial I_L}{\partial z} = -g_L I_L I_S \quad (4.B.6a)$$

$$\frac{\partial I_S}{\partial z} = -g_S I_S I_L \quad (4.B.6b)$$

Dividing equation (4.B.6a) by (4.B.6b) gives

$$\frac{\partial I_L}{\partial z} = \frac{g_L}{g_S} \frac{\partial I_S}{\partial z} \quad (4.B.7)$$

so

$$I_L(z) - \frac{g_L}{g_S} I_S(z) = \text{const} = I_L(l) - \frac{g_L}{g_S} I_S(l) \quad (4.B.8)$$

If we let $g_L = g_S$ then $I_L(z) - I_S(z) = I_L(l) - I_S(l)$. The difference in intensities of the pump and Stokes waves is a constant throughout the gain region. Since $g_L/g_S = \omega_L^2/\omega_S^2$ we can think of (4.B.8) as being a Manley-Rowe relation,^{100,103} or as conservation of energy.⁹⁷ The decrease in the pump photon flux in the +z direction equals the increase in the Stokes photon flux in the -z direction.

Substituting (4.B.8) into equation (4.B.6b) we get

$$\frac{\partial I_S}{\partial z} = -g_S I_S (I_S + C) \quad (4.B.9)$$

$$\text{where } C = I_L - I_S$$

The solution is^{100,104}

$$\frac{I_S(z)}{I_S(0)} = \frac{1 - I_S(0)/I_L(0)}{\exp[(1 - I_S(0)/I_L(0))g_S I_L(0)z] - I_S(0)/I_L(0)} \quad (4.B.10)$$

Unfortunately, $I_S(0)$ is unknown. We can derive a transcendental equation for $I_S(0)$, based on our knowledge of the noise Stokes intensity $I_S(l)$ and the input pump intensity $I_L(0)$. At $z=l$, equation (4.B.10) becomes

$$\frac{I_S(0)}{I_S(l)} = \frac{\exp[(1-I_S(0)/I_L(0))g_S I_L(0)l] - I_S(0)/I_L(0)}{1 - I_S(0)/I_L(0)} \quad (4.B.11)$$

and if we know the noise Stokes intensity $I_S(l)$ then equation (4.B.11) is a transcendental equation in one unknown, which can be solved on a computer.

If we define the reflectivity R to be $I_S(0)/I_L(0)$, then equation (4.B.11) is simplified.

$$\frac{I_S(0)}{I_S(l)} = \frac{\exp[(1-R)g_S I_L(0)l] - R}{1-R} \quad (4.B.12)$$

Now, let us return to the z -dependent plane wave equations. Letting $R=I_S(0)/I_L(0)$, eq. (4.B.10) becomes

$$\frac{I_S(z)}{I_S(0)} = \frac{1-R}{\exp[(1-R)g_S I_L(0)z] - R} \quad (4.B.13)$$

We can plot equation (4.B.13) for various SBS reflectivities. At $R=0.01$, the plot of $I_S(z)$ agrees with simple exponential growth (in the $-z$ direction) to better than 0.1 percent. If we assume 100% reflectivity (nearly 100% reflectivity has been observed with SBS in

heptane pumped at 308 nm^{48}), the form of the differential equation (4.B.9) is simplified. In this case, $C=0$ and we have

$$\frac{\partial I_S}{\partial z} = -g_S I_S^2 \quad (4.B.14)$$

The solution is

$$I_S(z) = \frac{1}{g I_S(0)z + 1} = \frac{1}{g I_L(0)z + 1} \quad (4.B.15)$$

since $I_S(0)=I_L(0)$.

For $R=99\%$, the solution in equation (4.B.13) agrees with the 100% reflectivity simple form (4.B.15) to better than 5 percent. So, equation (4.B.13) matches the z -dependence of the simple solutions for conditions of low and high reflectivity. In all cases, over half of the total gain occurs in the first 10 percent of the gain length. In Fig. 4.2, we plot the z -dependent intensity, calculated from (4.B.13), for several values of the reflectivity. The intensity of the pump monotonically declines in the $+z$ direction, and the intensity of the Stokes beam is different from the pump beam by a constant throughout the gain region. The Stokes beam increases in intensity in its propagation direction ($-z$).

In summary, the solutions for plane wave SBS show exponential growth for no depletion, hyperbolic growth for full (100%) depletion, and more complicated (but monotonic) growth for intermediate

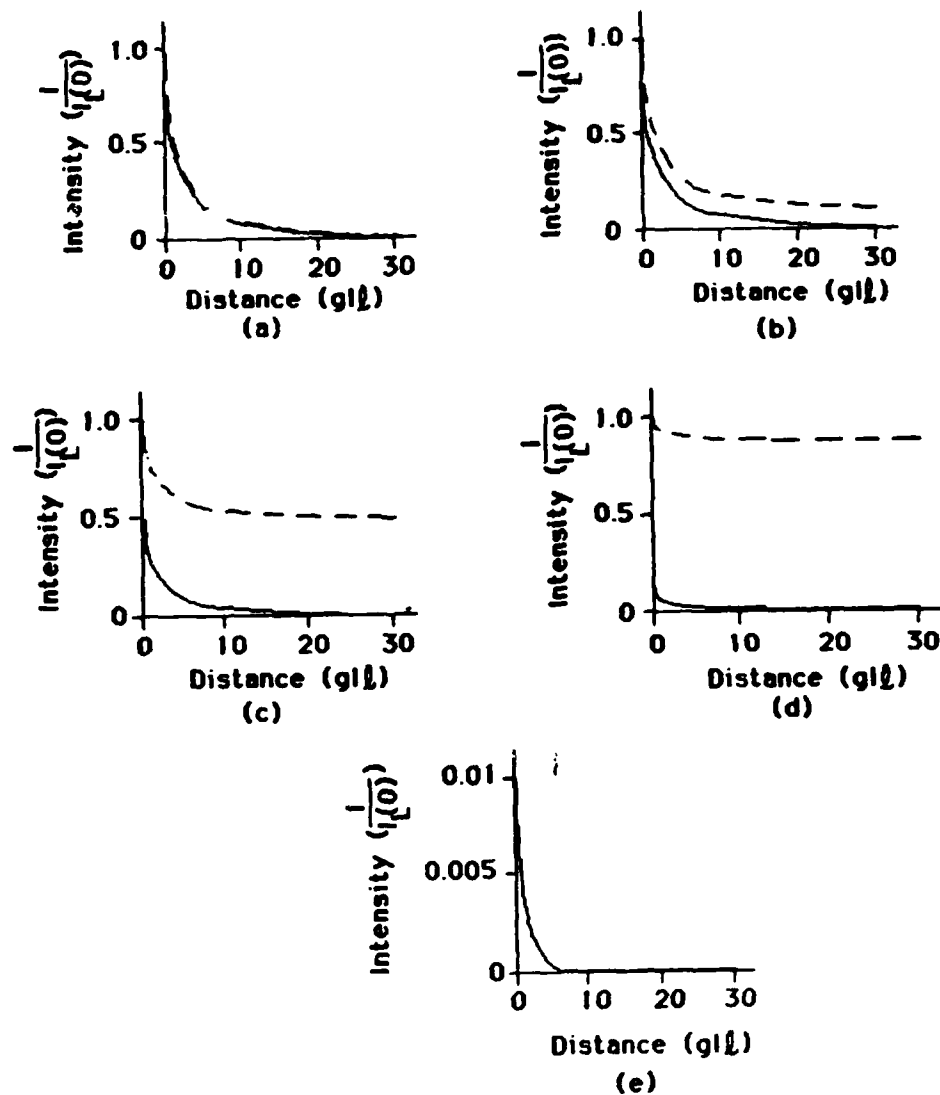


Figure 4.2 The intensities of the pump and Stokes beams are plotted versus the distance z , for several values of the reflectivity R . Dashed line: pump intensity. Solid line: Stokes intensity.

depletion. We have explicitly written the transcendental equation (4.B.11) for the unknown constant $I_L(0)$ in the intermediate gain case. The gain coefficient is a lorentzian function of the laser linewidth divided by the Brillouin linewidth. The gain \times intensity \times length (gIl) product is 25 to 30 at threshold. The large size of the gIl product will be shown to give efficient, accurate discrimination of conjugate waves from nonconjugate waves.

4.C. Temporal Equations

We have observed two temporal effects in SBS. First, for slowly varying pump pulses, the Stokes pulse replicates the pump pulse behavior, except for pulse compression. We have discussed temporal replication and pulse compression in section 3.C. Second, for rapidly varying pump intensities caused by mode beating, the SBS gain dropped and stimulated Raman scattering was observed (see section 3.C). Competition between SBS and SRS for gain in short pulses has been reported elsewhere.⁵⁶⁻⁶¹ Gain competition is analyzed below.

Solutions to the steady state, undepleted, plane wave equations for SBS give

$$I_S = I_0 \exp(gIl) \quad (4.C.1)$$

There are at least three sets of solutions to the transient SBS equations, all giving similar qualitative behavior, but slightly different numerical answers. In each solution the change from the steady state solution (4.C.1) is simply a change in the exponent. For large gain, and step function pulses the gil product becomes^{56,86}

$$gil \rightarrow 2[gIl(t/\tau_B)]^{1/2} - t/\tau_B \quad (4.C.2)$$

where t is the pulsewidth

τ_B is the phonon lifetime

For small gain, step function pulses, and small laser linewidth compared to the Brillouin linewidth, the $gI\ell$ product becomes^{56,105}

$$gI\ell \rightarrow gI\ell[1 - \exp(-t/2\tau_B)] \quad (4.C.3)$$

Finally, an analysis assuming constant gain throughout the interaction region and taking into account linewidth effects leads to^{61,87}

$$gI\ell \rightarrow gI\ell \frac{4gI\ell\tau_B/t}{|1 + gI\ell\tau_B/t|^2} \quad (4.C.4)$$

But if $t \ll gI\ell\tau_B$ then (4.C.4) can be reduced to

$$gI\ell \rightarrow gI\ell(4/gI\ell)(t/\tau_B) \quad (4.C.5)$$

which is linear in t/τ_B . The dependence of the gain on the pulsewidth is plotted in Fig. 4.3, for the three models.

We observed SBS gain reduction and visible backward and forward stimulated Raman scattering for certain mode beating intensity fluctuations with short risetimes and half widths. The phonon lifetime was 180 ps and the gain switching occurred for fluctuations having 400 ps rise and fall times, and 400 ps full widths at half maxima. Note that $gI\ell=25$ for steady state threshold. Since $g_B=0.026$ cm/MW and $g_R=0.016$ cm/MW in the steady state,^{56,62} $g_B/g_R = 2.45$. We can insert measured values of the pulsewidth into equations (4.C.2-5)

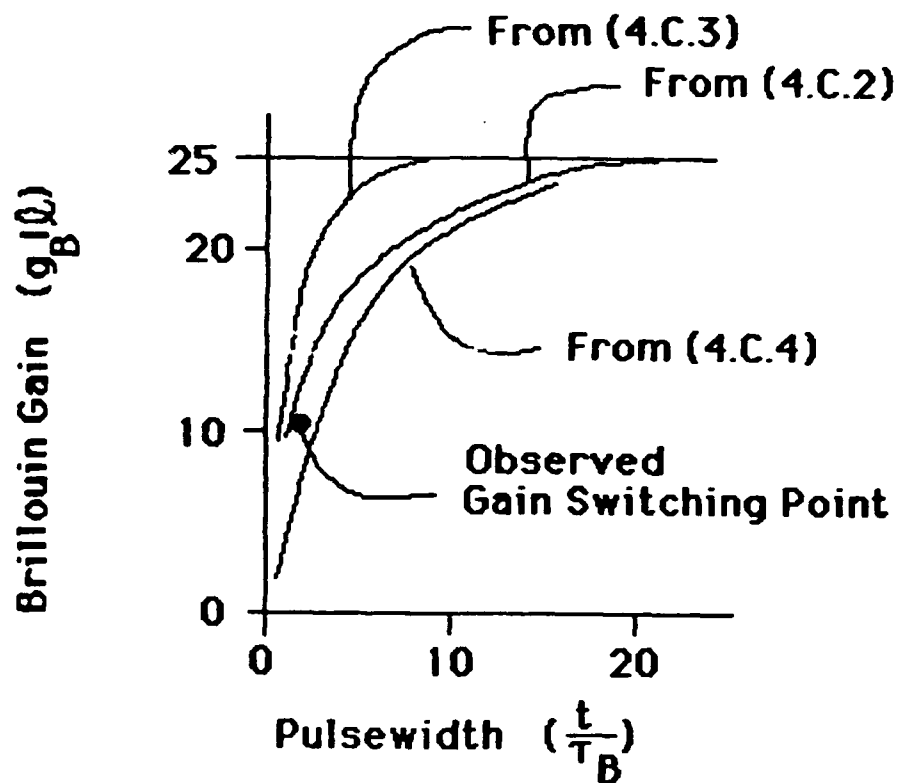


Figure 4.3 The SBS gain reduction for short pulses is plotted versus the pulsewidth. The point where the gain is reduced by a factor of 2.5 is the Raman-Brillouin switching point.

and compare the predictions of these theories to the observed gain switching time.

The three curves in Fig. 4.3 bracket the observed gain switching time nicely. The two upper curves ought to be reduced by linewidth effects, making them even closer to the observed gain switching time. Recall that

$$g = \frac{1}{1 + (\Delta\nu_L)^2 / (\Delta\nu_B)^2} \quad (4.C.6)$$

But for transform limited pulses, $\Delta\nu_L = 1/2\pi t$. Also, $\Delta\nu_B = 1/2\pi\tau_B$. So,

$$g = \frac{1}{1 + (\tau_B)^2 / t^2} \quad (4.C.7)$$

This linewidth effect makes the curves approach the observed Brillouin-Raman gain switching condition (see Fig. 4.4). In fact, when the gain coefficient in eq. (4.C.2) is modified to take into account linewidth effects, it closely approaches the observed gain switching value.

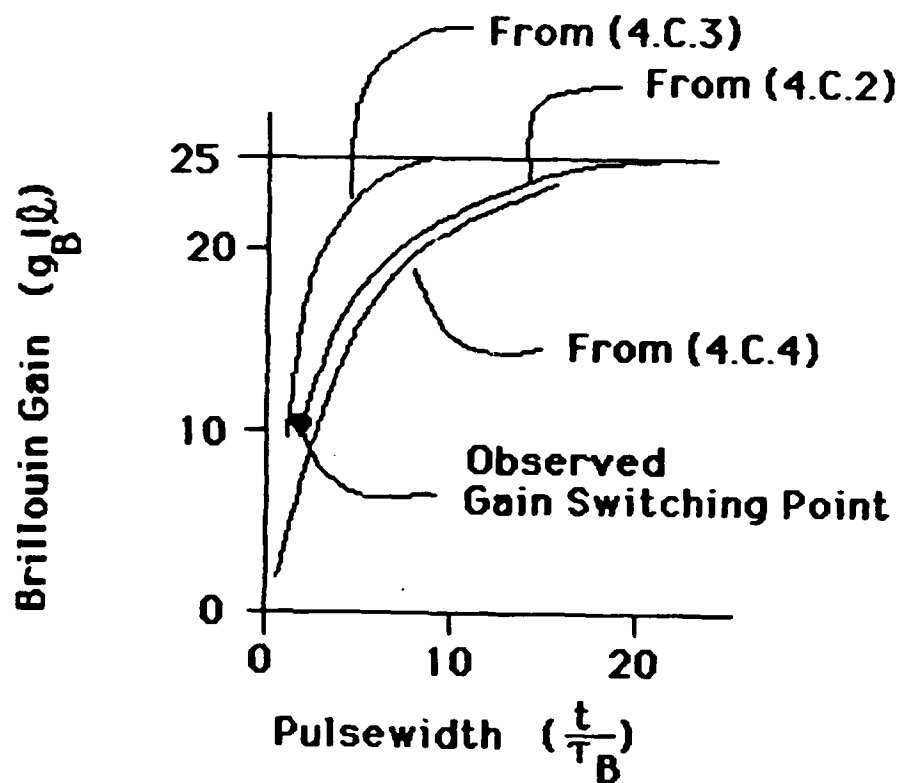


Figure 4.4 The modified SBS gain reduction, taking into account linewidth effects, is plotted versus the pulsewidth. Each curve closely approaches the observed 400 ps switching time.

4.D. SBS in Three Dimensions: Phase Conjugation

The coupled paraxial equations for stimulated Brillouin scattering have not been solved analytically. The coupled nonlinear equations for second harmonic generation (an analogous process) have been solved approximately using a Gauss-Hermite mode decomposition and a perturbative approach.¹⁰⁶ The equations for stimulated Raman scattering, including diffraction and depletion have been solved numerically, using a Gauss-Laguerre decomposition.^{107,108} However, the case of stimulated Brillouin scattering has an additional difficulty: the pump and Stokes waves propagate in opposite directions, making the boundary conditions more complex. In fact, the coupled SBS equations are not Sturm-Liouville equations,¹⁰⁹ so we have no guarantee of orthonormal eigenfunction solutions.¹¹⁰ One numerical approach to solving the coupled SBS equations including depletion and diffraction uses a Fourier decomposition of the transverse coordinates and an iterative "bounce" technique in the axial coordinate.^{16,24,25} This approach may have some problems with stability.^{24,111}

If the pump is undepleted, a single equation results. Solutions of the Stokes gain equation have been developed for the boundary conditions of a lightguide (a reflective tube) when the assumption is made that the pump is highly aberrated. The conclusion is that for accurate (>0.9) wavefront reconstruction in the lightguide geometry, the divergence must exceed 7 to 15 times the diffraction limited divergence.^{14,16,18-25} This has been confirmed by experiments.²⁶⁻³⁵

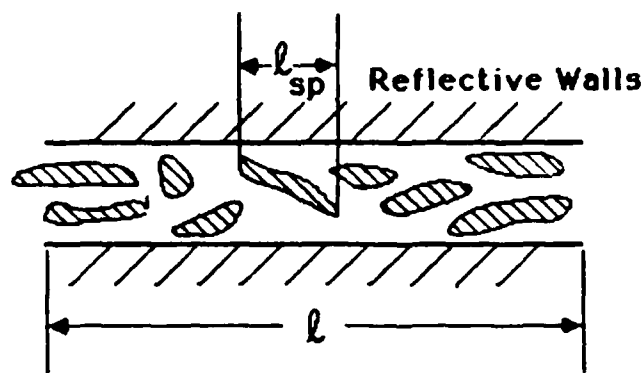
In a lightguide, the boundaries cause reflections, giving many interference maxima and minima in the gain length (see Fig. 4.5(a)). A necessary condition for accurate phase conjugation in lightguide SBS is^{14,22}

$$gIl_{sp} \ll 1 \quad (\text{lightguide}) \quad (4.D.1)$$

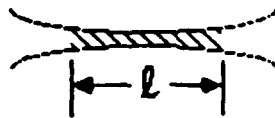
where l_{sp} is the length of the interference maxima (speckles) along the guide. The gain along the length of the guide ($gIl \approx 25$) is much greater than the gain in any of the short interference maxima.

For the case of focused SBS, the geometry is quite different from that in a lightguide. Since there are no walls to reflect the beam and maintain high intensity, the gain length l is shorter. We have shown in section 3.E that the gain length in focused SBS is independent of the strength of aberration, and is slightly less than the speckle length (see Figs. 4.5(b) and 4.5(c)).

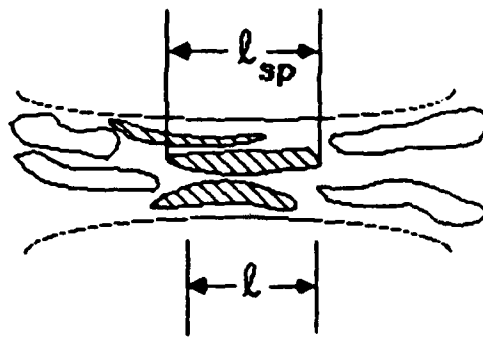
In the common theoretical formalism for focused SBS, two assumptions are carried over from the lightguide formalism: that strong aberration and a gain length much longer than the speckle length are required for accurate phase conjugation.^{13,17,21,38-40} These assumptions are not justified. Experiments have shown that focused SBS produces accurate phase conjugation of diffraction limited beams,^{26,38,41-44} and with weakly aberrated beams.^{26,42} Also, we have shown that the interaction length is independent of the aberration strength and is slightly shorter than the speckle length.



(a)



(b)



(c)

Figure 4.5 The long gain region for SBS in a lightguide (a) is compared to the shorter gain region for SBS in the focused geometry for a diffraction limited beam (b) and for an aberrated beam (c). The gain length l for focused SBS is approximately equal to the speckle length l_{sp} , which is twice the diffraction limited Rayleigh range.

Not only are the fundamental assumptions incorrect, but they lead to incorrect conclusions. The reported solutions predict "radial narrowing," in which the Stokes wave's transverse envelope (cross section) is predicted to be approximately a factor of 2.5 narrower than the pump's cross section,^{13,21,39,40} nonphysical formulas for the fidelity versus the pulse duration,³⁸ and inaccurate estimates of the minimum and maximum correctable divergence in focused SBS.^{13,17,21,37,38} All of the existing theories conclude that accurate phase conjugation is not possible in focused SBS for weakly aberrated beams.^{13,21,37-40} However, the authors of Refs. 26 and 42 specifically mention that they observed accurate phase conjugation for weakly aberrated beams, contrary to theoretical predictions. Similarly, in the experimental section of Ref. 40, the authors report that they did not observe the predicted radial narrowing. It should be noted that no mention is made of the aberrator's spatial frequency in Refs. 26 or 42. The authors of the published theoretical papers generally suggest that radial narrowing and poor fidelity for weakly aberrated beams are not observed experimentally because pump depletion, ignored in the theory but present in the experiments, would enhance the fidelity. We will show that radial narrowing and poor fidelity are not observed because they are outcomes of incorrect assumptions.

There is only one paper in the literature that predicts the phase conjugate fidelity as a function of the focal intensity, or as a function of the aberration strength.¹³ After assuming a strongly aberrated beam ($\xi \geq 10$, where ξ is the far field divergence over the

diffraction limited far field divergence), and after assuming that the pump intensity profile can be approximated as a second order polynomial, the authors of Ref. 13 conclude that

$$F = \frac{1 + \sqrt{(1/2)(gIl)(\xi)/\pi}}{1 + \sqrt{(1/2)(gIl)(\xi)/\pi} + (1/4)(gIl)(\xi)/\pi} \quad (4.D.2)$$

In Fig. 4.6, the predicted (from Ref. 13) and measured (our data) fidelity is plotted as a function of the focal intensity, for $\xi=10$. For $\xi>10$, the predicted fidelity is even lower. There are two important, qualitative differences between the predictions of this theory and our data. First, the predicted fidelity is much lower than that measured, both by us and by the authors of Refs. 42-44. Second, the theory predicts decreasing fidelity for increasing focal intensity, contrary to our data and that reported in Ref. 42. The common theoretical formalism for focused SBS is based on incorrect assumptions, and the conclusions are refuted by published experimental data. Therefore, we have chosen to develop a phenomenological theory which is not based on the incorrect assumptions, and which explains the data.

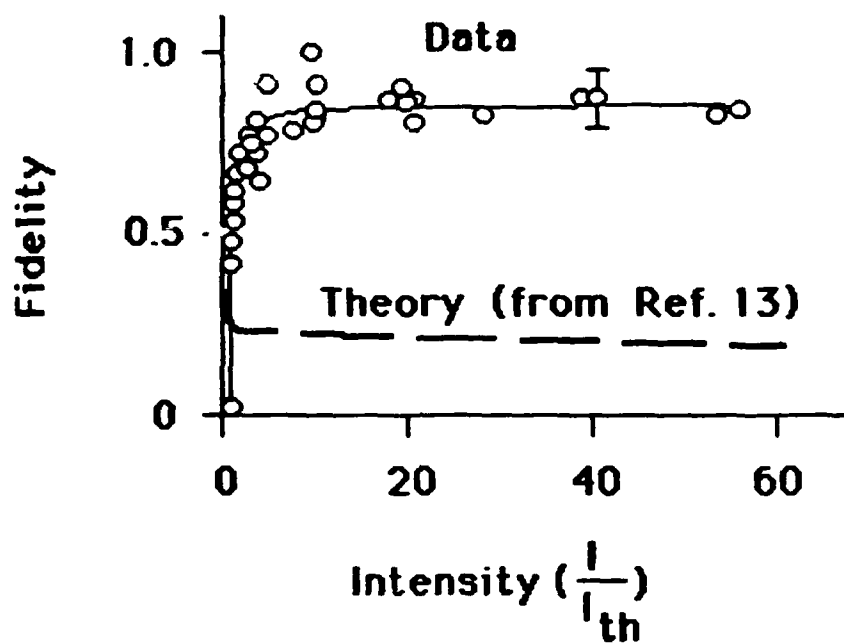


Figure 4.6 The predicted (Ref. 13) and measured phase conjugate fidelity is plotted versus the focal intensity over the SBS threshold intensity.

4.D.1 Boundary Conditions

We have shown in Sections 3.C and 3.D that the gain length for focused SBS is slightly shorter than the speckle length. This is reasonable because the intensity drops near the ends of the speckles. The speckles did not cross or twist appreciably in a gain length. We have also shown that the aberrator we used produced far field intensity patterns that qualitatively resembled single Gauss-Hermite modes. To a rough approximation, the mode index n is equal to $\xi-1$, where $\xi=\theta/\theta_{d1}$, the divergence over the diffraction limited divergence. These conditions allow us to use the boundary conditions of laser resonators to solve the focused SBS equations.

4.D.2 Solutions to the Equations for SBS in a Resonator

We solve the equations for stimulated Brillouin scattering in a resonator, using a Gauss-Hermite eigenmode decomposition. We follow closely the analysis which was developed for stimulated Raman scattering, and reported in Refs. 107 and 108. We start with the undepleted, paraxial, steady-state equations:

$$(\nabla_T^2 - 2ik_L \frac{\partial}{\partial z})E_L = 0 \quad (4.D.5a)$$

and

$$(\nabla_T^2 + 2ik_S \frac{\partial}{\partial z})E_S = \frac{-2ik_S g_S}{2} E_L E_L^* E_S \quad (4.D.5b)$$

where

$$\nabla_T^2 = \frac{\partial^2}{\partial x^2} + \frac{\partial^2}{\partial y^2}$$

and

$$\frac{g_S}{2} = \frac{k\gamma^2\omega_S^2}{16\pi c^2\nu\rho\Gamma_B} \frac{1}{(\Delta\nu_L)^2/(\Delta\nu_B)^2 + 1}$$

We note that $\vec{k} = \vec{k}_L + \vec{k}_S$, so $k = |\vec{k}| \approx k_L + k_S$. Now if we solve these equations in two dimensions (we choose x and z) we can simplify the analysis.

Solutions to the homogeneous pump equation (4.D.5a) are sums of Gauss-Hermite functions. In x and z we have

$$E_L(x, z) = \sum_{n=0}^N p_n u_n(x, z) \quad (4.D.6)$$

where

$$u_n(x, z) = \frac{1}{((\pi)^{1/2} w(z) n! 2^n)^{1/2}} \exp(-(x^2/w^2(z))) H_n(\sqrt{2}x/w(z)) \\ \times \exp[i(kx^2)/2R - i(n+1)\tan^{-1}(z/z_0)] \quad (4.D.7)$$

and $w(z)$ is the beam radius, H_n is the n th Hermite polynomial, z_0 is the Rayleigh range $(\pi w^2(0)/\lambda)$, and R is the radius of curvature of the boundary: $R(z) = -(1/z)(z^2 + z_0^2)$. We note that the pump mode coefficients do not vary along the z -axis. This is true for two reasons. First, we assume no pump depletion. Second, since the Gauss-Hermite modes are eigenmodes of the resonator,⁹⁷ the mode coefficients are constants in z .

We can also expand the Stokes field in sums of Gauss-Hermite modes, making the Stokes mode expansion coefficients dependent on z .

$$E_S(x, z) = \sum_{\alpha=0}^A s_{\alpha}(z) u_{\alpha}(x, z) \quad (4.D.8)$$

Using this expansion, we eliminate transverse derivatives in the equation for the coefficients s_α . The Stokes mode gain equation is

$$\frac{\partial}{\partial \theta} s_\alpha = (1/2)g \sum_{n=0}^N \sum_{m=0}^N \sum_{\beta=0}^A p_n p_m^* s_\beta Q_{\alpha n m \beta} \exp[i(-\alpha+\beta)\theta] \quad (4.D.9)$$

where $\theta = \tan^{-1}(z/z_0)$, z_0 is the length of the focal constriction, and where

$$Q_{\alpha n m \beta} = \frac{1}{2(\alpha!n!m!\beta!)^{1/2}} \int_{-\infty}^{\infty} dx \exp(-4x^2/w^2) H_\alpha(\sqrt{2}x/w) \\ \times H_n(\sqrt{2}x/w) H_m(\sqrt{2}x/w) H_\beta(\sqrt{2}x/w) \quad (4.D.10)$$

A variation of eq. (4.D.9) was derived for a general mode expansion by Zel'dovich in the first paper to analyze phase conjugation.¹ We can think of the phase matching term $\exp[i(-\alpha+\beta)\theta]$ as a z -dependent term multiplying the gain coefficient. The real part decreases the gain and the imaginary part introduces dephasing between the modes s_α and s_β . We can think of the mode overlap integral $Q_{\alpha n m \beta}$ as a four-dimensional matrix. Further assumptions will reduce the dimensionality of Q . Since the values of $Q_{\alpha n m \beta}$ are important to the analysis, we have calculated^{112,113} and tabulated some Q values in Tables 4.1 and 4.2. The Q values are independent of ordering of the coefficients, and the largest values in each column or row of Table 4.1 are the "diagonal" terms Q_{nnnn} . The Q values are constants in z .

Table 4.1

Values of the Overlap Integral $Q_{\alpha n m \beta}$ for $\alpha = \beta$, $n = m$

α	n	0	1	2	3	4
0		.398	.199	.150	.125	.109
1		.199	.299	.175	.137	.117
2		.150	.174	.255	.159	.128
3		.124	.137	.159	.229	.148
4		.109	.117	.128	.148	.210

Table 4.2

Values of the Overlap Integral $Q_{\alpha n m \beta}$ for $\alpha, \beta, n = 0, 1$

$Q_{0001} = 0.000$	$Q_{0111} = 0.000$
$Q_{0002} = -.141$	$Q_{0112} = 0.071$
$Q_{0003} = 0.000$	$Q_{0113} = 0.000$
$Q_{0004} = 0.061$	$Q_{0114} = -.092$
$Q_{1002} = 0.000$	$Q_{1112} = 0.000$
$Q_{1003} = -.122$	$Q_{1113} = -.076$
$Q_{1004} = 0.000$	$Q_{1114} = 0.000$
$Q_{2003} = 0.000$	$Q_{2113} = 0.000$
$Q_{2004} = -.108$	$Q_{2114} = -.076$
$Q_{3004} = 0.000$	$Q_{3114} = 0.000$

In the section on boundary conditions, we argued that to a first approximation, the pump field can be taken to be a single Gauss-Hermite mode u_n throughout the interaction region (see also section 3.E, particularly Figures 3.14 and 3.15). Increasing the aberration strength increased the number of spots in the transverse axis, and is modeled by simply increasing the mode index n of the pump. For a beam aberrated to have a divergence equal to ξ times the diffraction limit, the number of spots is ξ , and the number of nodes n is equal to $\xi-1$. In this case, the pump field can be expressed as a single mode coefficient times the n th Gauss-Hermite mode:

$$E_L(x,z) = p_n u_n(x,z) \quad (4.D.11)$$

Then equation (4.D.9) for the Stokes mode gain becomes

$$\frac{\partial}{\partial \theta} s_\alpha = (1/2) g p_n p_n^* \sum_{\beta=0}^A s_\beta Q_{\alpha n n \beta} \exp[i(-\alpha+\beta)\theta] \quad (4.D.12)$$

Diffraction Limited Pump

We first solve the gain equations for a diffraction limited pump. For $\xi=1$, we have $n=0$ and the spot size w is equal to the diffraction limited spot size w_{d1} . The length of the focal constriction, z_0 , equals the diffraction limited Rayleigh range z_{Rd1} . The interaction length constrains the "resonator" boundaries to $-z_{Rd1} \leq z \leq z_{Rd1}$. For this case, $p_n = p_0$. Let us examine eq. (4.D.12), defining $g'_{\alpha 0 0 \beta} = (1/2) g p_0 p_0^* Q_{\alpha 0 0 \beta}$. Then we have

$$\frac{\partial}{\partial \theta} s_{\alpha} = \sum_{\beta=0}^A g'_{\alpha 0 0 \beta} s_{\beta} \exp[i(-\alpha+\beta)\theta] \quad (4.D.13)$$

The mode that overlaps with the pump (the phase conjugate mode) is s_0 . So, the equation giving the gain of the conjugate is

$$\frac{\partial}{\partial \theta} s_0 = \sum_{\beta=0}^A g'_{0 0 0 \beta} s_{\beta} \exp[i(-0+\beta)\theta] \quad (4.D.14)$$

Explicitly writing out the sum, we have

$$\frac{\partial}{\partial \theta} s_0 = g'_{0 0 0 0} s_0 + g'_{0 0 0 1} s_1 e^{1\theta} + g'_{0 0 0 2} s_2 e^{2i\theta} + \dots \quad (4.D.15)$$

We know that the total gain of s_0 is e^{25} , so this helps us determine the scale of contribution of s_0 , s_1 , s_2 , etc., to the gain of s_0 . Referring to our table of Q values (Table 2.2), we examine the value of Q_{0001} and see that it is 0.000. Thus mode s_1 (and in fact all odd numbered modes) have no contribution to the gain of s_0 . Q_{0002} is -.141 (which represents loss), Q_{0003} is 0.000, and Q_{0004} is 0.061.

Now, even if we neglect the $e^{i(-\alpha+\beta)\theta}$ term, we see that each of the contributions of other modes to the gain of s_0 is negligible. (Note that we have taken $\exp[i(-\alpha+\beta)\theta] = 1$. Using the actual value of $\exp[i(-\alpha+\beta)\theta]$ can only decrease the contributions of non-phase matched terms.) Let us recall that the gain product $gI\ell$ is approximately 25 at SBS threshold. This product gives the intensity gain. The amplitude gain product is $(1/2)gI\ell$, or 12.5. If we assume that the contribution of mode s_0 to its own amplitude gain is $e^{12.5}$,

we see that the next highest gain contributor, s_4 , contributes a gain which is related to the ratio of Q_{0004}/Q_{0000}

$$\frac{\text{contribution of } s_4}{\text{contribution of } s_0} = \frac{e^{12.5(Q_{0004}/Q_{0000})}}{e^{12.5}} = 2.5 \times 10^{-5} \quad (4.D.16)$$

and the contribution of s_4 is utterly negligible in the gain of s_0 . We note that for nonzero Q 's their magnitude monotonically decreases with increasing difference between α and β . This means that s_6 and higher even numbered modes contribute even less to the gain of s_0 than s_4 . We find that the only contributor to the s_0 gain is itself (s_0), so we make $\alpha - \beta = 0$ in the gain equation (4.D.14). Gain selection allows us to ignore the phase matching term $\exp[i(-\alpha + \beta)\theta]$.

The gain equation (4.D.14) for the conjugate mode s_0 can now be written

$$\frac{\partial}{\partial \theta} s_0 = g'_{0000} s_0 \quad (4.D.17)$$

This gives simple exponential growth of s_0 . We note that the overlap integrals have selected only the s_0 term as a contributor to its own gain, and non-phase matched contributions are discarded because of their low gain.

We can use similar arguments to examine the buildup of nonconjugate modes. When pumped by p_0 , we have, as the first nonconjugate mode gain equation

$$\begin{aligned} \frac{\partial}{\partial \theta} s_1 = & g'_{1000} s_0 e^{1\theta} + g'_{1001} s_1 + g'_{1002} s_2 e^{-1\theta} \\ & + g'_{1003} s_3 e^{-21\theta} + \dots \end{aligned} \quad (4.D.18)$$

We find that s_0 and s_2 contribute nothing to the growth of s_1 , and the contribution of s_3 (and higher odd index s_n) is negligible. So, only s_1 contributes to its own gain. We have

$$\frac{\partial}{\partial \theta} s_1 = g'_{1001} s_1 \quad (4.D.19)$$

which again corresponds to simple exponential growth. The gain of the nonconjugate mode s_1 , compared to the gain of the conjugate, is related to Q_{1001}/Q_{0000}

$$\frac{\text{gain of nonconjugate } (s_1)}{\text{gain of conjugate } (s_0)} = \frac{e^{12.5(Q_{1001}/Q_{0000})}}{e^{12.5}} = 1.9 \times 10^{-3} \quad (4.D.20)$$

Thus, there is excellent gain discrimination of the conjugate mode from the nonconjugate. Similarly, for the next nonconjugate mode, s_2 , we have

$$\frac{\partial}{\partial \theta} s_2 = g'_{2002} s_2 \quad (4.D.21)$$

and

$$\frac{\text{gain of } s_2}{\text{gain of } s_0} = \frac{e^{12.5(Q_{2002}/Q_{0000})}}{e^{12.5}} = 4.1 \times 10^{-4} \quad (4.D.22)$$

By comparing eq. (4.D.20) to eq. (4.D.22), we see that the degree of discrimination against nonconjugate modes is related to the difference in mode indices. The larger the difference in mode indices, the better the discrimination.

Looking back over the development of the gain equations for s_0 , s_1 , and s_2 when pumped by a single diffraction limited mode p_0 , we conclude that the generalized gain equation (4.D.13) can be simplified to

$$\frac{\partial}{\partial \theta} s_\alpha = g'_{\alpha 0 0 \alpha} s_\alpha \quad (4.D.23)$$

The gain has eliminated the phase-mismatched modes. Only s_α contributes to the gain of s_α , so the equation gives simple exponential growth for each mode.

We can calculate the total nonconjugate fraction of the backscattered field by adding up the gain fractions derived in eqs. (4.D.20) and (4.D.22) for the few nearest modes (the more distant modes contribute little to the nonconjugate, and can be neglected).

$$\frac{E_{\text{non}}}{E_{\text{con}}} = \sum_{\alpha} \frac{s_\alpha}{s_0} \quad (\alpha \neq 0) \quad (4.D.24)$$

In order to calculate the nonconjugate fraction, we added up the gain fractions of the first 16 nonconjugate modes.¹¹² The nonconjugate fraction is

$$\frac{E_{\text{non}}}{E_{\text{con}}} = 1.9 \times 10^{-3} + 4.1 \times 10^{-4} + \dots = 2.8 \times 10^{-3} \quad (4.D.25)$$

We assume that the phase conjugate fidelity equals $1 - I_{\text{non}}/I_{\text{con}}$. We further assume that the nonconjugate intensity fraction $I_{\text{non}}/I_{\text{con}}$ is equal to the nonconjugate amplitude fraction $E_{\text{non}}/E_{\text{con}}$ squared. In the case of an unaberrated pump, this is equal to $(2.8 \times 10^{-3})^2$, or 7.84×10^{-6} . Thus, the predicted fidelity is perfect to better than 1 part in 10^5 when the pump is diffraction limited.

Aberrated Pump

We have shown that for our variable aberrator, an increase in the divergence over the diffraction limited divergence ($\xi = \theta/\theta_{d1}$) is roughly equivalent to increasing the mode index ($n = \xi - 1$). For example, if a beam is aberrated to twice the diffraction limited divergence, $\xi = 2$ and $n = 1$. By completely analogous arguments to eqs. (4.D.12-25), but for $n = 1$, we have

$$\frac{E_{\text{non}}}{E_{\text{con}}} = 1.5 \times 10^{-2} + 5.5 \times 10^{-3} + \dots = 2.3 \times 10^{-2} \quad (4.D.26)$$

and the nonconjugate intensity fraction is $(2.3 \times 10^{-2})^2$, or 5.3×10^{-4} . In Table 4.3, we list the nonconjugate intensity fractions for $1 \leq \xi \leq 6$. Less than 1 percent of the backscattered light intensity is nonconjugate, regardless of the aberration strength.

Table 4.3

Nonconjugate Fraction as a Function of Aberration
Strength for g11-25. (Single Aberration Axis)

Divergence ($\xi = \theta/\theta_{dl}$)	n	I_{non}/I_{con}
1	0	7.84×10^{-6}
2	1	5.35×10^{-4}
3	2	9.56×10^{-4}
4	3	1.36×10^{-3}
5	4	1.76×10^{-3}
6	5	2.18×10^{-3}

Two Transverse Axes of Aberration

The preceding analysis examined the case of focused SBS with a pump beam having intensity modulation in just one transverse axis, corresponding to TEM_{n0} modes, where $n \geq 1$. Since the equations are separable, we can analyze the y-dependence in the same way we analyzed the x-dependence. For equal amounts of aberration in both transverse axes, the analysis is particularly simple. The Stokes mode equations take the form

$$\frac{\partial}{\partial \theta} s_{\alpha}^{\alpha} = g_{\alpha n n \alpha}^{\alpha} s_{\alpha}^{\alpha} \quad (4.D.27)$$

where

$$g_{\alpha n n \alpha}^{\alpha} = (1/2) g p_n^n p_n^{n*} Q_{\alpha n n \alpha} Q_{\alpha n n \alpha}^{\alpha} \quad (4.D.28)$$

and p_n^n is the TEM_{nn} mode coefficient for the pump beam
 s_{α}^{α} is the $TEM_{\alpha\alpha}$ mode coefficient for the Stokes beam

Thus, the two dimensional Stokes mode equations are identical in form to the one-dimensional equations, but the gain is proportional to the square of the mode overlap integral $Q_{\alpha n n \alpha}$. This leads to improved discrimination of the conjugate from the nonconjugate waves for a given $n \geq 1$. In other words, the maximum amount of correctable aberration (ξ_{cr}) is higher for 2-D aberrated beams than for 1-D aberrated beams.

Focal Intensity Effects

Up to this point, we have assumed that the pump intensity was near the SBS threshold, used $g_{II}=25$, and ignored pump depletion. The predicted phase conjugate fidelity is nearly unity, independent of the aberration strength. Note that if we used $g_{II}=30$, the nonconjugate intensity fraction would be lower and the fidelity would be higher. We conclude that the phase conjugate fidelity ought to remain near unity for all intensities above the SBS threshold.

We can calculate the Stokes beam's amplification even during saturation by using our knowledge of the reflectivity as a function of the pump intensity. The Stokes amplification for intensities above the SBS threshold is

$$\frac{I_S(0)}{I_S(l)} = e^{25 \frac{R}{(R_{th} - 0.001)} \frac{I_L}{I_{Lth}}} \quad (4.D.27)$$

where R is the measured reflectivity, R_{th} is the reflectivity at threshold (assumed to be 0.1 percent), I_L is the pump intensity, and I_{Lth} is the threshold pump intensity. So, the "effective" gain product $g_{II_{eff}}$ is $25 + \ln[(R/.001)(I_L/I_{Lth})]$. For intensities below the SBS threshold, $g_{II_{eff}} \approx 25(I_L/I_{Lth})$.

We phenomenologically calculated the nonconjugate intensity fraction I_{non}/I_{con} for pump intensities above and below the SBS threshold, by using $g_{II_{eff}}$ instead of $g_{II}=25$ in equations (4.D.16-22). Even this rough phenomenological gain argument should give

correct qualitative predictions of the fidelity, both above and below the SBS threshold. Below threshold, the g_{eff} estimates should be valid. Above threshold, inaccuracies in g_{eff} due to pump depletion simply do not matter, because the nonconjugate fraction is negligibly small for all intensities above the SBS threshold.

Comparison to Experimental Data

The values of the predicted phase conjugate fidelity are plotted versus the intensity over the SBS threshold in Fig. 4.7. The bold dashed line is the theory, and the solid line is the data. It is clear that the theory qualitatively agrees with the data. In the theory, the fidelity is near unity, regardless of the aberration strength, for all pump beams with focal intensities above the SBS threshold, and the fidelity declines for pump beams having focal intensities below the SBS threshold. The data shows high (≈ 0.85) fidelity, regardless of the aberration strength, for all pump beams above 5 times the SBS threshold. The measured fidelity is slightly lower, and rolls off at higher intensities, compared to the predicted fidelity. According to this theory, the maximum correctable aberration for focused SBS is that aberration which reduces the focal intensity to below the SBS threshold. So, the maximum correctable aberration should be different for each laser power setting: higher power lasers can correct stronger aberrations. This prediction agrees qualitatively with the data. The measured fidelity rolled off as the aberration reduced the focal intensity to approximately 5 times the SBS threshold.

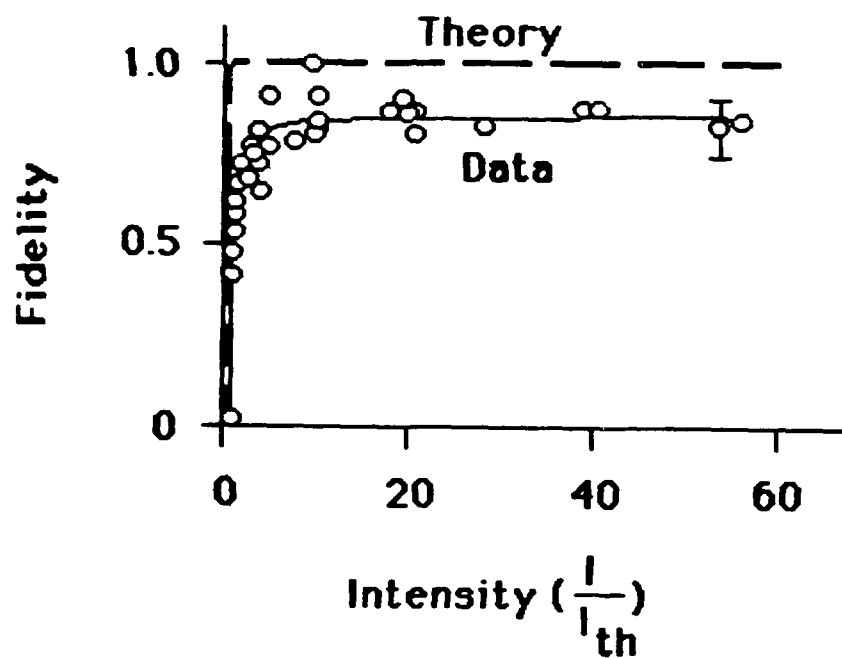


Figure 4.7 The phase conjugate fidelity is plotted as a function of the intensity over the SBS threshold. The solid line is a fit to our data. The dashed line is our theoretical prediction.

There are several possible reasons why the measured phase conjugate fidelity is slightly worse than our theory predicts. The many assumptions that were used in our theory to make it analytically tractable may have led to solutions which give predictions of better fidelity than is observed. In particular, the assumption of the pump being a single Gauss-Hermite mode was a very rough approximation. The pump intensity profile gave an appropriate number of spots in approximately the correct locations, but the intensity of the spots decreased, rather than increased (as do the Gauss-Hermite modes) near the edges of the pattern. Also, some of the speckles ended or began in the gain region. Both these observations show that using a single Gauss-Hermite mode for the pump is a crude approximation.

It is clear that more work needs to be done to make the theory more complete and accurate, especially for near-threshold intensities. A full numerical investigation of the propagation and gain of the pump and Stokes beams was beyond the scope of this dissertation, but such a project might be appropriate for a theoretical dissertation. Perhaps the work in Refs. 107 or 108 could be extended to include a Gauss-Hermite mode decomposition.

To summarize this chapter, a theory for the phase conjugate fidelity of focused SBS has been presented. A Gauss-Hermite mode decomposition was used in the undepleted pump limit, and the pump was assumed to be a single Gauss-Hermite mode. In contrast to existing theories, which predict inaccurate phase conjugation for weakly aberrated beams, this theory predicts accurate phase conjugation,

independent of the aberration strength, for all intensities above the SBS threshold. This is in qualitative agreement with the data.

Chapter 5. Conclusions

We have experimentally measured the effect of the aberrated focal intensity on the stimulated Brillouin scattering (SBS) phase conjugate fidelity. We directly measured the reduction in focal intensity of the brightest aberrated spot and used this intensity (not the average focal intensity) in our analysis of the data. Regardless of the aberration strength, if the focal intensity was greater than 5 times the SBS threshold intensity, the fidelity was high (greater than 0.8). As the focal intensity was reduced (either by aberrating the beam or by turning down the laser power) so that the focal intensity approached the SBS threshold intensity, the fidelity declined. To our knowledge, this is the first direct measurement of the effect of the aberrated focal intensity on SBS phase conjugate fidelity.

These measurements appear to be in qualitative agreement with published experimental results. In some published experimental results, the fidelity improves as the laser power increases, for a given aberration strength. Other data shows that the fidelity improves as the aberration strength decreases, for a given laser power. Our data may explain the wide variation in the reported values of the maximum correctable aberration strength for focused SBS. We obtained a different value of the "maximum" correctable aberration strength for each laser power setting.

The measurements refute a primary assumption of the common theoretical formalism: that strong aberration is a necessary condition for accurate phase conjugation in focused SBS. We found that the fidelity decreases for increasing aberration strength, because the aberration reduced the focal intensity. Our reflectivity measurements showed that the gain length was independent of the aberration strength, and was slightly less than the length of the interference maxima (speckles) at the focus. This data refutes another assumption of the common theoretical formalism: that many speckles must occur along the gain length for accurate phase conjugation in focused SBS. Also, our data refute the conclusion in the published theory that the phase conjugate fidelity would be sharply reduced due to a significant radial narrowing of the backscattered beam compared to the pump beam. The radius of the backscattered beam was approximately equal to the radius of the pump beam.

Since our data refuted the assumptions and the conclusions of the common theoretical formalism, we developed a phenomenological theory which did not use those assumptions. We assumed that the equations for focused, undepleted SBS could be solved using the boundary conditions of a laser resonator. By using a Gauss-Hermite mode decomposition, and by assuming that the pump could be described by a single Gauss-Hermite mode, we were able to derive simple analytic expressions for the gain of the conjugate and the nonconjugate modes. We calculated predictions of the nonconjugate intensity fraction of the backscattered light for several aberration strengths and spatial

frequencies. The theory predicted accurate phase conjugation, independent of the aberration strength, for all intensities over the SBS threshold. The theory qualitatively agrees with our data and other published experimental results.

We also measured the accuracy of temporal and spectral replication of the pump pulse by the backscattered (Stokes) pulse. Using time-resolved intensity diagnostics and Fourier analysis, we found accurate temporal and spectral replication, except during pulse compression and intense mode beating. We developed a phenomenological model for the pulse compression based on observed values of the reflectivity as a function of intensity. The model was in qualitative agreement with the pulse compression data. During mode beating, the Stokes pulse replicated the pump pulse, except for the most intense spike. During that spike, SBS gain depletion occurred. To our knowledge, this is the first time-resolved measurement of partial pulse replication by SBS. We assumed that stimulated Raman scattering depleted the SBS gain during mode beating spikes. We found that the pulsewidths for which we observed SBS gain depletion were as predicted in the published theory.

We developed two new techniques and devices for this dissertation. We used a variable phase grating aberrator to distort the pump beam, and we directly measured the focal intensity reduction due to the aberrator, using a computerized far field video image analysis system. These techniques and devices may be useful for

other researchers studying phase conjugation and imaging accuracy in a variety of nonlinear optical processes.

Perhaps the most intriguing unresolved question has to do with image reconstruction accuracy. A quantitative study of the spatial frequencies of images reproduced by focused SBS under a wide range of aberration conditions would make an excellent follow-on project. Another fruitful area for further study would be a computer analysis of focused SBS, in the undepleted pump regime, when the pump beam consists of a sum of Gauss-Hermite modes (instead of a single mode). Perhaps an existing code which has been developed to study stimulated Raman scattering using a Gauss-Laguerre mode decomposition could be modified to analyze non-rotationally symmetric intensity distributions, if the Gauss-Hermite decomposition were used. Finally, an experimental study of the phase conjugate fidelity of focused SBS as a function of the aberration strength for irregular or turbulent aberrations would be an attractive point of comparison with the regular, smooth aberrations studied in this dissertation. The simplicity and applicability of SBS for many uses of phase conjugation ensures that much more research will be done on this fascinating physical effect.

References

1. B.Ya. Zel'dovich, V.I. Popovichev, V.V. Ragul'skii, and F.S. Faizullov, JETP Lett 15, 109 (1972).
2. B.Ya. Zel'dovich, N.F. Pilipetskii, and V.V. Shkunov, Sov. Phys. Usp. 25, 713 (1983).
3. H.Z. Cummins and P.E. Shoen, "Linear Scattering From Thermal Fluctuations," in Laser Handbook, F.T. Arecchi and E.O. Schulz-Dubois, eds., North Holland, Amsterdam, 1972. pp. 1029-1075.
4. L. Brillouin. Ann. Phys. (Paris) 17, 88 (1922).
5. L. Brillouin. Wave Propagation and Group Velocity, Academic Press, New York, 1960.
6. R.Y. Chiao, C.H. Townes, and B.P. Stoicheff, Phys. Rev. Lett. 12, 592 (1964).
7. E. Garmire and C.H. Townes, Appl. Phys. Lett. 5, 84 (1964).
8. E.E. Hagenlocker and W.G. Rado, Appl. Phys. Lett. 7, 236 (1965).
9. R.G. Brewer, Phys. Rev. 140. A800 (1965).

10. T.A. Wiggins, R.V. Wick, and D.H. Rank, *Applied Optics* 5, 1069, (1966).
11. I.M. Beldyugin, M.G. Galushkin, E.M. Zemskov, and V.I. Mandrosov, *Sov. J. Quantum Electron.* 6, 1349 (1976).
12. B.Ya. Zel'dovich and V.V. Shkunov, *Sov. J. Quantum Electron.* 7, 610 (1977).
13. N.B. Barnova, B.Ya. Zel'dovich, and V.V. Shkunov, *Sov. J. Quantum Electron.* 8, 559 (1978).
14. B.Ya. Zel'dovich and V.V. Shkunov, *Sov. J. Quantum Electron.* 8, 15 (1978).
15. N.B. Baranova and B.Ya. Zel'dovich, *Sov. J. Quantum Electron* 10, 172 (1980).
16. R.H. Lehmborg, *Optics Commun.* 43, 369 (1982).
17. B.Ya. Zel'dovich, N.F. Pilipetskii, and V.V. Shkunov, "Experimental Investigation of Wave-Front Reversal Under Stimulated Scattering," in *Optical Phase Conjugation*, R.A. Fisher, ed., Academic Press, New York, 1983. pp. 135-167.
18. B.Ya. Zel'dovich and T.V. Yakovleva, *Sov. J. Quantum Electron.* 11, 186 (1981).

19. P. Suni and J. Falk, J. Opt. Soc. Am. B 3, 1681 (1986).
20. B.Ya. Zel'dovich and T.V. Yakovleva, Sov. J. Quantum Electron. 10, 181 (1980).
21. B.Ya. Zel'dovich, N.F. Pilipetskii, and V.V. Shkunov, Principles of Phase Conjugation, Springer-Verlag, Berlin, 1985.
22. V.G. Sidorovich, Sov. Phys. Tech. Phys. 21, 1270 (1977).
23. R.W. Hellwarth, J. Opt. Soc. Am. 68, 1050 (1978).
24. R.H. Lehberg and K.A. Holder, Phys. Rev. A 22, 2156 (1980).
25. R.H. Lehberg, J. Opt. Soc. Am. 73, 558 (1983).
26. N.G. Basov, V.F. Efimkov, I.G. Zubarev, A.V. Kotov, A.B. Mironov, S.I. Mikhailov, and M.G. Smirnov, Sov. J. Quantum Electron. 2, 455 (1979).
27. V.I. Popovichev, V.V. Ragulskii, and F.S. Faizullov, JETP Lett. 19, 196 (1974).
28. N.F. Pilipetskii, V.I. Popovichev, and V.V. Ragulskii, Sov. Phys. Dokl. 24, 845 (1980).
29. V. Wang and C.R. Giuliano, Optics Lett. 2, 4 (1978).

30. R.C. Lind and C.R. Giuliano, IEEE J. Quantum Electronics, QE-
15, 71D (1979).
31. R. Mays and R.J. Lysiak, Optics Commun. 31, 89 (1979).
32. R. Mays and R.J. Lysiak, Optics Commun. 32, 334 (1980).
33. D.T. Hon, Optical Engineering 21, 252 (1982).
34. P. Suni and J. Falk, paper MHH4 in CLEO '87 Technical Digest,
Optical Society of America, Washington, D.C., 1987. pp. 22-24.
35. P. Suni and J. Falk, Optics Lett. 12, 838 (1987).
36. V.N. Blaschuk, B.Ya. Zel'dovich, N.A. Mel'nikov, N.F.
Pilipetskii, V.I. Popovichev, and V.V. Ragul'skii, Sov. Tech.
Phys. Lett. 3, 83 (1977).
37. V.I. Bespalov, A.A. Betin, and G.A. Pasmanik, Radiophys. Quantum
Electron. 20, 544 (1977).
38. A.A. Betin, A.F. Vasil'ev, O.V. Kulagin, V.G. Manishin, and V.E.
Yashin, Sov. Phys. JETP 62, 468 (1986).
39. N.B. Baranova and B.Ya. Zel'dovich, Sov. J. Quantum Electron. 10,
555 (1980).

40. V.I. Bespalov, A.A. Betin, and G.A. Pasmanik, Radiophys. Quantum Electron. 21, 675 (1979).
41. V.N. Belousov, L.A. Bol'shov, N.G. Koval'skii, and Yu.K. Nizienko, Sov. Phys. JETP 52, 1071 (1980).
42. V.I. Kryzhanovskii, V.A. Serebryakov, and V.E. Yashin, Sov. Phys. Tech. Phys. 27, 825 (1983).
43. V.E. Yashin, V.I. Kryzhanovskii, and V.A. Serebryakov, Sov. J. Quantum Electron. 12, 1086 (1983).
44. N.F. Andreev, V.I. Bespalov, M.A. Dvoretiskii, and G.A. Pasmanik, Sov. Phys. JETP 58, 688 (1984).
45. M. Slatkine, I.J. Bigio, B.J. Feldman, and R.A. Fisher, Optics Lett. 7, 108 (1982).
46. M.C. Gower, Optics Lett. 7, 423 (1982).
47. M.C. Gower, Optics Lett. 8, 70 (1983).
48. E. Armandillo and D. Proch, Optics Lett. 8, 523 (1983).
49. "The New DCR-2 Nd:YAG Laboratory Laser System," specification sheet, Spectra-Physics, Mountain View, California, 1984.

50. Y.K. Park and R.L. Byer, *Optics Commun.* 37, 411 (1981).
51. D.C. Hanna and L.C. Laycock, *Opt. Quant. Electron.* 11, 153 (1979).
52. A.J. Berry, D.C. Hanna, and C.G. Sawyers, *Optics Commun.* 40, 54 (1981).
53. D.C. Hanna and Y.W.J. Koo, *Optics Commun.* 43, 414 (1982).
54. I.D. Carr and D.C. Hanna, *Appl. Phys. B* 36, 83 (1985).
55. A.Z. Grasyuk, I.G. Zubarev, and N.V. Suyazov, *JETP Lett.* 16, 166 (1972).
56. W. Kaiser and M. Maier, "Stimulated Rayleigh, Brillouin, and Raman Spectroscopy," in Laser Handbook, F.T. Arecchi and E.O. Schulz-Dubois, eds. North-Holland, Amsterdam, 1972. pp. 1077-1150.
57. M.D. Skeldon, P. Narum, and R.W. Boyd, *Proc. SPIE* 613, 93 (1986).
58. P. Narum, M.D. Skeldon, and R.W. Boyd, paper ThD3 in CLEO '86 Technical Digest, Optical Society of America, Washington, D.C., 1986. pp. 248, 249.

59. P. Narum, M.D. Skeldon, and R.W. Boyd, IEEE J. Quantum Elect. OE-22, 2161 (1986).
60. D. von der Linde, M. Maier, and W. Kaiser, Phys. Rev. 178, 11 (1969).
61. E.E. Hagenlocker, R.W. Minck, and W.G. Radon, Phys. Rev. 154, 226 (1967).
62. Y.R. Shen and Y.J. Shaham, Phys. Rev. 163, 224 (1967).
63. N.M. Kroll, J. Appl. Phys. 36, 34 (1965).
64. V.S. Starunov and I.L. Fabelinskii, Sov. Phys. Usp. 12, 463 (1970).
65. K. Daree and W. Kaiser, Phys. Rev. Lett. 26, 816 (1971).
66. M.V. Vasil'ev, V.U. Venediktov, A.A. Leshchev, V.G. Sidorovich, and N.S. Shlyapochnikova, Sov. Phys. Tech. Phys. 28, 1210 (1984).
67. Newport Corporation 1983-84 Catalog, Newport Corporation, Fountain Valley, California, 1983. p. 146.
68. Tek Products 1987, Tektronix Corporation, Beaverton, Oregon, 1987. pp. 239, 248, 347, 348.

69. "HP 98827A Waveform Analysis," Hewlett Packard Desktop Computer Division, Fort Collins, Colorado, 1982.
70. V.F. Efimkov, I.G. Zubarev, A.V. Kotov, A.B. Mironov, S.I. Mikhailov, and M.G. Smirnov, Sov. J. Quantum Electron. 10, 211 (1980).
71. D.T. Hon, Opt. Eng. 21, 252 (1982).
72. M.J. Damzen and M.H.R. Hutchinson, Optics Lett. 8, 313 (1983).
73. M.V.R.K. Murty, "Lateral Shearing Interferometers," in Optical Shop Testing, D. Malacara, ed., John Wiley and Sons, New York, 1978. pp. 105-148.
74. C.K. Davis, "SAINT Interferogram Reduction Software," Rockwell Power Services, Kirtland Air Force Base, New Mexico, 1983.
75. "Final Quality Control Report, Two Inch Diameter Shear Plate Fabrication," Martin Marietta Laser Systems Technology Division, Development Optics Facility, Kirtland Air Force Base, New Mexico, job number 40905-7, 1984.
76. "Model TN 2505 Specification Sheet," General Electric, Liverpool, New York, pamphlet number GET-6803.

77. "Model 505 and Model 515 Video Frame Grabber User's Manual," Poynting Products, Oak Park, Illinois, 1983.
78. C.A. Thies, "MULTI Image Analysis Software Package," Air Force Weapons Laboratory, Kirtland Air Force Base, New Mexico, 1987.
79. N.G. Basov, I.G. Zubarev, A.V. Kotov, S.I. Mikhailov, and M.G. Smirnov, Sov. J. Quantum Electron. 2, 237 (1979).
80. R.L. Abrams, C.R. Giuliano, and J.F. Lam, Optics Lett. 6, 131 (1981).
81. M. Born and E. Wolf, Principles of Optics, 4th ed., Pergamon Press, Oxford, 1970.
82. M.A. Ortega, private communication, October, 1987.
83. K.R. Calahan, "High Fresnel Number Resonator Experiments," MS Thesis, University of New Mexico, 1985.
84. L.P. Schelonka, K.R. Calahan, and C.M. Clayton, submitted to Applied Optics.
85. P.R. Peterson, private communication, May, 1987.
86. J.W. Goodman, Introduction to Fourier Optics, McGraw-Hill, New York, 1968.

87. M. Sargent, M.O. Scully, W.E. Lamb, Laser Physics, Addison-Wesley, Reading, Massachusetts, 1974.
88. J.T. Verdeyen, Laser Electronics, Prentice-Hall, Englewood Cliffs, New Jersey, 1981.
89. A. Yariv, Optical Electronics, 2d ed. Holt, Rinehart and Winston, New York, 1976.
90. E. Hecht and A. Zajac, Optics, Addison-Wesley, Reading, Massachusetts, 1974.
91. A. Yariv, Quantum Electronics, John Wiley and Sons, New York, 1967.
92. A. Corvo, "Multiple Short Pulse and Single Long Pulse/Forward Stimulated Brillouin Scattering," PhD Dissertation, University of New Mexico, 1987.
93. M.A. Greiner-Mothes and K.J. Witte, Appl. Phys. Lett. 49, 4 (1986).
94. V.I. Bespalov, A.A. Betin, and G.A. Pasmanik, Sov. Tech. Phys Lett. 3, 85 (1977).

95. M. Valley, R. Moyer, M. Cimolino, M. Sones, paper THK43, in CLEO '86 Technical Digest, Optical Society of America, Washington, DC, 1986.
96. R. Moyer, M. Valley, M. Cimolino, M. Sones, paper THD4, in CLEO '86 Technical Digest, Optical Society of America, Washington, DC, 1986.
97. L.P. Schelonka, to be published in Proc. SPIE 912, (1988).
98. L.P. Schelonka, Optics Commun. 64, 293 (1987).
99. L.P. Schelonka and C.M. Clayton, Optics Lett. 13, 42 (1988).
100. C.L. Tang, J. Appl. Phys. 37, 2945 (1966).
101. R.H. Enns and I.P. Batra, Phys. Lett. 28A, 591 (1969).
102. W. Demtroder, Laser Spectroscopy, Springer-Verlag, Berlin, 1982.
103. J.A. Armstrong, N. Bloembergen, J. Ducuing, and P.S. Pershan, Phys. Rev. 127, 1918 (1962).
104. R.W. Weast, ed., CRC Handbook of Chemistry and Physics, 64th ed., CRC Press, Boca Raton, Florida, 1983.

105. D. Pohl, M. Maier, and W. Kaiser, Phys. Rev. Lett. 20, 366 (1968).
106. M.S. Zubairy and J.K. McIver, Phys. Rev. A 31, 856 (1985).
107. A. Gavrielides and P. Peterson, J. Opt. Soc. Am. B 3, 1394 (1986).
108. B.N. Perry, P. Rabinowitz, and M. Newstein, Phys. Rev. A 27, 1989 (1983).
109. C.R. Wylie, Advanced Engineering Mathematics, McGraw-Hill, New York, 1975.
110. J. Mathews, R.L. Walker, Mathematical Methods of Physics, 2d ed., W.A. Benjamin, Menlo Park, California, 1970.
111. J.C. Vetter, private communication, April, 1987.
112. D.A. Cardimona and M.A. Ortega, private communication, September, 1987.
113. M. Abramowitz and I.E. Stegun, eds., Handbook of Mathematical Functions, National Bureau of Standards, Washington, DC, 1972.